

Quantitative Photoacoustic Imaging

by

Peng Shao

A thesis submitted in partial fulfillment of the requirements for the degree of

Doctor of Philosophy

in

Biomedical Engineering

Department of Electrical and Computer Engineering
University of Alberta

© Peng Shao, 2014

Abstract

Tumor angiogenesis is the cancer-induced chaotic proliferation of blood vessel structure penetrating into surrounding cancerous tissue. Effective microvasculature imaging method is urgently desired for both fundamental biological and clinical studies. However, this is a challenging task, as existing standard imaging techniques are limited by factors such as poor resolution, high cost, necessity of using imaging contrast agent and invasiveness. Photoacoustic (PA) imaging, as a non-ionizing modality, has drawn significant interest due to the promise it holds for high-resolution, noninvasiveness and its capability to reveal functional information based on intrinsic optical contrast.

The ultimate goal of this dissertation is to further previous work on quantitative photoacoustic imaging, specifically, to contribute to quantitative imaging of tumor angiogenesis and anti-angiogenetic therapy. The work presented in this dissertation can be divided into three parts. In the first part, we focus on quantitative photoacoustic tomography (qPAT) for deep tissue imaging. We developed a series of algorithms that are able to quantify deep tissue photoacoustic imaging. We demonstrated by simulations that spatial distributions of optical properties, namely optical absorption and scattering, as well as the Grüneisen parameter can be

faithfully reconstructed with our reconstruction algorithms. In the second part, we focused on developing new imaging platforms for quantitative photoacoustic microscopy (PAM) imaging for superficial imaging depths. We successfully included fluorescently-labeled molecular context in optical-resolution PAM (OR-PAM) imaging by our integrated micro-endoscopy system that is able to simultaneously accomplish fluorescence and OR-PAM imaging. With our fast, wide field-of-view OR-PAM imaging technique, we significantly reduced the data acquisition time of conventional OR-PAM systems to a clinically realistic level. In the third part, experimental work is presented for quantitative imaging of vasculature variations and oxygen depletions due to photodynamic therapy with an acoustic-resolution PAM (AR-PAM) system we developed.

Preface

Chapter 3 of this dissertations has been published as P. Shao, B. Cox and R. J. Zemp, Estimating Optical Absorption, Scattering, and Grueneisen Distributions with Multiple-Illumination Photoacoustic Tomography, *Appl. Opt.*, 50(19), 3145-3154, 2011. I was responsible for algorithm development, simulation design, programming (data collection) as well as manuscript composition. B. Cox assisted with some of the data collection and contributed to manuscript edits. R. J. Zemp was the supervisory author and was involved with concept formation and manuscript composition.

Chapter 4 of this dissertation has been published as P. Shao T. J. Harrison and R. J. Zemp, Iterative algorithm for multiple-illumination photoacoustic tomography (MIPAT) using ultrasound channel data, *Biomed. Opt. Express*, 3(12), 3240-3249, 2012. I was responsible for the algorithm development, simulation design, programming (data collection) as well as manuscript composition. T. J. Harrison contributed to simulation design and manuscript edits. R. J. Zemp was the supervisory author and was involved with concept formation and manuscript composition.

Chapter 6 of this dissertation has been published as P. Shao, W. Shi, P. Hajireza and R. J. Zemp, Integrated micro-endoscopy system for simultaneous fluorescence

and optical-resolution photoacoustic imaging, *J. Biomed. Opt.*, 17(7), 076024, 2012.

I was the lead of the project, responsible for experiment design, data collection and manuscript composition. W. Shi contributed to experiments. P. Hajireza contributed to experiment design. R. J. Zemp was the supervisory author and was involved with concept formation and manuscript composition.

Chapter 7 of this dissertation has been published as P. Shao, W. Shi, R. K. Chee, and R. J. Zemp, Mosaic Acquisition and Processing for Optical-Resolution Photoacoustic Microscopy, *J. Biomed. Opt.*, 17(8), 070503, 2012. I was the lead of the project, responsible for experiment design, data collection and manuscript composition. W. Shi contributed to experiments. R. K. W. Chee contributed to software design and realization. R. J. Zemp was the supervisory author and was involved with concept formation and manuscript composition.

Chapter 8 of this dissertation forms part of collaboration led by Dr. Ronald B. Moore, with Dr. Roger J. Zemp. Dr. Moore assisted with concept formation and experiment design. I conducted the study and manuscript composition. Dr. Roger J. Zemp was the supervisory author and was involved with experiment design, concept formation and manuscript composition.

In vivo experiments procedures involving animals described in Chapter 6, 7 and 8 in this dissertation followed follow the laboratory animal protocol approved by the University of Alberta Animal Use and Care Committee.

Acknowledgements

First and foremost, I would like to express my sincere gratitude to my supervisor, Dr. Roger J. Zemp for his encouragement, patience, guidance and support during my doctoral program. I have been grateful that he took me as a graduate student and offered me the chance to work on exciting research projects, by which I built up my confidence to pursue a research career.

My sincere thanks to my supervisory committee members, Dr. Robert Fedosejevs and Dr. Mrinal Mandal, our collaborator Dr. Ronald Moore from Faculty of Medicine, and Dr. Mauricio Sacchi from the Physics Department. I have been lucky to have the chance to learn from, and work with these excellent professors during my stay at the University of Alberta. Their scholarship and professionalism impressed me and set up role models for me to follow in my future career.

Many thanks to the colleagues in my lab and my friends at the University of Alberta, for your support and companionship!

Contents

1. Introduction	1
1.1 The need for micro-vasculature imaging	1
1.2 Photoacoustic imaging	1
1.3 Problem statement and motivation	2
1.4 Major contribution of this dissertation	4
1.5 Organization of this dissertation	9
2. Background	8
2.1 Tumor angiogenesis and anti-angiogenetic therapy	17
2.2 Photodynamic therapy	18
2.3 Micro-vasculature imaging	19
2.4 Photoacoustic imaging	20
2.5 Challenges of photoacoustic techniques	29
3. Estimating Optical Absorption, Scattering, and Grüneisen Distributions with Multiple-illumination Photoacoustic Tomography (MI-PAT)	47
3.1 Introduction	47
3.2 Theory	52
3.2.1 Problem of absorption-scattering non-uniqueness	53
3.2.2 Multiple-illumination locations as a potential remedy for absorption-scattering non-uniqueness	55
3.2.3 Multiple-optical-source photoacoustic reconstruction methodology for absorption and scattering perturbations in a known turbid background	55

3.2.4	Recovery of the spatially varying Grüneisenp parameter	61
3.3	Computational reconstruction	61
3.4	Discussion	66
3.5	Conclusions	70
3.6	Appendix A: Models of light transport	70
4.	Iterative Algorithm for Multiple-illumination Photoacoustic Tomography (MI-PAT) Using Ultrasound Channel Data	78
4.1	Introduction	78
4.2	Theory	80
4.2.1	Light propagation model	80
4.2.2	Reconstruction of the optical properties with ultrasound channel data	81
4.2.3	Inversion	85
4.3	Numerical simulation	86
4.4	Conclusion and discussion	91
5.	Consecutively Reconstructing Absorption and Scattering Distributions in Known Turbid Media with Multiple-Illumination Photoacoustic Microscopy (MI-PAT)	96
5.1	Introduction	96
5.2	Method	98
5.2.1	Light propagation model	98
5.2.2	Reconstruction of absorption distribution	98
5.3	Reconstruction of the diffusion coefficient perturbation distribution	102
5.4	Simulation	102
5.5	Conclusion and discussion	107
6.	Integrated Micro-endoscopy System for Simultaneous Fluorescence	

and Optical-Resolution Photoacoustic (OR-PAM) Imaging	114
6.1 Introduction	114
6.2 Method	115
6.3 Results	117
6.3.1 System characterization	117
6.3.2 In vivo imaging	119
6.4 Conclusion and discussion	120
7. Mosaic Acquisition and Processing for Optical-Resolution Photoacoustic Microscopy (OR-PAM)	125
7.1 Introduction	125
7.2 Method	127
7.3 Results	130
7.4 Conclusion and discussion	132
8. Monitoring Photodynamic therapy with Photoacoustic microscopy (PAM)	136
8.1 Introduction	136
8.2 Method	138
8.3 Results	140
8.4 Conclusion and discussion	144
9. Conclusions and Future Prospects	149
9.1 Summary of work done in this dissertation	149
9.2 Directions of future work	150

List of Tables

3.1 Condition Number for Different Configurations. 66

4.1 Condition Number for Different Configurations 91

List of Figures

2.1. A typical PAT imaging system.	22
2.2. Schematic of the reflection-mode dark-field illumination acoustic-resolution photoacoustic tomography (AR-PAM).	24
2.3. Schematic of the first optical-resolution photoacoustic microscopy (OR-PAM) system.	26
3.1. The absorption-scattering non-uniqueness problem in quantitative photoacoustic tomography.	54
3.2. Light propagation geometry.	57
3.3. Simulation models and results.	64
3.4. Simulation configuration.	65
3.5. Singular value spectra (normalized by the largest value) of the matrix Q used in the example of Fig. 3.3 for recovering both absorption and scattering perturbations.	65
4.1. The simulation model setup.	86
4.2. Some quantities generated in the simulation study.	88
4.3. Simulation results the proposed method and the ratio metric method with 4 illuminations surrounding the object.	89
4.4. Normalized reconstruction errors with 10 iterations.	90
4.5. Singular value spectra of the Jacobian matrices for different configurations.	91
5.1. Flow chart of the iterative algorithm.	102
5.2. Reconstruction of optical property distributions with the proposed method.	103
5.3. Reconstruction of sharp (a) and smoothed features (b) with the proposed method with 20 iterations.	104
5.4. Reconstruction with non-overlapping features to demonstrate capabilities of the algorithm to alleviate cross-talk between absorption and diffusion coefficient.	105
5.5. Reconstruction of a synthetic blood vessel vasculature.	105
5.6. Cross-sectional profiles of the reconstruction results along horizontal direction in the center of the true model in Figure 5.5.	106
5.7. Reconstruction errors with different number of optical sources.	107
5.8. Normalized reconstruction errors with 50 iterations.	107
6.1. Experimental setup for the combined photoacoustic and fluorescence micro-endoscopy imaging system.	117

6.2. System characterization.	118
6.3. Results of in vivo experiments.	120
7.1. System configuration.	128
7.2. Flow chart of the control software.	129
7.3. Phantom studies.	131
7.4. Micro-vasculature of a living mouse ear.	132
8.1. Experiment setup.	139
8.2. Setup PAM image of a HT1080 tumor-induced neo-vasculature on a CAM model.	139
8.3. PDT-induced vasculature change in a CAM model.	140
8.4. PDT-induced vasculature change in a CAM model.	141
8.5. Change of a target blood vessel size in a CAM model due to PDT. ·	142
8.6. PDT-induced vasculature change in the treated area in a rat ear.	143
8.7. Change of a target blood vessel size in a rat ear model due to PDT. ·	143
8.8. Oxygen saturation change during PDT.	134

1. Introduction

1.1 The need for micro-vasculature imaging

Tumor angiogenesis refers to the proliferation of a blood vessel network that penetrates into cancerous growth [1]. From the 1970s, the importance of these vessels in tumors have been gradually identified as a hallmark of cancers [2]. To longitudinally and non-invasively monitor the angiogenic process is non-trivial, but could be very important to monitor tumor aggressiveness, track treatment efficacy, guide therapeutic decisions and to predict responders and non-responders. A number of techniques in biomedicine have been developed to visualize vasculature. For example, magnetic resonance angiography (MRA) based on magnetic resonance imaging (MRI) [3], X-ray computed tomography angiography (CT-Angiography, or CRA) [4], positron emission tomography (PET) [5] and contrast-enhanced ultrasound have been used. However, these methods are comparably expensive and requires utility of contrast agents. Limited by ultrasonic resolution, color and power Doppler techniques are only suitable for imaging large vessels [6]. Recently proposed optical techniques, such as laser Doppler imaging [7] [8] and laser speckle imaging [9] suffer from either limited penetration depth due to highly scattered photons in soft tissue, limited resolution or difficulty to target at specific regions of interests in practice. Moreover, they cannot visualize capillary-level changes, which is important for the angiogenic process.

1.2 Photoacoustic imaging

Photoacoustic (PA, or optoacoustic, thermoacoustic) imaging is an ideal candidate

for tumor angiogenesis imaging, due to its non-invasiveness, non-ionizing nature and its capability to provide intrinsic optical contrast, which can be used to reveal important functional information in biological bodies [10][11]. PA imaging is a hybrid biomedical imaging modality based on the photoacoustic effect [12]. As a non-ionizing imaging technique, it has drawn dramatic attention in the last two decades [13][14][15].

PA imaging relies on sensing acoustic energy from local transient thermal elastic expansion of absorbers due to ultra-short laser pulse irradiations. Therefore optical absorption provides the primary contrast for PA imaging. In biological subjects, while exogenous contrast agent are observable, hemoglobin in blood is the dominant absorber, PA imaging is thus ideal for visualizing vasculature without the use of exogenous agents. PA imaging falls into two categories: computational PA tomography (PAT), and scanning PA tomography, or PA microscopy (PAM). In PAT, an unfocused ultrasound transducer is used to detect the PA effect-induced acoustic waves, which are used to reconstruct tomographic images using an inverse algorithm [16]. In PAM [17], a pulsed laser beam is focused by an optical lens onto the target, and an ultrasound detector is employed to sense the acoustic waves, leading to 1D A-scan lines at each detection location, 2D B-scans and 3D C-scan images are then formed from a set of A-scans.

1.3 Problem statement and motivation

Despite the success of PA imaging in a wide spectrum of topics, it is also facing a number of challenges.

First, quantification of PA imaging is challenging. To visualize the optical properties based on PA images is important and very much desired [18]. For example, optical absorption can provide functional contrast, which reveals

angiogenesis and hypermetablism information; scattering spectra is related to physical properties of optical scatters such as cell nuclei size distribution. PA imaging quantification is nontrivial, because 1) it is in nature an ill-posed, nonlinear inverse problem [19]; 2) an unknown and spatially varying parameter, the Grüneisen parameter, which is impossible to de-couple from the measurements makes the problem even more complex. It has been proved that with PAT images by single wavelength and single optical source, it is impossible to simultaneously recover both absorption and scattering maps [20]. This is known as the absorption-scattering non-uniqueness problem. Previous literature focused on estimating only absorption coefficient distribution from reconstructed PAT images [21] [22] [23]. Some investigators also tried estimating both absorption and scattering with measurements by multiple wavelengths [24][25] with *a priori* information about wavelength-dependence of optical scattering. Reconstruction of the Grüneisen parameter is also desired. As it varies among different soft tissue types, and is temperature-dependent, there is a potential for applications, for example, spatial temperature monitoring in various treatments [26]. However, no reports of reconstructing the spatial distribution of the Grüneisen parameter were yet found before the work presented in this thesis.

Second, except for other highly absorbing molecules such as melanin, hemoglobin dominates optical absorption, therefore only blood vessel structure is visualized in normal soft tissue. Inclusion of cellular information in PA imaging has the potential to make it a more powerful tool in biomedical imaging. For example, though angiogenesis is a hallmark of tumor growth, morphological variations of cellular structures plays the most important role in clinical diagnosis in early stage cancer.

Third, slow imaging speed of conventional PA imaging systems hinders

application of this technique. PA imaging is essentially a fast imaging modality. For an ideal imaging system, the only time restriction is the time of flight from the imaging object to the ultrasonic sensing device. However, to form a 3D C-scan image, raster scanning is a necessity. The utility of mechanical raster scanning significantly slows down the data acquisition speed [27]. Whereas some workers used optical scanning instead, field-of-view and signal-to-noise ratio of the imaging system are sacrificed [28][29].

The long-term goal of this dissertation is to further previous work on quantitative photoacoustic imaging, targeting these three challenges. Specifically, to contribute to the development of efficient tools for quantitative imaging of tumor angiogenesis and anti-angiogenetic therapy.

1.4 Major contribution of this dissertation

Work described in this dissertation can be classified into the following three parts.

1. Quantitative photoacoustic tomography (qPAT)

We pioneered the use of multiple illuminations in photoacoustic tomography and explored the improved information content provided by such multiple-illumination schemes for quantitative imaging of optical properties. Previous to this work, most investigators working on photoacoustic tomography used blanket illumination or a single illumination pattern. However it was recognized that reconstruction of optical properties using photoacoustic data was challenging due to ill-posedness [26]. Yet in the Diffuse Optical Tomography field, multiple source-detector pairs were utilized to reconstruct coarse distributions of absorption and scattering parameters. Photoacoustic tomography used many multiple acoustic detectors previously but had not really considered multiple optical sources (with the exception of scanning photoacoustic microscopy

methods, however these scanning methods were not necessarily used for quantitative reconstructions of optical properties). We reasoned that photoacoustic tomography promised significantly higher spatial resolutions than DOT, moreover, adding multiple illuminations might pave a way to reconstruct optical properties with high photoacoustic resolution.

We developed a series of algorithms to quantitatively estimate optical properties using multiple-illumination imaging schemes, as well as the Grüneisen parameter distributions for photoacoustic tomography (PAT) imaging. Previous to this work, most photoacoustic literature focused on reconstruction of photoacoustic initial pressures [16][10][13] or estimation of optical absorption maps [21][22][30][31] but with the exception of a few contributions [25], little had been done to reconstruct optical scattering distributions (with or without multiple illuminations) and no previous work had considered reconstruction of the Grüneisen parameter distributions. Reconstruction of scattering distributions is important because, for example, cell nuclei are often enlarged in tumors and pre-cancers, leading to higher bulk-scattering coefficients. Being able to image scattering distributions could lead to improved ability to diagnose or detect cancers or monitor the effect of therapies. The Grüneisen parameter is the constant of proportionality between absorbed energy density and photoacoustic initial pressure generation and had previously been taken as spatially constant, however it is known to increase as much as $\sim 5\%$ per degree Celcius temperature rise and reconstruction of this parameter could be important for temperature mapping [32]. Additionally since this paper was published others have measured the Grüneisen parameter and found it can vary from tissue to tissue [33].

- We proposed a method using multiple-optical-sources to reconstruct optical absorption, scattering and Grüneisen parameter distributions in turbid

biological tissue simultaneously. This work resulted in publication [34]. Previous to this paper it was known that a given photoacoustic image could be associated with multiple absorption-scattering distributions hence quantitation of optical properties was challenging. In [34] we demonstrated that multiple optical illumination patterns could break this non-uniqueness and provided computational examples of demonstrating two pairs of absorption-scattering optical properties which gave the same simulated photoacoustic image with one illumination but not with a different illumination pattern. We provided a radiometric algorithm which showed for the first time the potential of multiple illuminations to enable reconstruction of absorption, scattering and Gruneisen parameter distributions.

- Previous quantitative reconstruction methods principally used ideally-reconstructed initial pressure distributions as a starting point. We proposed an iterative method to reconstruct optical properties directly using ultrasonic channel data (raw voltage signals as a function of time from each transducer element in a multi-detector array configuration). Unlike methods published before, this method does not rely on ideal reconstruction of PAT images, thus avoided degradation of reconstruction results due to imperfection, such as noise in PAT images. Also, instead of a two-step approach to first reconstruct initial pressures then reconstruct optical properties, our approach offers a one-step reconstruction inverting for both optical and acoustic data simultaneously. This algorithm again leverages multiple illuminations to provide an informative dataset for the reconstruction of optical absorption and scattering distributions but not Grüneisen distributions. This work was published as [35].
- Many of the previous approaches (including our previous works) required

inversion of large matrices which quickly scaled to unrealistically large matrices with a fine 3D mesh. To address this problem, I assisted my colleague Tyler Harrison in developing a fixed point iterative least-squares algorithm for reconstructing optical scattering distributions in a medium with a known scattering distribution [36]. A key advantage of this algorithm is that a key matrix inversion was performed analytically rather than computationally which is important for minimizing computational complexity and to minimize numerical errors associated with inverting ill-conditioned matrices. The algorithm was an extension of a previous method proposed by Cox et al. [21] for a single illumination scheme but shown to exhibit convergence problems with over-iteration including using experimental data as demonstrated by Jetzfellner et al. [31]. Our algorithm was a least-squares multiple-source extension to this previous work and we demonstrated that multiple-source data offered significant potential for ensuring convergence. This work was extended by including scattering as a parameter to reconstruct. We proposed a hybrid strategy which consecutively reconstructs optical absorption and scattering using multiple illuminations. While large matrices still needed to be inverted for scattering reconstructions, our low-complexity least-squares fixed point iteration approach was used for absorption reconstruction. By taking advantages of the robustness and fast convergence of absorption estimation, we demonstrated with simulations that the new method can faithfully reconstruct both absorption and scattering at a realistic signal-to-noise ratio level of ~ 30 dB and is the first algorithm and approach to show promise for experimental implementation.

We were not yet able to experimentally realize the concepts discussed here. However, the methods presented may prove important for quantitative

photoacoustic imaging in deep tissue (*cm*) on a macro-scale and will be the topic of ongoing work.

2. Development of new imaging platforms.

- We developed an imaging platform which for the first time included fluorescently-labeled cellular context in photoacoustic microscopy (PAM) imaging by combining a fluorescent imaging system and our micro-endoscopic PAM system. This approach avoids the necessity of a fluorescent label to be injected to visualize the microvasculature as it instead uses endogenous hemoglobin contrast for photoacoustic imaging. Fluorescent labelling of cells is accomplished by a simple topical applicator so the approach is non-invasive and has potential for clinical translation. This work was published in [37].
- We developed a fast, wide FOV imaging system using a fast fiber laser system, optical scanning and the mosaicing acquisition and processing. Our system is able to achieve arbitrary FOVs and reduced imaging acquisition time of conventional mechanical scanning PAM imaging systems by over 20 times. This work was published in [38].

The work is in nature experimental and focuses on developing imaging platforms for superficial ($< 3 \text{ mm}$) micro-scale structure visualization in biological objects with the optical-resolution PAM technique. This work used fiber lasers with repetition rates significantly higher than most previous approaches. The improved imaging speed and field of view may help make the technique easier to use for biologists and could help facilitate translation to the clinic.

3. An example of applications: monitoring photodynamic therapy with acoustic-resolution photoacoustic microscopy.

- We demonstrated the capability of our custom-developed acoustic-resolution

PAM system for monitoring vasculature changes and oxygen saturation variations induced by photodynamic therapy. This is the first report of using PAM technique to quantitatively study morphological and functional changes of blood vessel structures in small animal models before, during, and after photodynamic therapy treatments. The work shows promise for detecting vessel ablation and oxygen depletion in blood and tissues during and after photodynamic therapy and could lead to improved treatment guidance and could help predict responders from non-responders.

1.5 Organization of this dissertation

The rest of the dissertation is organized as follows: Chapter 2 provide background knowledge on tumor angiogenesis and photodynamic therapy, principle of PA imaging, as well as literature review on the development of PA imaging techniques. The work presented in this dissertation can be divided into three parts. The first part (chapters 3-5) is focused on quantitative photoacoustic tomography (qPAT). The second part (Chapters 6-7) is focused on developing new imaging platforms for quantitative photoacoustic microscopy (PAM). In the third part (Chapter 8), experimental work is described for quantitative imaging of vasculature variations due to photodynamic therapy with PAM. Chapter 9 summarizes contributions, discusses conclusions and future work.

Contents of this dissertation (Chapter 3 to Chapter 8) are drawn from the following publications with permissions:

- [1] **P. Shao**, B. Cox and R. J. Zemp, Estimating Optical Absorption, Scattering, and Grueneisen Distributions with Multiple-Illumination Photoacoustic Tomography, *Appl. Opt.*, 50(19), 3145-3154, 2011.
- [2] **P. Shao** and R. J. Zemp, Iterative Algorithm for Multiple-Illumination

Photoacoustic Tomography (MIPAT) Using Ultrasound Channel Data, *Biomed. Opt. Express*, 3(12), 3240-3249, 2012.

- [3] **P. Shao**, T. Harrison, and R. J. Zemp, A Consecutive Strategy for Estimating Absorption and Scattering Coefficient Distributions in Multiple-Illumination Photoacoustic Tomography (MI-PAT), submitted to *J. Biomed. Opt.*, under review, 2014.
- [4] **P. Shao**, W. Shi, P. Haji Reza and R. J. Zemp, Integrated Micro-Endoscopy System for Simultaneous Fluorescence and Optical-Resolution Photoacoustic Imaging, *J. Biomed. Opt.*, 17(7), 076024, 2012.
- [5] **P. Shao**, W. Shi, R. K. Chee, and R. J. Zemp, Mosaic Acquisition and Processing for Optical-Resolution Photoacoustic Microscopy, *J. Biomed. Opt.*, 17(8), 070503, 2012.
- [6] **P. Shao**, Roger J. Zemp, Monitoring Photodynamic Therapy Using Photoacoustic Microscopy, *in preparation*, 2014.

Bibliography

- [1] B. R. Zetter, “Angiogenesis and tumor metastasis.,” *Annu. Rev. Med.*, vol. 49, no. 1, pp. 407–24, Jan. 1998.
- [2] R. S. Kerbel, “Tumor angiogenesis: past, present and the near future.,” *Carcinogenesis*, vol. 21, no. 3, pp. 505–15, Mar. 2000.
- [3] M. P. Hartung, T. M. Grist, and C. J. François, “Magnetic resonance angiography: current status and future directions,” *J. Cardiovasc. Magn. Reson.*, vol. 13, no. 1, p. 19, 2011.
- [4] A. Kopp, “Non-invasive coronary angiography with high resolution multidetector-row computed tomography. Results in 102 patients,” *Eur. Heart J.*, vol. 23, no. 21, pp. 1714–1725, Nov. 2002.
- [5] S. Valable, E. Petit, S. Roussel, L. Marteau, J. Toutain, D. Divoux, F. Sobrio, J. Delamare, L. Barré, and M. Bernaudin, “Complementary information from magnetic resonance imaging and (18)F-fluoromisonidazole positron emission tomography in the assessment of the response to an antiangiogenic treatment in a rat brain tumor model.,” *Nucl. Med. Biol.*, vol. 38, no. 6, pp. 781–93, Aug. 2011.
- [6] R. S. C. Cobbold, *Foundations of Biomedical Ultrasound*. Oxford University Press, 2006.
- [7] A. Major, S. Kimel, S. Mee, T. E. Milner, D. J. Smithies, S. M. Srinivas, and J. S. Nelson, “Microvascular photodynamic effects determined in vivo

- using optical Doppler tomography,” *IEEE J. Sel. Top. Quantum Electron.*, vol. 5, no. 4, pp. 1168–1175, 1999.
- [8] J. Tyrrell, C. Thorn, a Shore, S. Campbell, and a Curnow, “Oxygen saturation and perfusion changes during dermatological methylaminolaevulinate photodynamic therapy.,” *Br. J. Dermatol.*, vol. 165, no. 6, pp. 1323–31, Dec. 2011.
- [9] H. Qiu, Y. Zhou, Y. Gu, Q. Ang, S. Zhao, Y. Wang, J. Zeng, and N. Huang, “Monitoring Microcirculation Changes in Port Wine Stains During Vascular Targeted Photodynamic Therapy by Laser Speckle Imaging,” *Photochem. Photobiol.*, vol. 88, no. 4, pp. 978–984, Jul. 2012.
- [10] G. Ku, X. Wang, X. Xie, G. Stoica, and L. V Wang, “Imaging of tumor angiogenesis in rat brains in vivo by photoacoustic tomography.,” *Appl. Opt.*, vol. 44, no. 5, pp. 770–5, Feb. 2005.
- [11] S. Hu, S. Oladipupo, J. Yao, A. C. Santeford, K. Maslov, J. Kovalski, J. M. Arbeit, and L. V. Wang, “Optical-resolution photoacoustic microscopy of angiogenesis in a transgenic mouse model,” in *proceedings of SPIE*, 2010, vol. 7564, pp. 756406–756406–5.
- [12] M. Xu and L. V. Wang, “Photoacoustic imaging in biomedicine,” *Rev. Sci. Instrum.*, vol. 77, no. 4, p. 041101, 2006.
- [13] X. Wang, Y. Pang, G. Ku, X. Xie, G. Stoica, and L. V Wang, “Noninvasive laser-induced photoacoustic tomography for structural and functional in vivo imaging of the brain.,” *Nat. Biotechnol.*, vol. 21, no. 7, pp. 803–6, Jul. 2003.

- [14] H. F. Zhang, K. Maslov, G. Stoica, and L. V Wang, "Functional photoacoustic microscopy for high-resolution and noninvasive in vivo imaging.," *Nat. Biotechnol.*, vol. 24, no. 7, pp. 848–51, Jul. 2006.
- [15] J. Yao and L. V Wang, "Photoacoustic Microscopy.," *Laser Photon. Rev.*, vol. 7, no. 5, pp. 1771–1773, Sep. 2013.
- [16] X. Wang, Y. Xu, M. Xu, S. Yokoo, E. S. Fry, and L. V. Wang, "Photoacoustic tomography of biological tissues with high cross-section resolution: Reconstruction and experiment," *Med. Phys.*, vol. 29, no. 12, p. 2799, 2002.
- [17] H. F. Zhang, K. Maslov, M.-L. Li, G. Stoica, and L. V Wang, "In vivo volumetric imaging of subcutaneous microvasculature by photoacoustic microscopy.," *Opt. Express*, vol. 14, no. 20, pp. 9317–23, Oct. 2006.
- [18] L. V. Wang and H. Wu, *Biomedical Optics, principles and imaging*. Willey-Interscience, 2007.
- [19] B. Cox, J. G. Laufer, S. R. Arridge, and P. C. Beard, "Quantitative spectroscopic photoacoustic imaging: a review.," *J. Biomed. Opt.*, vol. 17, no. 6, p. 061202, Jun. 2012.
- [20] G. Bal and K. Ren, "Multi-source quantitative photoacoustic tomography in a diffusive regime," *Inverse Probl.*, vol. 27, no. 7, p. 075003, Jul. 2011.
- [21] B. T. Cox, S. R. Arridge, K. P. Köstli, and P. C. Beard, "two-dimensional quantitative photoacoustic image reconstruction of absorption distribution in scattering media by use of a simple iterative method," pp. 4–6, 2006.

- [22] Z. Yuan and H. Jiang, “Quantitative photoacoustic tomography.,” *Philos. Trans. A. Math. Phys. Eng. Sci.*, vol. 367, no. 1900, pp. 3043–54, Aug. 2009.
- [23] R. J. Zemp, “Quantitative photoacoustic tomography with multiple optical sources.,” *Appl. Opt.*, vol. 49, no. 18, pp. 3566–72, Jun. 2010.
- [24] G. Bal and K. Ren, “On multi-spectral quantitative photoacoustic tomography in diffusive regime,” *Inverse Probl.*, vol. 28, no. 2, p. 025010, Feb. 2012.
- [25] B. T. Cox, S. R. Arridge, and P. C. Beard, “Estimating chromophore distributions from multiwavelength photoacoustic images.,” *J. Opt. Soc. Am. A. Opt. Image Sci. Vis.*, vol. 26, no. 2, pp. 443–55, Feb. 2009.
- [26] B. T. Cox, J. G. Laufer, and P. C. Beard, “<title>The challenges for quantitative photoacoustic imaging</title>,” vol. 7177, pp. 717713–717713–9, Feb. 2009.
- [27] S. Hu, K. Maslov, and L. V. Wang, “Second-generation optical-resolution photoacoustic microscopy with improved sensitivity and speed,” *Opt. Lett.*, vol. 36, no. 7, pp. 1134–1136, 2011.
- [28] Z. Xie, S. Jiao, H. F. Zhang, and C. A. Puliafito, “Laser-scanning optical-resolution photoacoustic microscopy,” *Opt. Lett.*, vol. 34, no. 12, pp. 1771–1773, 2009.
- [29] W. Shi, P. Hajireza, P. Shao, A. Forbrich, and R. J. Zemp, “In vivo near-realtime volumetric optical-resolution photoacoustic microscopy using

- a high-repetition-rate nanosecond fiber-laser.,” *Opt. Express*, vol. 19, no. 18, pp. 17143–50, Aug. 2011.
- [30] Z. Guo, S. Hu, and L. V Wang, “Calibration-free absolute quantification of optical absorption coefficients using acoustic spectra in 3D photoacoustic microscopy of biological tissue.,” *Opt. Lett.*, vol. 35, no. 12, pp. 2067–9, Jun. 2010.
- [31] T. Jetzfellner, D. Razansky, A. Rosenthal, R. Schulz, K.-H. Englmeier, and V. Ntziachristos, “Performance of iterative optoacoustic tomography with experimental data,” *Appl. Phys. Lett.*, vol. 95, no. 1, p. 013703, 2009.
- [32] M. Pramanik and L. V Wang, “Thermoacoustic and photoacoustic sensing of temperature.,” *J. Biomed. Opt.*, vol. 14, no. 5, p. 054024, 2009.
- [33] D.-K. Yao and L. V. Wang, “Measurement of Grüneisen parameter of tissue by photoacoustic spectrometry,” vol. 8581, p. 858138, Mar. 2013.
- [34] P. Shao, B. Cox, and R. J. Zemp, “Estimating optical absorption, scattering, and Grueneisen distributions with multiple-illumination photoacoustic tomography.,” *Appl. Opt.*, vol. 50, no. 19, pp. 3145–54, Jul. 2011.
- [35] P. Shao, T. Harrison, and R. J. Zemp, “Iterative algorithm for multiple illumination photoacoustic tomography (MIPAT) using ultrasound channel data.,” *Biomed. Opt. Express*, vol. 3, no. 12, pp. 3240–9, Dec. 2012.
- [36] T. Harrison, P. Shao, and R. J. Zemp, “A least-squares fixed-point iterative algorithm for multiple illumination photoacoustic tomography.,” *Biomed. Opt. Express*, vol. 4, no. 10, pp. 2224–30, Jan. 2013.

- [37] P. Shao, W. Shi, P. Hajireza, and R. J. Zemp, "Integrated micro-endoscopy system for simultaneous fluorescence and optical-resolution photoacoustic imaging.," *J. Biomed. Opt.*, vol. 17, no. 7, p. 076024, Jul. 2012.
- [38] P. Shao, W. Shi, R. K. W. Chee, and R. J. Zemp, "Mosaic acquisition and processing for optical-resolution photoacoustic microscopy.," *J. Biomed. Opt.*, vol. 17, no. 8, pp. 080503–1, Aug. 2012.

2. Background

2.1. Tumor angiogenesis and anti-angiogenic therapy

Angiogenesis is the process of blood vessel formation from existing vasculature. Tumor angiogenesis refers to the tumor-induced chaotic proliferation of blood vessel structures penetrating into cancerous tissue [1]. The blood vessel network supplies nutrients and oxygen and remove waste products from tumors [2]. Though permeable blood vessels surround tumors have been observed for a long history, its importance in diagnosis and treatment of cancer was not recognized until the 1970s. It is well-appreciated nowadays that angiogenesis is a critical component of tumor metastasis [3]. A highly vascular tumor might lead to high potential to produce metastases. For example, studies implied a direct correlation between vascular density and the likelihood of metastasis in human breast cancer patients [4].

Angiogenesis is initiated by certain stimuli, mainly exposure of cancer tissue to hypoxia [5]. After a complex response by cancer cells, transcription of certain growth factors is started within the nucleus. These factors include the well-known VEGF (vessel endothelial growth factor), VEGFR-C, endothelin-1, platelet-derived growth factor and so on. These growth factors stimulate the growth of endothelial cells, which lead to formation of new blood vessels. The revolutionary concept antiangiogenesis was proposed by Folkman J. in 1971. As a pioneer on tumor angiogenesis, he proposed to treat cancer by ‘preventing new vessel sprouts from penetrating into early tumor implant.’ [5]. Efforts were directed to search for agents targeting VEGF, or multiple growth factors [6]. Three classes of agents targeting at VEGF were developed, including monoclonal antibodies, VEGF decoy receptors

and small molecule tyrosine kinase inhibitors (TKIs).

Development of antiangiogenic therapy has been a long journey. The first antiangiogenesis drug was approved by FDA in 2004, over 30 years after Folkman's imaginary hypothesis. However, only modest improvement in terms of survival benefits were observed, 'with possible exception of ... renal-cell carcinoma [6].' There are still many questions with unclear answers, for example, resistance to angiogenic therapy.

2.2. Photodynamic therapy

Photodynamic therapy (PDT) is a photochemistry-based method which uses light at certain wavelength illuminating light-activable chemical, namely a photosensitizer (PS), to generate reactive oxygen species (ROS) that is cytotoxic to diseased cells [7]. In modern clinical settings, PS administration is accomplished either intravenously or topically, followed by laser illumination. PDT is an oxygen-dependent procedure [8]: when irradiated by light, the PS transfers energy from photons to molecular oxygen to generate ROS, such as singlet oxygen ($^1\text{O}_2$) and free radicals. PDT is used clinically to treat a wide spectrum of medical conditions, for example, skin disease [9] and cancer [10]. It impacts a tumor by several mechanisms, among which vascular damage is one of the most important.

Evaluation of PDT efficacy is a challenging topic. Conventionally, researchers focus on measurement of the two fundamental elements of PDT: PS and light dose administration [11]. However, it is now recognized that simple measurements of these quantities are not sufficient. Real-time monitoring of multiple dosimetric parameters including biological response is urgently needed for personalized treatment planning and evaluation [11]. Vascular damage, in terms of blood flow, vessel diameter and blood perfusion variations, are some of the representative factors of biological response.

2.3. Micro-vasculature imaging

Effective imaging techniques are desirable for both fundamental research and clinical purposes in the aforementioned areas. Quite a number of approaches have been proposed to visualize vasculature. For example, Magnetic resonance angiography (MRA) – a group of techniques based on magnetic resonance imaging (MRI). However, the necessity of imaging contrast agent, comparatively high cost and limited spatial and temporal resolution hinders its applications [12]. There is always a trade-off between higher field strength and parameters such as scan time, spatial resolution and contrast agent dose. X-ray-based computed tomography angiography (CT-Angiography, or CRA) is becoming more popular and is able to provide better spatial resolution than MRI methods with access to almost any regions of interests in human bodies. But the significant amount of ionizing radiation and difficulty in contrast agent administration is a challenge [13]. In a study by Einstein A. J. et al. [14], the authors argued that there is a ‘nonnegligible’ correlation between use of a 64-slice CRA and lifetime of attributable risk of cancer. Positron emission tomography (PET) is a nuclear functional imaging technique to trace positron-emitting tracer in human bodies. 3D images are reconstructed with the assistance of CT or MRI to assess tracer concentration in the subjects. PET has been used for vasculature imaging since 1997 [15]. However, tremendous challenges still exist such as poor spatial resolution (millimeter), high-cost and exposure of patients to radiation by tracer [16]. Ultrasound imaging, as a fast, portable, cost-effective, non-ionizing and noninvasive technique, is commonly used for studying vasculature in clinical practices. Usually color or power Doppler images, which are produced with the Doppler Effect containing information such as blood vessel structure, relative velocity and directions of blood flow are co-registered with ultrasound sonography [17]. However, this technique can only

provide limited spatial resolution determined by ultrasound imaging system. Whereas intravascular ultrasound (IVUS) significantly improves imaging resolution (with a lateral resolution of 200 – 250 μm , axial resolution of $\sim 80 \mu m$) compared with clinical ultrasonography [18], the invasiveness by inserting miniature probing device into blood vessels is a concern [19]. Advanced optical techniques have been used for micro-vascular imaging. Optical Doppler tomography [20] is a technique that combines the laser Doppler flowmetry and optical coherence tomography. Whereas high spatial resolution is achieved with this technique, its penetration depth in turbid soft tissue is limited [21] [22]. Recently laser speckle contrast imaging [9] has been proposed to study vasculature change. However, as addressed by Duncan D. et al. [23], because the results by this technique are in arbitrary units, it can only serve as a semi-quantitative real-time mapping of blood flow fields and calibration is needed.

2.4. Photoacoustic imaging

Photoacoustic (PA) imaging is based on the PA effect, which refers to generation of acoustic energy based on absorption of electromagnetic (EM) energy [24]. PA effect was first discovered by the eminent scientist Alexander G. Bell while searching for means to transmit sound over long distance and reported in 1880 [25]. However, the effect was soon abandoned till the invention of intensive light sources and reliable acoustic sensors before being applied to different fields.

PA imaging in biomedicine was pioneered in late 1980's and soon developed very quick because of its multifold advantages. The main driver behind early efforts was to combine ultrasonic resolution and intrinsic optical contrast, although optical-resolution PA imaging techniques was proposed later in 2008 [26]. In pure optical imaging, scattering of photons in turbid biological tissue significantly degrades spatial resolution. Despite that ultrasound provides with greater penetration depth,

mechanical properties detected by pure ultrasonic imaging technique is weak [17]. Combining these two aspects takes advantages of the two energy forms. Since ultrasound is ~ 1000 times less scattered in soft tissue [17], initial pressure generated by PA, which carries optical contrast information is able to propagate over a longer distance. The non-ionizing mechanical waves in PA imaging are not biologically hazardous. Moreover, since the dominant absorber in soft tissue is oxy- and deoxyhemoglobin (others include water and melanin), demultiplexing of these two components can provide functional information, namely the oxygen concentration (SO_2) in biological tissue, which reveals physiological information of significant importance.

In PA imaging, upon absorption of laser pulses with short duration, local thermoelastic expansion-induced transient acoustic pressure acts as initial acoustic sources. The acoustic waves propagate through the tissue to the surface and are detected by ultrasound sensors positioned nearby. Recorded acoustic waves are stored for image reconstruction to estimate the internal structure of the biological target. According to the image reconstruction method involved in PA imaging, it can be classified into two categories: computational photoacoustic tomography (PAT) and scanning photoacoustic microscopy (PAM).

Computational Photoacoustic Tomography (PAT)

Computational photoacoustic tomography (usually termed as photoacoustic tomography, PAT) is based on image reconstruction with backprojection algorithms [27]. With this technique, usually a nanosecond-pulsed wide-field laser is used as the light source, above the target for sample surface heating. An ultrasound transducer is nearby to sense generated photoacoustic signals. To optimize lateral resolution, Wang et al. [27] proposed to scan the acoustic sensor in a plane perpendicular to the laser irradiation axis with a motorized stage, as is shown in

Figure 2.1. A modified back-projection method is used for image reconstruction. A resolution of $\sim 60 \mu\text{m}$ was achieved with a 10-MHz center-frequency transducer, which has a similar diffraction limit.

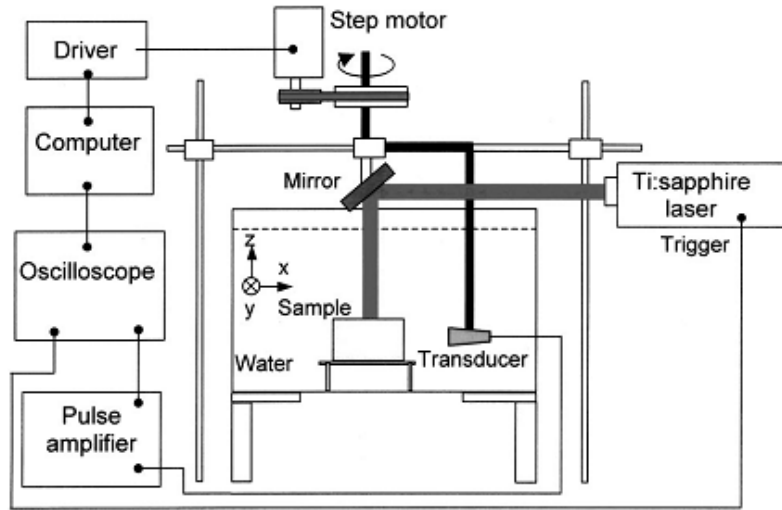


Figure 2.1 A typical PAT imaging system [27].

Alternative imaging system setups were proposed to reduce imaging time by avoiding or minimizing mechanical scanning. Conventional linear array transducers was utilized [28] [29]. Ephrat et al. [30] used a sparse 2D annular detector array. Gamelin J. [31] introduced a custom-fabricated 5-MHz 128-element curved ultrasonic transducer array that covers a 90-degree field of view (FOV). Mechanical rotation is required to cover a 360-degree full FOV. Gamelin [32] and Yao [33] then introduced a second generation curved ring with 512 detector elements. This ring provides with a 0.1-mm axial resolution and a 0.25-mm transverse resolution. Kruger et al. introduced a bowl-shape hemispherical transducer array [34]. Xiang et al. [35] reported a 4D PAT system with a spherical ultrasound transducer array, which included the time resolution to provide real-time 3D PAT imaging. The system achieved hundred-millisecond temporal resolution.

Reconstruction algorithms are crucial for PAT. Analytic reconstruction methods were employed for PAT. Xu M. and Wang L. V. [36] reported the first reconstruction method based on the backprojection algorithm for PAT in a spherical geometry. A number of other algorithms of the filtered backprojection form were introduced [27] [37]. Paltauf et al. [38] utilized an iterative method to alleviate artifacts when using backprojection methods, which later on became an important topic in this field [39] [30]. Yao and Jiang used a finite element-based framework combined with total variation minimization to improve reconstruction quality using time-domain data [40]. In practice, sparse spatial sampling is desired to increase imaging speed. Compressed sensing techniques was introduced to compensate for recovering unobserved components (incomplete datasets) under certain conditions [41] [42]. With phantom studies and *in vivo* experiments, the authors demonstrates that undersampling artefacts were effectively reduced.

PAT can be used to for imaging deeper tissues than PAM. In [34], the authors used their PAT system to image vasculature in human breasts with a 40-*mm* penetration depth at a resolution of 250 μm .

In this dissertation we discuss improving both PAT and PAM. For PAT, we primarily use simulations to demonstrate new algorithms for improved quantification.

Scanning photoacoustic microscopy (PAM)

Scanning photoacoustic microscopy is very much similar to the clinically used ultrasonography imaging in principle. An ultrasonic detector (transducer) scans along a soft tissue to collect multiple A-scan signals, which can be converted to single 1D image depicting structure information along the vertical axis. Multiple A-scans generated sequentially along one direction are then combined to form a B-scan cross-sectional view, or tomography. B-scan images are further stacked

together to generate 3D C-scan volumetric view. The maximum amplitude projection (MAP, or maximum intensity projection, MIP) method was employed to visualize the 3D dataset on the plane of projection (horizontal plane).

Scanning photoacoustic microscopy falls into two classes: the acoustic-resolution photoacoustic microscopy (AR-PAM) [43] and optical-resolution photoacoustic microscopy (OR-PAM) [44].

AR-PAM was first proposed by Maslov et al. [43] in 2005. In the first-reported setup, light coming out the light-deliver optical fiber is coaxially positioned with a focused ultrasound transducer with a 50-MHz center frequency (Fig. 2.2). NA (numerical aperture) of the transducer is as high as 0.44. Light pulse is first expanded and then focused by an optical condenser lens with a NA of 1.1. Foci of the light beam and the ultrasonic detector are aligned. The imaging system reached a lateral resolution of $45 \mu\text{m}$ and a 3-mm imaging depth. The author claimed multiple advantages of the dark-field illumination design, including reduced optical fluence on sample surface, mitigated shadows of superficial heterogeneities in images, and alleviated strong interference of the extraneous photoacoustic signals from superficial areas.

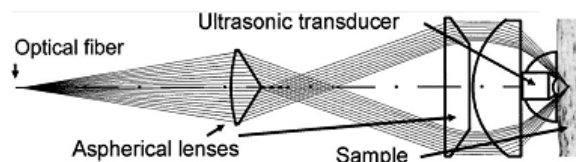


Figure 2.2 Schematic of the reflection-mode dark-field illumination acoustic-resolution photoacoustic tomography (AR-PAM) [43].

In AR-PAM imaging system, the axial resolution is determined by two factors [24]: the width of the ultrasound transducer impulse response, and the width of the irradiation laser pulses. AR-PAM system can provide a maximum penetration depth

to depth resolution ratio of over 100 [45]. Lateral resolution relies on the dimension of ultrasonic focal zone, which is in turn determined by the center-frequency and f-number of the transducer [17]. The detection sensitivity system decreases significantly outside the focal zone. As the imaging system works in the reflection mode rather than transmission mode, superficial layers of thick tissues can be imaged. With penetration depth on the order of millimeters, AR-PAM finds its applications in imaging vasculature [45], SO₂ in blood vessels [46], subcutaneous melanoma [47], and real-time cardiovascular dynamics [48] in nude mice. Alternative setups were proposed. Zemp et al. reported a system utilizing a high-frequency array transducer [49]. Zhang et al [50] from University College London reported their design utilizing a transparent Fabry-Perot sensor poisoned on the surface of the target to detect PA signal in the backward reflection fashion. Raster scanning was accomplished by moving the light source on a 2D motion stage. Since the spatial resolution is also determined by limitations of effect detection element size, it also falls into the category of AR-PAM. Success of this design was demonstrated in *in vivo* studies visualizing mouse brain vasculature [51] and tumor vasculature development [52].

OR-PAM imaging system was introduced in 2008 by Maslov et al. [26]. Rather than defining the lateral resolution with the focal zone of the ultrasound detector like AR-PAM, the system takes advantages of a strongly-focused bright field illumination (spot size $3.7 \mu m$, focal zone $200 \mu m$) to provide high resolution (experimentally demonstrated as $5 \mu m$). An imaging depth of $0.7 mm$ was achieved. Energy of a single laser pulse was $100 nJ$. Center-frequency of the ultrasound transducer was $75 MHz$ and a focal width of $27 \mu m$ was realized. Similar to PAM, the MAP method was used to visualize 3D volumetric data set. In the second generation OR-PAM by Hu et al. [53], the signal-to-noise ratio was

significantly increased by 18 dB with a novel acoustic coupling design. Penetration depth was deepened to 1.2 *mm*.

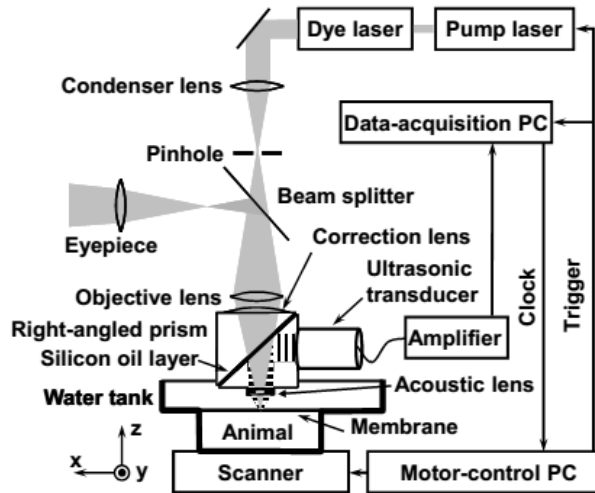


Figure 2.3 Schematic of the first optical-resolution photoacoustic microscopy (OR-PAM) system [26].

OR-PAM has been intensively studied ever since. Besides being applied to study structural information of vasculatures with high resolution [44], it has been utilized to study oxygen saturation in scenarios. Hu et al. [54] reported the first imaging of 3D volumetric structural and functional images of brain microvasculature through intact skull. Hu et al. also reported micro-hemodynamics [55][56] activities, such as vasomotion and vasodilation in small animals imaged with OR-PAM. These studies demonstrated the power of OR-PAM as a non-invasive, high-resolution imaging technique for potential broad applications in both biological and clinical studies. The healing process of lesions induced by laser burns [57] was imaged with OR-PAM. Amyloid plaques in the brain of a transgenic mouse model was imaged with OR-PAM [58]. Ophthalmic angiography using OR-PAM was introduced to image ocular microvasculature in living animals [59] as well as oxygen saturation in the iris microvasculature.

To speed up data acquisition, different scanning schemes were proposed. Rao et al. [60] reported a hybrid-scanning OR-PAM scheme. With this system, fast scanning in 1 dimension was accomplished with a galvanometer mirror and mechanical scanning was used for scanning in the other dimension. A cylindrically-focused transducer was used to receive acoustic signals. Xie et al. [61] reported a system using purely optical-scanning by a pair of galvanometer mirrors. Using a laser with a pulse repetition rate of 1024 Hz, it took only 2 *min* to generate an image with 256×256 pixels. Wang [62] used a fast voice-coil system to realize 1D fast scanning at the frequency of 40 Hz for B-scan. A motor stage was used for scanning along the other axis. Endoscopic imaging setup was proposed for OR-PAM [63]. Shi et al. [64] reported the first near-real time OR-PAM with optical-scanning and customized photoacoustic imaging probe [65]. By using a pulsed laser system with a laser pulse repetition rate of 600 kHz, a data acquisition rate of 4 frames per second was achieved. Field-of-view of the system, however, was limited to $1\text{mm} \times 1\text{mm}$.

Functional photoacoustic imaging

PA imaging is the only imaging modality that is able to provide morphological, functional and molecular imaging of ‘organelles, cells, tissues, and organs *in vivo*’ with high resolution at multiple scales [66]. Functional information here refers to physiological parameters including oxygenation and micro-hemodynamics.

Oxygenation in soft tissue is measured with oxygen saturation (SO_2). This is achieved by estimating concentrations of oxy- and deoxyhemoglobin: C_{ox} and C_{de} [67]. If we denote two laser wavelengths with λ_1 and λ_2 , the optical absorption coefficient can be written as:

$$\mu_a(\lambda_1) = \ln(10) \varepsilon_{ox}(\lambda_1)C_{ox} + \ln(10) \varepsilon_{de}(\lambda_1)C_{de} \quad (2.1)$$

$$\mu_a(\lambda_2) = \ln(10) \varepsilon_{ox}(\lambda_2)C_{ox} + \ln(10) \varepsilon_{de}(\lambda_2)C_{de} \quad (2.2)$$

where ε_{ox} and ε_{de} are the known molar extinction coefficients of oxy- and deoxyhemoglobin, respectively. Once C_{ox} and C_{de} are obtained, SO_2 is computed with

$$SO_2 = \frac{C_{ox}}{C_{ox} + C_{de}} \times 100\%. \quad (2.3)$$

This is also the principle of pulse oxymetry.

SO_2 is of significant importance in many applications. Examples include microcirculatory physiology, pathology, tumor angiogenesis, laser microsurgery, neuroscience etc. Zhang H. et al. [45] [68] pioneered estimating SO_2 with AR-PAM techniques. Hu S. et al. used OR-PAM to measure SO_2 in soft tissue [54].

Recently, Ashkenazi et al. [69][70] demonstrated the feasibility of performing photoacoustic lifetime imaging to estimate partial oxygen pressure (PO_2) in soft tissue. PO_2 refers to the pressure oxygen exerted in a mixture of other gases. By using a pump beam to excite chromophores out of their ground state, then using a time-delayed probe pulse to interrogate the remaining ground-state population as a function of pump-probe time delays, life-time curves according to different PO_2 level in biological objects is depicted.

Photoacoustic imaging of tumor angiogenesis and treatment monitoring

PA technique is an ideal candidate for vasculature imaging in biomedicine because its noninvasiveness, high resolution and capability to provide intrinsic optical contrast. Efforts have been directed to blood vessel vasculature imaging. Ku et al.

[71] described their work using a PAT system imaging angiogenesis induced by a brain tumor in rat model. The authors concluded that with a contrast that is good enough, the tumor can be diagnosed with the neovasculature observed. Xiang et al. [72] reported a serial PAT images of neovascularization in tumor angiogenesis in a rat with implanted gliosarcoma. Hu et al. [73] first implemented OR-PAM technique to chronic study of microchemodynamics. They reported longitudinal monitoring of hypoxia-inducible factor-1-mediated angiogenesis in a transgenic mouse model with their OR-PAM system.

Besides neovascularization, cancer treatment evaluation with PA technique was also proposed. Monitoring of photodynamic therapy (PDT) is one of the examples. Monitoring of dosimetric parameters such as light dose and photosensitizer administration [11] fail to evaluate efficacy of PDT. PA imaging has the potential for monitoring PDT by directly imaging biological response to the treatment. An early trial study was conducted by Xiang et al. [74], in which the authors demonstrated the capability of PAT technique to image tumor neovascularization and blood vessel destruction due to PDT.

2.5. Challenges of photoacoustic techniques

Despite the success of PA imaging in various applications, challenges exist in tumor angiogenesis imaging using PA techniques.

Quantification of photoacoustic imaging

To visualize the intrinsic optical properties, namely optical absorption and scattering in soft tissue is one of the most important purposes of PA imaging. This is called the quantification of PA imaging.

In this dissertation, we focus on quantitative photoacoustic tomography (qPAT) techniques. Usually, two steps are involved in qPAT: In the first step, one seeks to

recover photoacoustic initial pressure distribution. The second step focus on estimating the optical properties, namely absorption and scattering maps based on the first step. The first step is an ultrasonic inverse problem, whose framework has already been well-established, based on knowledge developed for other imaging modalities. The second step, which is an optical inverse problem, is rather challenging.

The contrast of PA imaging is mainly provided by optical absorption. Typical absorbers of interests in biological bodies include a) endogenous molecules, for example, hemoglobin (oxy- and deoxy-), melanin etc.; b) exogenous contrast agents, such as cell-surface receptor and biomolecules; c) optically absorbing enzymes or proteins [75]. The spatially varying optical property distributions can be used to reveal important physiological and pathological information, in both morphology and function. For example, quantitative estimates of concentrations of oxy- and deoxy-hemoglobin can be used to obtain oxygen saturation (SO_2), which is of significant importance of a wide spectrum of applications in biomedical studies and clinical practices. One example is hyper-metabolism in cancer [2]. Scattering coefficient distributions, which is due to micro-structure of soft tissue, may represent important morphological information interests researchers. For example, size distribution of cell nuclei can be used for cancer diagnosis, as enlarged nuclei are characteristic of many cancers [76]. However, quantitative reconstruction of optical property distributions from PA imaging is a rather challenging task, because in nature it is an ill-posed nonlinear problem. The initial pressure p generated in PA imaging is determined by local absorption μ_a , optical fluence Φ and the Grüneisen parameter Γ , which is a measure of conversion efficiency from heat to stress:

$$p = \Gamma \mu_a \Phi(\mu_a, \mu'_s). \quad (2.4)$$

However, the local optical fluence, is unknown in PA imaging. Moreover, since it is also a function of μ_a and local scattering property (quantified by the reduced scattering coefficient μ'_s , sometime with the diffusion coefficient D), to estimate $\{\mu_a, \mu'_s\}$ is a nonlinear problem. The spatially varying Grüneisen parameter Γ makes this problem even more complex. Quite a number of methods have been proposed for recovering optical absorption coefficient distribution in turbid biological media [77][78][79][80]. It has also been proved that without priori information such as wavelength dependence of optical scattering, it is impossible to correctly recover the optical properties [81]. Cox et al. [82] extended the work of previous literature by reconstructing both absorption and reduced scattering coefficients. However, with his method, multiple-wavelength, with the assistance of the priori information about wavelength of optical scattering have to been used. A common element lacked in the literature is the reconstruction of the Grüneisen parameter. Because it varies significantly among tissue types and is temperature-dependent [83], the spatial reconstruction of Grüneisen parameter can lead to important applications in clinical settings, for example, spatial temperature monitoring for treatments.

Lack of cellular contexts besides vasculature

PA imaging is ideal for vasculature visualization, because hemoglobin is the dominant optical absorber in biological soft tissue. However, usually no cellular contexts can be visualized with label-free PA imaging, despite other optical absorbing structures exist, such as melanin, lipids, DNA etc [66]. Morphology at cellular level can be vital for fundamental research and clinical studies. For example, despite the chaotic angiogenesis is considered a hallmark of tumor [3],

morphological change in pathology is still the most important factor for cancer diagnosis. Cancerous cells share similarities such as large nucleus, irregular size and shape, prominent nucleoli, scarce cytoplasm, and either intense color or pale [84]. None of these can be observed with conventional PA imaging systems. PA imaging has been employed to image tumor angiogenesis [72][73]. Chen et al. [85] used PAM system to evaluate angiogenesis inhibitor. Whereas blood vessel structure were quantitatively observed, visualized cellular structures can be used to enrich these studies by locating the cancerous tissue, evaluating treatment efficacy by studying the interaction between angiogenesis and tumor growth, etc.

Long data acquisition time in scanning PAM imaging

PA imaging is fundamentally a fast imaging technique [66]. For each A-scan in scanning PAM imaging, the only time restriction come from the time of flight of the PA acoustic waves from the internal acoustic source in the object to the sensing device. However, point-to-point raster scanning could be rather time consuming. Conventional PAM system employs mechanical scanning of either the object or the bulky imaging head, which consists of the ultrasonic detecting device and the optical focusing components [45] [44] [53]. Therefore the data acquisition time is limited by 1) mechanical scanning speed and 2) laser pulse repetition rate and 3) data transfer. Usually, mechanical scanning is slow, which restrict the overall imaging speed. For example, in the first report of OR-PAM, to image a $1\text{ mm} \times 1\text{ mm}$ -FOV with a pixel size of $1.25\text{ }\mu\text{m}$, 10 min is needed [44]. It took the second generation OR-PAM by Hu et al. 70 min to image an ear of $7.8\text{ mm} \times 10\text{ mm}$ [53]. In [50], 1 s is needed for each A-scan line scanning. Optical scanning is proposed to speed up data acquisition [61]. However, whereas raster scanning is significantly faster, a trade-off between SNR and FOV always exists. There are also hybrid scanning reported, which use optical scanning in 1 direction and mechanical in the

other axis [60][62]. However, the FOV of these systems is limited in at least one direction.

Bibliography

- [1] B. R. Zetter, “Angiogenesis and tumor metastasis,” *Annu. Rev. Med.*, vol. 49, no. 1, pp. 407–424, Jan. 1998.
- [2] P. Carmeliet, D. Ph, and M. Baes, “Metabolism and Therapeutic Angiogenesis,” pp. 2511–2512, 2008.
- [3] R. S. Kerbel, “Tumor angiogenesis: past, present and the near future,” *Carcinogenesis*, vol. 21, no. 3, pp. 505–15, Mar. 2000.
- [4] N. Weidner, J. P. Semple, W. R. Welch, and J. Folkman, “Tumor angiogenesis and metastasis - correlation in invasive breast carcinoma,” vol. 324, no. 1, pp. 1–8, 1991.
- [5] B. Al-husein, M. Abdalla, D. Pharm, M. Trepte, D. L. Deremer, P. R. Somanath, and D. Ph, “Antiangiogenic Therapy for Cancer : An Update,” 2004.
- [6] R. S. Kerbel, “Tumor Angiogenesis,” vol. 18, pp. 2039–2049, 2008.
- [7] J. P. Celli, B. Q. Spring, I. Rizvi, C. L. Evans, K. S. Samkoe, S. Verma, B. W. Pogue, and T. Hasan, “Imaging and photodynamic therapy: mechanisms, monitoring, and optimization,” *Chem. Rev.*, vol. 110, no. 5, pp. 2795–838, May 2010.
- [8] D. E. J. G. J. Dolmans, D. Fukumura, and R. K. Jain, “Photodynamic therapy for cancer,” *Nat. Rev. Cancer*, vol. 3, no. 5, pp. 375–80, May 2003.

- [9] H. Qiu, Y. Zhou, Y. Gu, Q. Ang, S. Zhao, Y. Wang, J. Zeng, and N. Huang, "Monitoring Microcirculation Changes in Port Wine Stains During Vascular Targeted Photodynamic Therapy by Laser Speckle Imaging," *Photochem. Photobiol.*, vol. 88, no. 4, pp. 978–984, Jul. 2012.
- [10] K. Kurohane, a Tominaga, K. Sato, J. R. North, Y. Namba, and N. Oku, "Photodynamic therapy targeted to tumor-induced angiogenic vessels.," *Cancer Lett.*, vol. 167, no. 1, pp. 49–56, Jun. 2001.
- [11] B. Li, Z. Qiu, and Z. Huang, "Advanced optical techniques for monitoring dosimetric parameters in photodynamic therapy," vol. 8553, p. 85530F, Dec. 2012.
- [12] M. P. Hartung, T. M. Grist, and C. J. François, "Magnetic resonance angiography: current status and future directions," *J. Cardiovasc. Magn. Reson.*, vol. 13, no. 19, pp. 1–11, 2011.
- [13] A. F. Kopp, S. Schroeder, A. Kuettner, A. Baumbach, C. Georg, R. Kuzo, M. Heuschmid, B. Ohnesorge, K. R. Karsch, and C. D. Claussen, "Non-invasive coronary angiography with high resolution multidetector-row computed tomography," *Eur. Heart J.*, vol. 23, no. 21, pp. 1714–1725, Nov. 2002.
- [14] A. J. Einstein, M. J. Henzlova, and S. Rajagopalan, "Estimating risk of cancer associated with radiation exposure from 64-slice computed tomography coronary angiography," *JAMA*, vol. 298, no. 3, pp. 317–323, Jul. 2007.

- [15] F. Joshi, D. Rosenbaum, S. Bordes, and J. H. F. Rudd, "Vascular imaging with positron emission tomography," *J. Intern. Med.*, vol. 270, no. 2, pp. 99–109, Aug. 2011.
- [16] S. Valable, E. Petit, S. Roussel, L. Marteau, J. Toutain, D. Divoux, F. Sobrio, J. Delamare, L. Barré, and M. Bernaudin, "Complementary information from magnetic resonance imaging and (18)F-fluoromisonidazole positron emission tomography in the assessment of the response to an antiangiogenic treatment in a rat brain tumor model," *Nucl. Med. Biol.*, vol. 38, no. 6, pp. 781–93, Aug. 2011.
- [17] R. S. C. Cobbold, *Foundations of Biomedical Ultrasound*. Oxford University Press, 2006.
- [18] S. Ohlerth, D. Laluehová, J. Buchholz, M. Roos, H. Walt, and B. Kaser-Hotz, "Changes in vascularity and blood volume as a result of photodynamic therapy can be assessed with power Doppler ultrasonography," *Lasers Surg. Med.*, vol. 38, no. 3, pp. 229–234, Mar. 2006.
- [19] G. S. Mintz, S. E. Nissen, W. D. Anderson, S. R. Bailey, J. Abrams, and C. M. Tracy, "American College of Cardiology Clinical Expert Consensus Document on Standards for Acquisition, Measurement and Reporting of Intravascular Ultrasound Studies (IVUS)," vol. 37, no. 5, pp. 1478–1492, 2001.

- [20] S. M. Srinivas, J. S. Nelson, N. Prakash, and R. D. Frostig, "Optical Doppler tomography," *IEEE J. Sel. Top. Quantum Electron.*, vol. 5, no. 4, pp. 1134–1142, 1999.
- [21] A. Major, S. Kimel, S. Mee, T. E. Milner, D. J. Smithies, S. M. Srinivas, and J. S. Nelson, "Microvascular photodynamic effects determined in vivo using optical Doppler tomography," *IEEE J. Sel. Top. Quantum Electron.*, vol. 5, no. 4, pp. 1168–1175, 1999.
- [22] J. Tyrrell, C. Thorn, A. Shore, S. Campbell, and A. Curnow, "Oxygen saturation and perfusion changes during dermatological methylaminolaevulinate photodynamic therapy," *Br. J. Dermatol.*, vol. 165, no. 6, pp. 1323–1331, Dec. 2011.
- [23] D. D. Duncan, S. J. Kirkpatrick, M. Larsson, T. Stromberg, and O. B. Thompson, "Laser speckle contrast imaging : theoretical and practical limitations David Briers Laser speckle contrast imaging : theoretical and practical limitations," *J. Biomed. Opt.*, vol. 18, no. 6, p. 066018, 2013.
- [24] M. Xu and L. V. Wang, "Photoacoustic imaging in biomedicine," *Rev. Sci. Instrum.*, vol. 77, no. 4, p. 041101, 2006.
- [25] A. G. Bell, "Selenium and the Photophone," *Nature*, vol. 22, pp. 500–503, 1880.
- [26] K. Maslov, H. F. Zhang, S. Hu, and L. V. Wang, "optical-resolution confocal photoacoustic microscopy," in *proceedings of SPIE*, 2008, vol. 6856, p. 68561I–68561I–7.

- [27] X. Wang, Y. Xu, M. Xu, S. Yokoo, E. S. Fry, and L. V. Wang, "Photoacoustic tomography of biological tissues with high cross-section resolution: Reconstruction and experiment," *Med. Phys.*, vol. 29, no. 12, pp. 2799–2805, 2002.
- [28] R. A. Kruger, W. L. J. Kiser, D. R. Reinecke, and G. A. Kruger, "Thermoacoustic computed tomography using a conventional linear transducer array," *Med. Phys.*, vol. 30, no. 5, pp. 856–860, 2003.
- [29] J. J. Niederhauser, M. Jaeger, R. Lemor, P. Weber, and M. Frenz, "Combined ultrasound and optoacoustic system for real-time high-contrast vascular imaging in vivo," *IEEE Trans. Med. Imaging*, vol. 24, no. 4, pp. 436–440, Apr. 2005.
- [30] P. Ephrat, L. Keenliside, A. Seabrook, F. S. Prato, and J. J. L. Carson, "Three-dimensional photoacoustic imaging by sparse-array detection and iterative image reconstruction," *J. Biomed. Opt.*, vol. 13, no. 5, p. 054052, 2014.
- [31] J. Gamelin, D. Castillo, and L. V Wang, "Curved array photoacoustic tomographic system for small animal imaging," vol. 13, no. April, pp. 1–10, 2008.
- [32] J. Gamelin, A. Maurudis, A. Aguirre, F. Huang, P. Guo, L. V Wang, and Q. Zhu, "A real-time photoacoustic tomography system for small animals," *Opt. Express*, vol. 17, no. 13, pp. 10489–10498, Jun. 2009.
- [33] J. Yao, J. Xia, K. I. Maslov, M. Nasiriavanaki, V. Tsytsarev, A. V Demchenko, and L. V Wang, "Noninvasive photoacoustic computed

- tomography of mouse brain metabolism in vivo.,” *Neuroimage*, vol. 64, pp. 257–266, Jan. 2013.
- [34] R. A. Kruger, R. B. Lam, D. R. Reinecke, S. P. Del Rio, and R. P. Doyle, “Photoacoustic angiography of the breast,” *Med. Phys.*, vol. 37, no. 11, pp. 6096–6100, 2010.
- [35] L. Xiang, B. Wang, L. Ji, and H. Jiang, “4-D photoacoustic tomography,” *Sci. Rep.*, vol. 3, no. 1113, pp. 1–8, Jan. 2013.
- [36] M. Xu and L. V Wang, “Time-Domain Reconstruction for Thermoacoustic Tomography in a Spherical Geometry,” vol. 21, no. 7, pp. 814–822, 2002.
- [37] M. Xu and L. Wang, “Universal back-projection algorithm for photoacoustic computed tomography,” *Phys. Rev. E*, vol. 71, no. 1, p. 016706, Jan. 2005.
- [38] G. Paltauf, J. a. Viator, S. a. Prahl, and S. L. Jacques, “<title>Iterative reconstruction method for three-dimensional optoacoustic imaging</title>,” *J. Opt. Soc. Am. A. Opt. Image Sci. Vis.*, vol. 112, no. 4, pp. 1136–1144, Jun. 2002.
- [39] K. Wang, R. Su, A. a Oraevsky, and M. a Anastasio, “Investigation of iterative image reconstruction in three-dimensional optoacoustic tomography,” *Phys. Med. Biol.*, vol. 57, no. 17, pp. 5399–5423, Sep. 2012.
- [40] L. Yao and H. Jiang, “Enhancing finite element-based photoacoustic tomography using total variation minimization,” *Appl. Opt.*, vol. 50, no. 25, p. 5031, Aug. 2011.

- [41] J. Provost and L. Frederic, "The Application of Compressed Sensing for photo-acoustic tomography," *IEEE Trans. Med. Imaging*, vol. 28, no. 4, pp. 585–594, 2009.
- [42] Z. Guo, "Quantification and Reconstruction in Photoacoustic Tomography," 2012.
- [43] K. Maslov and L. V Wang, "In vivo dark-field reflection-mode photoacoustic," vol. 30, no. 6, pp. 625–627, 2005.
- [44] K. Maslov, H. F. Zhang, S. Hu, and L. V Wang, "Optical-resolution photoacoustic microscopy for in vivo imaging of single capillaries," *Opt. Lett.*, vol. 33, no. 9, pp. 929–931, May 2008.
- [45] H. F. Zhang, K. Maslov, G. Stoica, and L. V Wang, "Functional photoacoustic microscopy for high-resolution and noninvasive in vivo imaging," *Nat. Biotechnol.*, vol. 24, no. 7, pp. 848–851, Jul. 2006.
- [46] H. F. Zhang, K. Maslov, M.-L. Li, G. Stoica, and L. V Wang, "In vivo volumetric imaging of subcutaneous microvasculature by photoacoustic microscopy," *Opt. Express*, vol. 14, no. 20, pp. 9317–9323, Oct. 2006.
- [47] J.-T. Oh, M.-L. Li, H. F. Zhang, K. Maslov, G. Stoica, and L. V Wang, "Three-dimensional imaging of skin melanoma in vivo by dual-wavelength photoacoustic microscopy," *J. Biomed. Opt.*, vol. 11, no. 3, p. 34032, 2006.
- [48] R. J. Zemp, L. Song, R. Bitton, K. K. Shung, and L. V Wang, "Realtime photoacoustic microscopy of murine cardiovascular dynamics," *Opt. Express*, vol. 16, no. 22, pp. 18551–18556, Oct. 2008.

- [49] R. J. Zemp, R. Bitton, M.-L. Li, K. K. Shung, G. Stoica, and L. V Wang, "Photoacoustic imaging of the microvasculature with a high-frequency ultrasound array transducer.," *J. Biomed. Opt.*, vol. 12, no. 1, p. 010501, 2007.
- [50] E. Zhang, J. Laufer, and P. Beard, "Backward-mode multiwavelength photoacoustic scanner using a planar Fabry-Perot polymer film ultrasound sensor for high-resolution three-dimensional imaging of biological tissues.," *Appl. Opt.*, vol. 47, no. 4, pp. 561–77, Feb. 2008.
- [51] J. Laufer, E. Zhang, G. Raivich, and P. Beard, "Three-dimensional noninvasive imaging of the vasculature in the mouse brain using a high resolution photoacoustic scanner," vol. 48, no. 10, pp. 299–306, 2009.
- [52] J. Laufer, P. Johnson, E. Zhang, B. Treeby, B. Cox, B. Pedley, and P. Beard, "In vivo preclinical photoacoustic imaging of tumor vasculature development and therapy," *J. Biomed. Opt.*, vol. 17, no. 5, p. 056016, May 2012.
- [53] S. Hu, K. Maslov, and L. V. Wang, "Second-generation optical-resolution photoacoustic microscopy with improved sensitivity and speed," *Opt. Lett.*, vol. 36, no. 7, pp. 1134–1136, 2011.
- [54] S. Hu, K. Maslov, V. Tsytarev, and L. V Wang, "Functional transcranial brain imaging by optical-resolution photoacoustic microscopy," *J. Biomed. Opt.*, vol. 14, no. 4, p. 040503, 2009.

- [55] S. Hu, K. Maslov, and L. V Wang, "Noninvasive label-free imaging of microhemodynamics by optical-resolution photoacoustic microscopy," *Opt. Express*, vol. 17, no. 9, pp. 7688–93, Apr. 2009.
- [56] W. Shi, P. Shao, P. Hajireza, A. Forbrich, and R. J. Zemp, "In vivo dynamic process imaging using real-time optical-resolution photoacoustic microscopy," *J. Biomed. Opt.*, vol. 18, no. 2, p. 26001, Feb. 2013.
- [57] S. Hu, K. Maslov, and L. V. Wang, "In vivo functional chronic imaging of a small animal model using optical-resolution photoacoustic microscopy," *Med. Phys.*, vol. 36, no. 6, p. 2320, 2009.
- [58] C. He, P. Agharkar, and B. Chen, "Intravital microscopic analysis of vascular perfusion and macromolecule extravasation after photodynamic vascular targeting therapy," *Pharm. Res.*, vol. 25, no. 8, pp. 1873–80, Aug. 2008.
- [59] S. Hu, B. Rao, K. Maslov, and L. V Wang, "Label-free photoacoustic ophthalmic angiography," *Opt. Lett.*, vol. 35, no. 1, pp. 1–3, Jan. 2010.
- [60] B. Rao, L. Li, K. Maslov, and L. Wang, "Hybrid-scanning optical-resolution photoacoustic microscopy for in vivo vasculature imaging," vol. 35, no. 10, pp. 1521–1523, 2010.
- [61] Z. Xie, S. Jiao, H. F. Zhang, and C. A. Puliafito, "Laser-scanning optical-resolution photoacoustic microscopy," *Opt. Lett.*, vol. 34, no. 12, pp. 1771–1773, 2009.

- [62] L. Wang, K. Maslov, J. Yao, B. Rao, and L. V Wang, "Fast voice-coil scanning optical-resolution photoacoustic microscopy," *Opt. Lett.*, vol. 36, no. 2, pp. 139–141, Jan. 2011.
- [63] P. Hajireza, W. Shi, and R. J. Zemp, "Label-Free In Vivo GRIN-Lens Optical Resolution Photoacoustic Micro-Endoscopy," *Laser Phys. Lett.*, vol. 5, no. 10, p. 055603, 2013.
- [64] W. Shi, P. Hajireza, P. Shao, A. Forbrich, and R. J. Zemp, "In vivo near-realtime volumetric optical-resolution photoacoustic microscopy using a high-repetition-rate nanosecond fiber-laser.," *Opt. Express*, vol. 19, no. 18, pp. 17143–50, Aug. 2011.
- [65] W. Shi, S. Kerr, I. Utkin, J. Ranasinghesagara, L. Pan, Y. Godwal, R. J. Zemp, and R. Fedosejevs, "Optical resolution photoacoustic microscopy using novel high-repetition-rate passively Q-switched microchip and fiber lasers.," *J. Biomed. Opt.*, vol. 15, no. 5, p. 056017, 2014.
- [66] L. V. Wang, "Photo acoustic tomography," *Scholarpedia*. p. 10278, 2014.
- [67] L. V. Wang and H. Wu, *Biomedical Optics, principles and imaging*. Willey-Interscience, 2007.
- [68] H. F. Zhang, K. Maslov, M. Sivaramakrishnan, G. Stoica, and L. V. Wang, "Imaging of hemoglobin oxygen saturation variations in single vessels in vivo using photoacoustic microscopy," *Appl. Phys. Lett.*, vol. 90, no. 5, p. 053901, 2007.

- [69] S. Ashkenazi, "Photoacoustic lifetime imaging of dissolved oxygen using methylene blue.," *J. Biomed. Opt.*, vol. 15, no. 4, p. 040501, 2010.
- [70] S. Ashkenazi, S.-W. Huang, T. Horvath, Y.-E. L. Koo, R. Kopelman, and R. Kopelman, "Photoacoustic probing of fluorophore excited state lifetime with application to oxygen sensing.," *J. Biomed. Opt.*, vol. 13, no. 3, p. 034023, 2011.
- [71] G. Ku, X. Wang, X. Xie, G. Stoica, and L. V Wang, "Imaging of tumor angiogenesis in rat brains in vivo by photoacoustic tomography," *Appl. Opt.*, vol. 44, no. 5, pp. 770–775, Feb. 2005.
- [72] L. Xiang, D. Xing, H. Gu, F. Zhou, D. Yang, L. Zeng, and S. Yang, "In vivo monitoring of neovascularization in tumor angiogenesis by photoacoustic tomography," *Chinese Opt. Lett.*, vol. 24, no. 3, pp. 751–754, 2007.
- [73] S. Hu, S. Oladipupo, J. Yao, A. C. Santeford, K. Maslov, J. Kovalski, J. M. Arbeit, and L. V. Wang, "Optical-resolution photoacoustic microscopy of angiogenesis in a transgenic mouse model," in *proceedings of SPIE*, 2010, vol. 7564, pp. 756406–756406–5.
- [74] L. Xiang, D. Xing, H. Gu, D. Yang, S. Yang, L. Zeng, and W. R. Chen, "Real-time optoacoustic monitoring of vascular damage during photodynamic therapy treatment of tumor," *J. Biomed. Opt.*, vol. 12, no. 1, p. 014001, 2007.

- [75] B. Cox, J. G. Laufer, S. R. Arridge, and P. C. Beard, “Quantitative spectroscopic photoacoustic imaging: a review,” *J. Biomed. Opt.*, vol. 17, no. 6, p. 061202, Jun. 2012.
- [76] K.-H. Chow, R. E. Factor, and K. S. Ullman, “The nuclear envelope environment and its cancer connections,” *Nat. Rev. Cancer*, vol. 12, no. 3, pp. 196–209, 2012.
- [77] B. T. Cox, S. R. Arridge, K. P. Köstli, and P. C. Beard, “two-dimensional quantitative photoacoustic image reconstruction of absorption distribution in scattering media by use of a simple iterative method,” pp. 4–6, 2006.
- [78] Z. Yuan and H. Jiang, “Quantitative photoacoustic tomography,” *Philos. Trans. A. Math. Phys. Eng. Sci.*, vol. 367, no. 1900, pp. 3043–3054, Aug. 2009.
- [79] T. Jetzfellner, D. Razansky, A. Rosenthal, R. Schulz, K.-H. Englmeier, and V. Ntziachristos, “Performance of iterative optoacoustic tomography with experimental data,” *Appl. Phys. Lett.*, vol. 95, no. 1, p. 013703, 2009.
- [80] Z. Guo, S. Hu, and L. V Wang, “Calibration-free absolute quantification of optical absorption coefficients using acoustic spectra in 3D photoacoustic microscopy of biological tissue,” *Opt. Lett.*, vol. 35, no. 12, pp. 2067–9, Jun. 2010.
- [81] G. Bal and K. Ren, “Multi-source quantitative photoacoustic tomography in a diffusive regime,” *Inverse Probl.*, vol. 27, no. 7, p. 075003, Jul. 2011.

- [82] B. T. Cox, S. R. Arridge, and P. C. Beard, "Estimating chromophore distributions from multiwavelength photoacoustic images," *J. Opt. Soc. Am. A. Opt. Image Sci. Vis.*, vol. 26, no. 2, pp. 443–55, Feb. 2009.
- [83] B. T. Cox, J. G. Laufer, and P. C. Beard, "<title>The challenges for quantitative photoacoustic imaging</title>," vol. 7177, pp. 717713–717713–9, Feb. 2009.
- [84] A. L. Baba and C. Catio, *Comparative Oncology*, First edit. Bucharest: The Publishing House of the Romanian Academy, 2007.
- [85] S.-L. Chen, J. Burnett, D. Sun, X. Wei, Z. Xie, and X. Wang, "Photoacoustic microscopy: a potential new tool for evaluation of angiogenesis inhibitor," *Biomed. Opt. Express*, vol. 4, no. 11, pp. 2657–66, Jan. 2013.

3. Estimating Optical Absorption, Scattering, and Grüeneisen Distributions with Multiple-Illumination Photoacoustic Tomography (MI-PAT)¹

3.1 Introduction

Photoacoustic tomography (PAT) is a unique new imaging technology capable of generating images with high optical contrast, fine ultrasonic spatial resolution, and good imaging depth [1]. Despite its recent attention in the bio-imaging community, presently, quantitative reconstruction of optical properties in photoacoustic imaging is rather challenging due to several reasons. First, photoacoustic signals emitted from a subcutaneous location are proportional to the unknown optical fluence, which is in turn, a function of the distributed optical properties to be estimated. This introduces a non-linear relationship between the measured signals and the optical properties to be recovered. Second, a given optically-induced heating distribution could be produced by multiple possible optical property distributions. Furthermore, the Grüeneisen parameters may vary between tissue types. The present project proposes an inversion methodology which addresses each of these challenges.

A number of methods have emerged for quantitative estimation of optical properties using photoacoustics. Cox B. T. et al. [2] proposed to recover absorption coefficient distribution with a fixed-point iterative inversion scheme when the

¹ A version of this chapter has been published. Reprint with permission from: P. Shao, B. Cox and R. J. Zemp, *Appl. Opt.*, 50(19), p.3145-3154, 2011. Copyright 2011 OSA.

scattering distribution is known. Yuan Z. and Jiang H. [3] reconstructed absorption coefficient map based on the finite-element solution to diffuse equation. Ripoll J. and Ntziachristos V. [4] also described an iterative diffusion-regime inverse method, which can recover small perturbations in the absorption coefficient distribution when the optical properties of the background turbid medium are known. Jetzfellner T. et al. [5] investigated the experimental performance of an iterative approach and found that it was sensitive to errors in the scattering coefficient. Banerjee B. et al. [6] proposed a non-iterative scheme to recover the absorption coefficient map, which is applicable to only highly scattering media. Yin L. et al. [7] suggested iteratively estimating absorbed energy density with photoacoustic tomography (PAT) and the interior fluence distribution with diffusing light measurements, and then calculating the absorption coefficient with quotient of the two quantities. Yuan Z. et al. [8] proposed the use of a method based on diffusion equation with *a priori* structural information from PAT images serving as a means of regularization. Unfortunately, the PAT image may be biased by the nonuniform fluence and thus the *a priori* structural information from the PAT image may not be reliable. Cox B. T. et al. [9] further extended the work of previous literature to the case where both absorption and reduced scattering coefficients were unknown. He showed that multiple optical wavelengths, with prior information about the wavelength-dependence of the optical scattering, could overcome non-uniqueness and estimate chromophore distributions quantitatively, albeit with some numerical challenges. Guo Z. et al. [10] proposed a self-calibrating method to quantify absorption coefficient. By taking the ratio of acoustic spectrals of two optical wave lengths, factors such as system bandwidth and acoustic attenuation are canceled out. This method is robust to absolute fluence variations. However, it requires the fluence to follow the Beer-Lambert law and so is not generally applicable to heterogeneous

media. With the exception of the DOT (Diffuse Optical Tomography)-PAT hybrid technologies [7], the literature cited thus far has considered only a single optical illumination location.

One of the common elements lacking in the above noted literature is the inability to decouple the Grüneisen parameter from the reconstructed optical parameter distributions. The Grüneisen parameter Γ is a unitless thermodynamical parameter quantifying the efficiency of conversion between thermal energy to acoustic energy. It is given as $\Gamma = \beta c^2 / C_p$, where β is the the volume thermal expansivity of the tissue, c is the speed of sound in the tissue, and C_p is the specific heat capacity at a constant pressure. While most reconstruction strategies assume that the Grüneisen parameter is considered spatially constant, Cox B. T. et al. [11] point out that the Grüneisen parameter may vary considerably between tissue types such as fat and blood.

Additionally, the Grüneisen parameter is highly temperature dependent, and several groups have shown how photoacoustics can track temperature changes by tracking variations in photoacoustic amplitude with temperature [12] [13] [14] [15] [16] [17] [18] [19]. In applications such as thermal therapy, where imaging of local heating is desired, the Grüneisen coefficient may be spatially varying, and may change as much as a few percent per degree Celcius temperature rise [13]. To our knowledge, recent articles investigating photoacoustic thermometry choose to track only changes in the photoacoustic signals due to temperature sensitivity of the Grüneisen parameter, and do not consider the reconstruction of this parameter. As with other temperature imaging methods [20] [21] [22] [23] [24], those methods requiring pre- and post-heating images are susceptible to motion artifacts and other physiological changes which often confound reliable temperature estimates. Imaging of the Grüneisen parameter may lead to opportunities for quantifying

temperature distributions without confounding issues of tissue motion, although this remains to be seen.

There has been little work done in quantitative photoacoustic reconstruction of optical properties when multiple optical source locations are involved. Zemp R. J. et al. [25] and Ranasinghesagara J. et al. [26] described a simple method for estimating optical scattering properties of turbid media using multiple surface illumination locations. That work also described a design for flexible light delivery with accompanying photoacoustic detection. Multiple optical sources are routinely used in DOT. Multiple source-detector pair measurements are collected and then reconstructed to form images of absorption, scattering, and fluorescence with this technique. Unfortunately, DOT is limited to light collection from surface-detectors. One potential advantage of multiple-optical-source photoacoustic imaging is that for each optical source, photoacoustic detection effectively provides an optical fluence measurement at each subsurface location and hence sub-surface points can be viewed as virtual detectors. Bal G. and Uhlmann G. [27] showed mathematically that absorption and diffusion coefficients can, in principle, be stably constructed from “internal data” corresponding to “ $2n$ well-chosen boundary conditions”, where n is the dimension. By “internal data” they mean PAT images and by “boundary conditions” they mean illumination patterns. Their work, however, provided no computational or experimental studies nor a way to find the “well-chosen boundary conditions”. Our work could be viewed as a first step in assessing the practicality of concepts they discuss, but from a very different theoretical perspective.

We recently proposed a novel reconstruction methodology utilizing faithful photoacoustic reconstructions of initial pressure distributions due to spatially distinct multiple illuminations (MI) [28]. We call the technique multiple-

illumination photoacoustic tomography (MI-PAT). We showed that absolute reconstructions of absorption coefficient perturbations is possible with simulated data, and that these MI-PAT reconstructions are robust to spatially-varying Grüeneisen coefficients.

Building on that success, the goal of this paper is to show that photoacoustic imaging with multiple optical illumination locations (sources) can provide quantitative estimates of tissue optical absorption and scattering perturbations with ultrasonic spatial resolution. For a given optical illumination geometry, a heating distribution can be reconstructed via photoacoustic tomography. The heating distribution can, however, be due to multiple possible absorption-scattering distribution pairs, hence, non-uniqueness confounds quantitative reconstruction methods when both absorption and scattering distributions are unknown. We demonstrate that alternative illumination geometries can alleviate this type of ill-posedness, and that distributions of the optical absorption and diffusion coefficients may be faithfully reconstructed, albeit with some numerical challenges. This is the first report of, to our knowledge, a framework for reconstruction of both absorption and scattering coefficient distributions in a known turbid-tissue with a single optical wavelength. Suggestions for further reducing ill-conditioning are discussed. One unique aspect of our framework is that our reconstruction methods are immune to, and able to recover spatially-varying Grüeneisen parameter distributions, which may be important in practice due to large variations in this parameter for different tissue types or when temperature varies in an imaging subject. We also compare conditioning (singular values) of our methods with Continuous-Wave Diffuse Optical Tomography (CW-DOT) and show that MI-PAT is orders of magnitude less ill-posed.

3.2 Theory

We assume that the true subcutaneous heating distribution at object location \mathbf{r} due to a laser pulse incident at location \mathbf{r}_{s_i} is given as

$$h_i(\mathbf{r}) = \mu_a(\mathbf{r})\Phi(\mathbf{r}, \mathbf{r}_{s_i}) \quad (3.1)$$

where μ_a and Φ are the optical absorption coefficient and the optical fluence, respectively. Local heating induces a thermoelastic expansion with initial photoacoustic pressure generation given as

$$p_i(\mathbf{r}) = \Gamma(\mathbf{r})\mu_a(\mathbf{r})\Phi(\mathbf{r}, \mathbf{r}_{s_i}) \quad (3.2)$$

where $\Gamma(\mathbf{r})$ is the Grüeneisen parameter as a function of object position. The initial pressure distribution can be reconstructed from received photoacoustic signals $g_i(\mathbf{r}_d, t)$ [1]

$$\hat{p}_i(\mathbf{r}) = O\{g_i(\mathbf{r}_d, t)\} \quad (3.3)$$

where O is a reconstruction operator, and where ultrasound detectors are located at locations \mathbf{r}_d and t is time.

The reconstructed photoacoustic image due to illumination s_i can be thought of as the true initial pressure distribution filtered by an imaging system, represented as functional operator H which is linear but not necessarily shift-invariant:

$$\hat{p}_i(\mathbf{r}) = H\{p_i(\mathbf{r})\} + n = H\{\Gamma(\mathbf{r})\mu_a(\mathbf{r})\Phi_i(\mathbf{r})\} + n \quad (3.4)$$

where n is additive noise and we use the abbreviated notation $\Phi(\mathbf{r}, \mathbf{r}_{s_i}) = \Phi_i(\mathbf{r})$.

When the reconstruction is ideal, H is modeled as a linear shift-invariant delta function. In general, however, H is linear and shift-variant.

3.2.1 Problem of absorption-scattering non-uniqueness

Arridge S. and Lionheart W. [29] showed that in DOT there is a non-uniqueness between optical absorption and scattering, to the extent that it is not possible to recover a unique internal absorption distribution from d.c. measurements of the boundary fluence unless the scattering is known. Does the same non-uniqueness plague photoacoustic tomography (PAT)? The situation differs in two ways: first, the data for the optical inversion in PAT consists of measurements proportional to absorbed energy, h , rather than the fluence Φ , so the data depends more strongly on absorption than scattering; second, the data consists of internal measurements, i.e., the initial pressure is known for all interior points in contrast to DOT's measurements of Φ on the boundary. Despite these differences, a similar non-uniqueness does affect PAT, although this has yet to be proven analytically. Numerical examples calculated by minimizing an error functional are given in Fig. 3.1 and Ref [9].

Figure 3.1 shows two pairs of absorption and scattering distributions with background absorption coefficients of 0.02 cm^{-1} and reduced scattering coefficients of 5 cm^{-1} . Absorption coefficient A has a circular heterogeneity of 1.2 cm^{-1} . Reduced scattering coefficient A is constant at the background value in contrast to reduced scattering coefficient B which has the two circular scattering heterogeneities with $\mu_s' = 15 \text{ cm}^{-1}$. Absorption coefficient B was calculated to ensure that the absorbed energy distributions resulting from placing a point source centrally at the top of the $20 \times 20 \text{ mm}$ domain were identical to machine precision.

The calculations were performed using a finite element model of light transport [30] on a 40×40 element square mesh, with a boundary condition of zero incoming photon current.

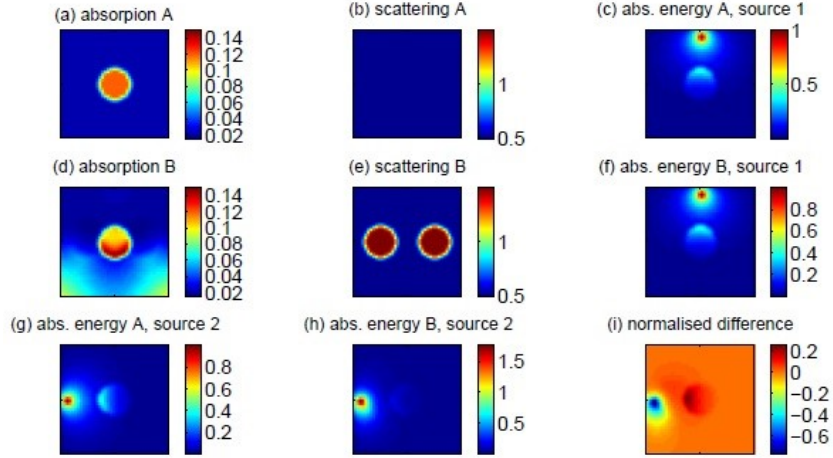


Fig. 3.1. The absorption-scattering non-uniqueness problem in quantitative photoacoustic tomography. Give heating distributions (c) = (f) can be produced by the $\{\mu_a, \mu'_s\}$ distributions A {(a), (b)} or B {(d), (e)}. Because two pairs of absorption and scattering distributions, A and B, can produce the same heating distribution for a given optical illumination geometry, approaches attempting to reconstruct optical properties using single-illumination PAT are ill-posed due to nonuniqueness. However, when illuminated by a spatially distinct alternate optical source (source 2), the heating distribution from A is distinct from that of B. The error image (difference) between (g) and (h) is shown in (i). This example demonstrates the potential to remedy nonuniqueness using multiple sources.

This example shows that non-uniquenesses can appear in PAT when a single optical source is used to illuminate the sample. This makes the extraction of quantitative estimates of absorption coefficient from absorbed energy distributions difficult, if not impossible. Additional independent information is necessary in order to mitigate the non-uniqueness. As mentioned in the Introduction, Cox B. et al. [9] proposed using knowledge of the wavelength dependence of the scattering

in conjunction with multiple wavelengths to assist in recovering chromophore concentrations. Yin L. et al. [7] avoided the question of non-uniqueness by using DOT to estimate the fluence thereby allowing μ_a to be estimated from $\mu_a = h/\Phi$. Here, we propose using multiple illumination patterns to provide the extra information necessary to recover absorption coefficients.

3.2.2 Multiple-Illumination locations as a potential remedy for absorption-scattering non-uniqueness

The diffusive nature of light propagation in highly scattering media, and the resulting randomness of the photons within the tissue at depths greater than one scattering depth, might suggest that the position of the illuminating source is not a significant factor in determining a photoacoustic image at greater depths. However, when the illumination comes from just one direction, or from a small illumination region, the fluence can vary significantly within the tissue. This raises the prospect of obtaining extra information by taking PAT images of the same sample using different illumination patterns (here point sources of light are used for simplicity).

Figure 3.1 (g) and (h) show the absorbed energy distributions generated from the pair of absorption and scattering coefficients calculated in the previous section but with the point source positioned centrally at the left of the image, rather than at the top. There are clearly significant differences in the images: not just around the point source itself, which is perhaps unsurprising, but also at a depth of 10 mm at the position of the absorption heterogeneity. This suggests that a set of PAT images obtained with sufficiently independently placed sources might contain sufficient additional information to enable the separation of μ_a and Φ .

3.2.3 Multiple-optical-source photoacoustic reconstruction Methodology for absorption and scattering perturbations in a known turbid

background

Here we consider the case where distributed absorbers perturb the fluence from the homogenous case such that

$$\Phi(\mathbf{r}_j, \mathbf{r}_{s_i}) = \Phi_0(\mathbf{r}_j, \mathbf{r}_{s_i}) + \Phi_{sc}(\mathbf{r}_j, \mathbf{r}_{s_i}) \quad (3.5)$$

where $\Phi(\mathbf{r}_j, \mathbf{r}_{s_i})$ is the fluence at location \mathbf{r}_j (with $j=1,2,\dots,J$) due to illumination spot at location \mathbf{r}_{s_i} . Figure 3.2 provides an illustration of the vector geometry of the problem. $\Phi_0(\mathbf{r}_j, \mathbf{r}_{s_i})$ is the fluence due to the known homogenous turbid background with absorption and reduced scattering coefficients $\{\mu_a, \mu_s'\}$ if no additional absorption or scattering perturbations were present, and $\Phi_{sc}(\mathbf{r}_j, \mathbf{r}_{s_i})$ is the fluence perturbation due to optical property variations. In this paper, we use the diffusion coefficient D , which is defined as $1/[3(\mu_a + \mu_s')]$ instead of μ_s' to depict scattering for simplicity. For both absorption and scattering perturbations such that $\mu_a(\mathbf{r}_j) = \mu_a + \delta\mu_a(\mathbf{r}_j)$ and $D(\mathbf{r}_j) = D + \delta D(\mathbf{r}_j)$ we have that [31]

$$\begin{aligned} \Phi_{sc}(\mathbf{r}_j, \mathbf{r}_{s_i}) = & - \int \frac{\delta\mu_a(\mathbf{r}')}{D_0} G_0(\mathbf{r}_j, \mathbf{r}') \Phi(\mathbf{r}', \mathbf{r}_{s_i}) d\mathbf{r}' \\ & + \int \frac{\delta D(\mathbf{r}')}{D_0} \nabla G_0(\mathbf{r}_j, \mathbf{r}') \cdot \nabla \Phi(\mathbf{r}', \mathbf{r}_{s_i}) d\mathbf{r}' \end{aligned} \quad (3.6)$$

where D_0 is the diffusion coefficient of the homogenous background, and $G_0(\mathbf{r}_j, \mathbf{r}')$ is the Green's function representing propagation from $\mathbf{r}_j \rightarrow \mathbf{r}'$. Using the first-order Born approximation, such that $\Phi_{sc} \ll \Phi_0$, we have that $\Phi \approx \Phi_0$. Although this limits the inversion to the linear case, it is sufficient to show that multiple illumination ameliorates the nonuniqueness without the additional

complexity the nonlinearity imposes. For cases in which the linear assumption is not sufficient, this framework can be extended to the nonlinear case, as discusses in Section 3.4.

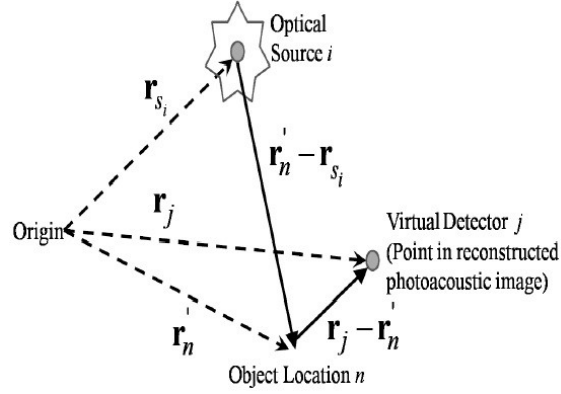


Fig. 3.2 Light propagation geometry

We can discretize the integral as

$$\Phi_{SC}(\mathbf{r}_j, \mathbf{r}_{s_i}) = \sum_n W_{\{ij\}n}^a \delta\mu_a(\mathbf{r}'_n) + \sum_n W_{\{ij\}n}^s \delta D(\mathbf{r}'_n) \quad (3.7)$$

with s_i represents a source index ($i = 1, 2, \dots, S$),

$$W_{\{ij\}n}^a = -G_0(\mathbf{r}_j, \mathbf{r}'_n) \Phi(\mathbf{r}'_n, \mathbf{r}_{s_i}) \nabla V / D_0 \quad (3.8)$$

and

$$W_{\{ij\}n}^s = \nabla G_0(\mathbf{r}_j, \mathbf{r}'_n) \cdot \nabla \Phi(\mathbf{r}'_n, \mathbf{r}_{s_i}) \Delta V / D_0 \quad (3.9)$$

where ∇V is a volume element. The $\{ij\}$ elements are grouped together in this way because they could be rasterized into a single index $k_{ij} = i + jS$ so that this may be written in matrix form as

$$\Phi_{SC} = \mathbf{W}\mathbf{u} \quad (3.10)$$

where $\mathbf{W} = [\mathbf{W}^a | \mathbf{W}^s]$ with \mathbf{W}^a and \mathbf{W}^s being $SJ \times N$ matrices corresponding to absorption and scattering, respectively. Here, $\mathbf{u} = [\delta\mu_a^T, \delta D^T]^T$, where $\delta\mu_a$ and δD are $N \times 1$ column vectors. For example, $\delta\mu_a = [\mu_a(\mathbf{r}'_1), \mu_a(\mathbf{r}'_2), \dots, \mu_a(\mathbf{r}'_N)]^T$. The locations $\{\mathbf{r}'_n: n = 1, 2, \dots, N\}$ could represent, for example, points on a mesh and represent locations at which optical properties are to be reconstructed.

If we multiply the expression for $\Phi_i(\mathbf{r}_j) \equiv \Phi(\mathbf{r}_j, \mathbf{r}_{s_i})$ by $\Gamma(\mathbf{r}_j)\mu_a(\mathbf{r}_j)$, we obtain the initial pressure distribution $p_i(\mathbf{r}_j)$ due to point source \mathbf{r}_{s_i} . Let us take a ratio of reconstructed initial pressure distribution estimates from photoacoustic images taken at source positions s_i and s_l . If we consider locations $\{\mathbf{r}_j: j=1, 2, \dots, J\}$, which have high signal-to-noise ratio (SNR) in the reconstructed image to avoid instability, then the ratio is well approximated as:

$$\frac{\hat{p}_i(\mathbf{r}_j)}{\hat{p}_l(\mathbf{r}_j)} \cong \frac{H\{\Phi_i(\mathbf{r}_j)\Gamma(\mathbf{r}_j)\mu_a(\mathbf{r}_j)\}}{H\{\Phi_l(\mathbf{r}_j)\Gamma(\mathbf{r}_j)\mu_a(\mathbf{r}_j)\}} \quad (3.11)$$

We now assume that the fluence distribution is slowly varying (essentially a constant) compared to the scale of a point-spread function, which should be a good approximation when absorption and scattering perturbations are not too strong. In

this case, if H is linear and noise is small enough to be negligible,

$$\hat{p}_i(\mathbf{r}_j) = \Phi_i(\mathbf{r})H\{\Gamma(\mathbf{r})\mu_a(\mathbf{r})\} \quad (3.12)$$

With this approximation the ratio becomes

$$\frac{\hat{p}_i(\mathbf{r}_j)}{\hat{p}_l(\mathbf{r}_j)} \cong \frac{\Phi_i(\mathbf{r}_j)}{\Phi_l(\mathbf{r}_j)} \quad (3.13)$$

Fortuitously the terms $H\{\Gamma(\mathbf{r}_j)\mu_a(\mathbf{r}_j)\}$ cancel and we are left with a ratio of fluences due to different illumination locations. By expanding these fluence distributions in terms of homogeneous and perturbation terms we have:

$$\frac{\hat{p}_i(\mathbf{r}_j)}{\hat{p}_l(\mathbf{r}_j)} \cong \frac{\Phi_0(\mathbf{r}_j, \mathbf{r}_{s_i}) + \Phi_{SC}(\mathbf{r}_j, \mathbf{r}_{s_i})}{\Phi_0(\mathbf{r}_j, \mathbf{r}_{s_i}) + \Phi_{SC}(\mathbf{r}_j, \mathbf{r}_{s_i})} \quad (3.14)$$

The local unknown absorption coefficients cancel and we are left with a ratio of fluences. The left-hand side represents a set of measurements, while the right-hand-side consists of model calculations. Then Φ_{SC} is expressed in terms of the distributed absorption perturbations and we can re-write Eq. 3.14 as

$$\begin{aligned} \Sigma_n[\hat{p}_i(\mathbf{r}_j)\mathbf{W}_{\{lj\}n} - \hat{p}_l(\mathbf{r}_j)\mathbf{W}_{\{ij\}n}]\mathbf{u}(\mathbf{r}'_n) \\ = \hat{p}_l(\mathbf{r}_j)\Phi_0(\mathbf{r}_j, \mathbf{r}_{s_i}) - \hat{p}_i(\mathbf{r}_j)\Phi_0(\mathbf{r}_j, \mathbf{r}_{s_i}) \end{aligned} \quad (3.15)$$

For S optical source locations $\{s_1, s_2, \dots, s_S\}$ we consider $S(S-1)/2$ unique pairs $\{(s_i, s_t), i \neq t\}$ of optical sources. In matrix form Eq. 3.15 is written as

$$\mathbf{Q}\mathbf{u}=\mathbf{b}. \quad (3.16)$$

where $\mathbf{Q} = [\mathbf{Q}^a | \mathbf{Q}^s]$ is a $[S(S-1)/2]J \times 2N$ matrix, where \mathbf{Q}^a has elements $[\mathbf{Q}^a]_{\{ilj\}n} = \hat{p}_i(\mathbf{r}_j)\mathbf{W}_{\{lj\}n}^a - \hat{p}_l(\mathbf{r}_j)\mathbf{W}_{\{ij\}n}^a$, and \mathbf{Q}^s has elements $[\mathbf{Q}^s]_{\{ilj\}n} = \hat{p}_i(\mathbf{r}_j)\mathbf{W}_{\{lj\}n}^s - \hat{p}_l(\mathbf{r}_j)\mathbf{W}_{\{ij\}n}^s$. These consist of measurements \hat{p} from the reconstructed photoacoustic image (due to different optical source positions), and model calculations based on a known homogenous background. \mathbf{b} is a $[S(S-1)/2]J \times 1$ column vector with elements $[\mathbf{b}]_{\{ilj\}} = \hat{p}_l(\mathbf{r}_j)\Phi_0(\mathbf{r}_j, \mathbf{r}_{s_i}) - \hat{p}_i(\mathbf{r}_j)\Phi_0(\mathbf{r}_j, \mathbf{r}_{s_t})$ which are a mixture of measurements and model calculations.

The unknown perturbations can be estimated quantitatively by inverting the linearized model via a Moore-Penrose pseudo-inverse: $\mathbf{u} = (\mathbf{Q}^T\mathbf{Q})^{-1}\mathbf{Q}^T\mathbf{b}$. We may alternatively need to use singular value decomposition to decompose the matrix \mathbf{Q} as $\mathbf{Q} = \mathbf{U}\mathbf{\Sigma}\mathbf{V}^T$, where $\mathbf{\Sigma}$ is a diagonal matrix of singular values of the same dimension as \mathbf{Q} , and \mathbf{U} and \mathbf{V} are unitary matrices consisting of columns of the “right” and “left” singular vectors \mathbf{u}_i and \mathbf{v}_i , respectively. The inversion is then given as $\mathbf{u} = \mathbf{V}\mathbf{\Sigma}^{-1}\mathbf{U}^T\mathbf{b} = \sum_i \frac{u_i^T \mathbf{b}}{\sigma_i} \mathbf{v}_i$. Tikhonov regularization or other regularization procedures may be used to avoid instabilities due to poor matrix conditioning. It should be noted that the above should produce absolute estimates of $\{\delta\mu_a(\mathbf{r}), \delta D(\mathbf{r})\}$.

3.2.4 Recovery of the spatially varying Grüeneisen parameter

With the ability to recover absorption coefficients perturbations quantitatively, in a way which is robust to spatially-varying Grüeneisen parameters, we can estimate the Grüeneisen coefficient distributions $\hat{\Gamma}(\mathbf{r}) = \frac{\hat{p}(\mathbf{r})}{\hat{\Phi}(\mathbf{r})\hat{\mu}_a(\mathbf{r})}$, where $\hat{p}(\mathbf{r})$ is the reconstructed photoacoustic image, $\hat{\mu}_a(\mathbf{r})$ is the reconstructed absolute absorption coefficient distribution, and $\hat{\Phi}(\mathbf{r})$ is the estimated fluence distribution (computed with knowledge of the absorption perturbations). To improve robustness to noise, we choose to use all illumination sources as follows:

$$\hat{\Gamma}(\mathbf{r}) = \frac{\sum_i \hat{p}_i(\mathbf{r})}{\hat{\mu}_a(\mathbf{r}) \sum_i \hat{\Phi}_i(\mathbf{r})} \quad (3.17)$$

where \hat{p}_i is the reconstructed photoacoustic image due to source i , and $\hat{\Phi}_i$ is the estimated fluence distribution due to source i .

3.3 Computational reconstruction

Two-dimensional simulations are considered here for simplicity. True absorption and diffusion-coefficient maps are simulated on a 20×20 grid spanning $2 \text{ cm} \times 2 \text{ cm}$, as shown in Figs. 3.3 (a) and (b), respectively. The grid sampling interval is 1 mm. The reduced scattering coefficient of the turbid background is taken as 10 cm^{-1} everywhere. The background absorption coefficient is taken as $\mu_a = 0.1 \text{ cm}^{-1}$, while two absorbing regions are taken to have a 0.025 cm^{-1} absorption perturbation. One region of increased diffusion coefficient (reduced scattering coefficient) corresponds to a $\delta\mu'_s = 0.9 \text{ cm}^{-1}$. Eight optical sources $\{s_1, s_2, \dots, s_8\}$, as is illustrated in Fig. 3.4, located 3-mm back from each edge around the object are simulated. The fluence due to source s_1 is shown in Fig. 3.3 (d). The 3-mm gap between the tissue surface and the reconstruction region permits isotropic

point-sources in an infinite medium to be used as a good approximation to the true pencil-beam illumination situation that would occur in an experiment. Photoacoustic images are simulated by multiplying the computed optical fluence distribution, Grüneisen parameter distribution and the absorption map, as shown in Fig. 3.3 (h). One way to estimate the absorption perturbations could be to estimate the local fluence as $\Phi_0(\mathbf{r})$, the fluence computed in a homogenous medium with no absorption perturbations. By normalizing the photoacoustic images by these fluence estimates, we produce estimates of the absorption map, as shown in Fig. 3.3 (i) for source s_1 as an example. These estimates possess unacceptable errors that we aim to correct with the reconstruction method described in this article. When we apply our algorithm to the “measured” photoacoustic images, we are able to produce a fairly good estimate of the optical absorption map, as shown in Fig. 3.3 (j). Reconstructed diffusion (scattering) distribution map is shown in (k). No cross-talk has been found in the two recovered maps. The maximum error without additive noise is less than 12 orders of magnitude below the true values. However, we find the reconstruction quality deteriorates quickly as the amount of noise increases, revealing sensitivity of the algorithm to noise. In the examples we show here, signal-to-noise ratio (SNR) of the simulation photoacoustic images at each detection location is no lower than 40 dB, and only data with SNR higher than 60 dB for each source pair are used for reconstruction to ensure the image quality. Key to numerical stability and robustness to noise is the conditioning of the matrix \mathbf{Q} . We plot the singular values of \mathbf{Q} (normalized by the maximal value of each curve to compare the condition numbers) in Fig. 3.5. We find that the matrix condition number improves with the number of optical sources used for condition numbers of corresponding cases). With 2 optical sources, Eq. 3.16 is under-determined. For two sources \mathbf{Q} is of size $J \times 2N$ with $J = N =$

20^2 , hence there are only 400 rather than 800 singular values. Matrix conditioning improves by using 4 sources rather than 2, and further improves by using 8. Interestingly, the diffusion coefficient seems to be reconstructed with higher accuracy than the absorption coefficient despite that photoacoustic signals in reality are more sensitive to absorption. This is consistent with the fact that the matrix condition number of \mathbf{Q}^a is larger than that of \mathbf{Q}^s for the case of 8 sources (data not shown). The nature of our inversion strategy might be accounting for this phenomenon. Based on our assumptions, the ratio of photoacoustic signals is simplified into a ratio of fluences, which is sensitive to scattering perturbations. We also plot singular values from the linearized CW-DOT technique [31] when recovering optical properties. Three kinds of configuration were used for the CW-DOT imaging, as is shown in Fig. 3.4. In the first one, the same sources locations as the MI-PAT simulation are used, but only diffuse reflectance of light exiting from four tissue surfaces were measured by detectors for the imaging task. A more realistic configuration is to place all 20 sources and 20 detectors on top of the turbid tissue (also with a 3-mm gap from the tissue edge). Finally, we also consider 80 sources and 80 detectors placed around the object as a case where the DOT simulations are not under-determined (but are still ill-conditioned).

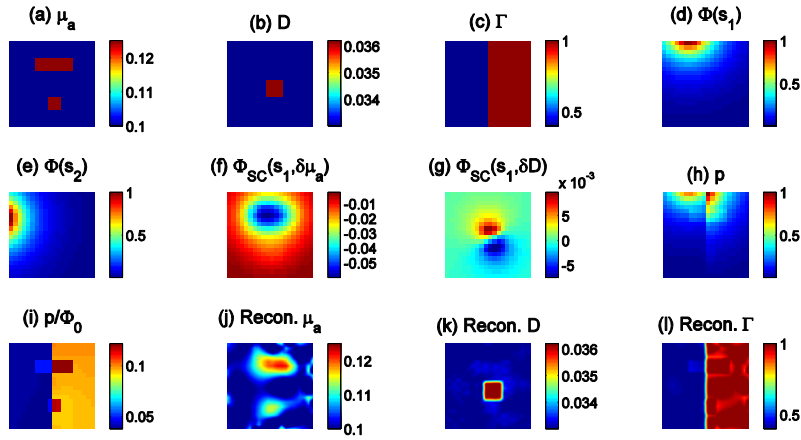


Fig. 3.3 Simulation models and results. (a) True 2D μ_a distribution. (b) True 2D diffusion coefficient distribution. (c) True 2D Grüneisen parameter distribution. (d) Normalized fluence distribution from source s_1 . (e) Normalized fluence distribution from source s_2 . (f) Fluence perturbation from source s_1 due to only absorption perturbation. (g) Fluence perturbation from source s_1 with the presence of only diffusion coefficient perturbation. (h) Photoacoustic imaging with source s_1 . (i) Photoacoustic image normalized by the fluence distribution Φ_0 due to source s_1 , where Φ_0 is calculated under the assumption of a homogeneous medium. If the Grüneisen parameter were constraint, this would represent one approximation to the absorption map. This estimate exhibits unacceptable errors. (j) Reconstructed image of the optical absorption map using our multiple-source photoacoustic inversion technique. (k) Reconstructed image of the diffusion coefficient. (l) Reconstructed image of the Grüneisen parameter.

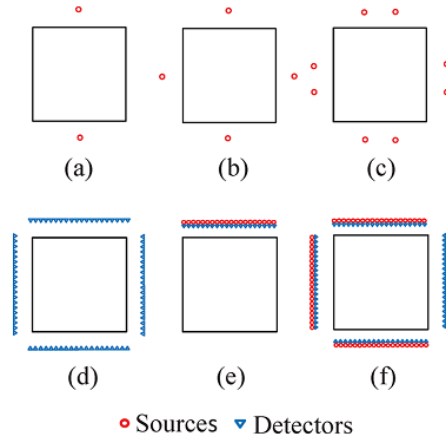


Fig. 3.4 Simulation configuration. (a)-(c) two, four and eight sources located around the object from MI-PAT and DOT imaging simulation. (d) Detector distribution for DOT imaging when using two, four, and eight sources. (e) 20 source-detector pairs positioned on top of the object for DOT. (f) 80 source-detector pairs around the tissue. For all configurations, sources and transducers are positioned 3 mm back from the object surfaces.

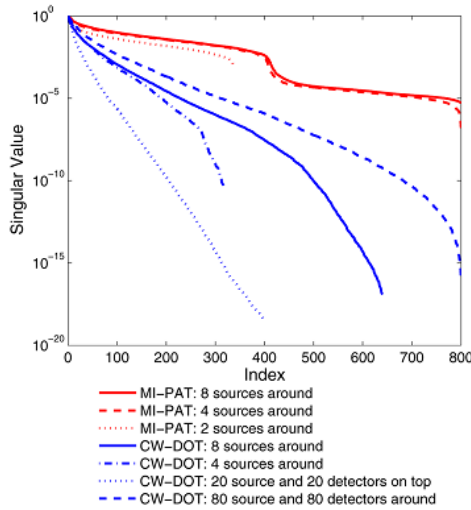


Fig. 3.5 Singular value spectra (normalized by the largest value) of the matrix Q used in the example of Fig. 3.3 for recovering both absorption and scattering perturbations. For $n = 2$ sources, the number of singular values is underdetermined. Matrix conditioning improves when using more sources. The MI-PAT method is better conditioned than DOT imaging.

The condition number of a matrix, defined as the ratio of maximum to minimum singular values, typically determines the numerical stability of inversion. Compared with CW-DOT, while trying to accomplish the same imaging task with the same number of sources, the MI-PAT scheme has orders of magnitude smaller condition number, which implies that it is better-conditioned and thus more informative (please refer to Table 3.1 for the over-determined cases). The positioning of the sources matters too. We found that sources positioned around the object was more informative than cases with sources all on the top of the object. It is interesting to note that our simulations could recover the $\{\mu_a, \mu'_s\}$ distributions accurately with only 3 sources (data not shown), albeit with orders of magnitude worse matrix condition number, hence more sensitivity to noise. Nevertheless, this point is interesting because the work of Bal and Uhlmann [27] predict $2n = 4$ sources are needed for stable reconstruction (where $n = 2$ is the dimension of the space in our simulations). They also point out (mathematically) that fewer than $2n$ illumination patterns are possible at the expense of reconstruction stability. Our findings support their theory.

Table 3.1 Condition Number for Different Configurations

Case	Condition number
MI-PAT, eight sources around	1.9654e5
MI-PAT, four sources around	7.3810e6
CW-DOT, 80 sources and 80 detectors around	1.776e16

3.4 Discussion

We have demonstrated an inversion method to recover both absorption and

scattering perturbations in a known homogeneous turbid background when multiple optical source locations are used. A number of approaches have been discussed in the literature to recover absorption-only perturbations without multiple sources. Recovery of both absorption and scattering perturbations, however, has remained a challenge. In part this is due to the ill-posedness associated with absorption-scattering non-uniqueness. We have demonstrated that the non-uniqueness problem is remedied by the use of multiple optical source illumination locations. The method presented here is not iterative, is not under-determined (although like many methods may be ill-conditioned), and is the first, to our knowledge to address multiple optical sources in a quantitative photoacoustic reconstruction framework. Very little has been done on work to recover optical properties using photoacoustics when the Grüeneisen parameter $\Gamma(\mathbf{r})$ (note $\kappa(\mathbf{r}) \propto \Gamma(\mathbf{r})$) is spatially varying. Surveying the literature, Cox B. et al. [11] note that the Grüeneisen parameter Γ can vary considerably between different tissue types, and as such, may serve as a significant challenge for quantitative photoacoustic inversion of optical properties. Because the present framework can reconstruct optical properties independently of the local Grüeneisen parameter, we believe it worthwhile to explore further. From the ability to estimate tissue optical properties, we can predict local fluence and hence estimate the Grüeneisen parameter distribution, which may have diagnostic value in and of itself, but may also prove important for temperature imaging, due to the temperature-dependence of this parameter.

While our theoretical framework accounts for a spatio-temporal system-response, the present simulations are restricted to an ideal photoacoustic imaging system response. For the theoretical developments to work when a more realistic imaging system is used, the conditions for the approximations discussed must hold well (i.e. the fluence must be slowly varying compared to the size of the point-

spread function, and spatial variations of optical properties must not be too strong), otherwise additional errors will be introduced and reconstructions may fail.

We believe that ill-conditioning arises due to the diffusive nature of light propagation in tissue. Matrix condition number worsens with penetration depth - or equivalently, the dynamic range of fluence values throughout the image (data not shown). Illumination from points around the object rather than just the top surface was shown to be significantly advantageous in this regard. A challenge our framework faces is its sensitivity to data noise. This may be due to our hypothesis behind the derivation of the radiometric quantity in Eq. 3.16. As such we only consider points in the photoacoustic images which have high signal-to-noise (SNR). SNR of photoacoustic images will be important to avoid reconstruction instabilities when matrix condition numbers are large. Even though we use only high SNR locations as virtual detectors, we must have enough source-(virtual) detector pair combinations to produce adequate estimates of the subsurface fluence and absorption distributions if we have an adequate number of optical sources. In the presence of increasing amounts of noise, we found that regularization methods become important. Investigation of various regularization schemes to stabilize the inversion should be a topic of future work.

When the linear assumption made in Section 2 proves restrictive, the inversion scheme could be extended to nonlinear case in a number of ways. Iterations of the present method may be attempted, and should be the subject of future work. This will entail computations of Jacobian matrices $\mathbf{J} = [\frac{\partial\Phi}{\partial\mu_a}, \frac{\partial\Phi}{\partial\mathbf{D}}]$ (eg. using Finite-Element methods) at each iteration, rather than using the analytical Green's function-approximation $\mathbf{J} \approx \mathbf{W}$ for a homogenous turbid background. Then the $k + 1^{th}$ iteration of the optical properties \mathbf{u}^{k+1} would use the previous iteration's estimates as follows: $\mathbf{u}^{k+1} = inv(\mathbf{Q}^k)\mathbf{b}^k$ where \mathbf{Q}^k and \mathbf{b}^k are the k^{th}

estimate of the \mathbf{Q} matrix and \mathbf{b} vector, respectively. However, for large scale 3D reconstruction, the jacobian matrix might be computationally expensive and requires large memory space. To overcome this problem, Gao et al. [32] proposed a gradient-based method for quantitative photoacoustic imaging. Alternatively, techniques for the inversion of a Born series for diffuse waves could be exploited [33]. More generally, nonlinear optimization-based schemes for image reconstruction should be considered, which will additionally permit various constraints to be included as terms modifying an objective function. For example, Gao et al. [34] proposed using the Bregman method combined with the total variation regularization for recovering both absorption and scattering information in turbid media with photoacoustic imaging. Numerical simulation showed that their methods surpass Jacobian-matrix-based methods in terms of computational efficacy. Furthermore, piecewise features can be better reserved with the proposed regularization scheme. Nevertheless, The present linearized inversion problem could serve as a starting point for such iterative procedures. Three-dimensional reconstructions should be tested numerically, then, future work should of course involve experiments to test the practicality of our methods.

Combining multiple optical source locations with multiwavelength photoacoustic imaging may provide quantitative estimates of chromophore concentrations which in turn may pave the way for reliable mapping of oxygen saturation of hemoglobin and quantitative molecular imaging applications. Additionally, similar to Cox et al. [9], prior knowledge of the wavelength-dependence of the scattering coefficient may further alleviate ill-conditioning and absorption-scattering non-uniqueness. This list of future projects can now proceed given the present groundwork.

3.5 Conclusions

We have presented, for the first time, a theoretical framework and numerical results for quantitative estimation of optical properties with multiple-source photoacoustic optical tomography. The reconstruction algorithm presented is able to reproduce optical absorption, scattering, and Grüeneisen distributions in a known turbid-media background with high accuracy. Compared with CW-DOT, our methods are better-conditioned. We also show the reconstruction of spatially varying Grüeneisen parameter for the first time. Despite some challenges our methods faces in terms of robustness to noise, this article may be a first step towards a number of techniques for quantitative reconstruction of optical properties with high spatial resolution.

3.6 Appendix A: Models of Light Transport

For monochromatic light, the diffusion-equation of optical transport can be written as [31]

$$\frac{\partial \Phi(\mathbf{r}, t)}{\partial t} + c\mu_a(\mathbf{r}, t) - c\nabla \cdot [D\nabla \Phi(\mathbf{r}, t)] = q(\mathbf{r}, t) \quad (3.A1)$$

where q denotes the photon density source strength, c is the speed of light in the medium, and D is the diffusion coefficient. For photoacoustic imaging, we often use lasers with multiple-nanosecond pulse-lengths. Over a time-scale of a few nanoseconds light can propagate distances of meters, whereas we are concerned with cm-distance scales for biological imaging applications, hence, we can effectively consider q to be time-independent for our present purposes.

If we assume that all light propagation, scattering and absorption will finish in a time scale much shorter than the acoustic time scale, the optical part of the propagation is independent of time. For a time-independent point-source $q(\mathbf{r}, t) =$

$A\delta(\mathbf{r})$ in an effectively infinite turbid homogeneous medium, we have

$$\mu_{\text{eff}}^2 \Phi_0(\mathbf{r}) - \nabla^2 \Phi_0(\mathbf{r}) = \frac{A}{cD} \delta(\mathbf{r}) \quad (3.A2)$$

where $\mu_{\text{eff}} = \sqrt{\mu_a/D}$. Taking the spatial Fourier transform, this equation can be written as

$$[k^2 + \mu_{\text{eff}}^2] \Phi_0(\mathbf{k}) = \frac{A}{cD} \quad (3.A3)$$

where k is the magnitude of \mathbf{k} , the spatial frequency vector conjugate to \mathbf{r} . The solution in three-dimensional (3D) space is given by taking the inverse Fourier transform of $\Phi_0(\mathbf{k})$ as

$$\Phi_0(\mathbf{r}) = A \frac{\exp(-\mu_{\text{eff}} r)}{4\pi c D r} \quad (3.A4)$$

where $r = |\mathbf{r}|$. For two-dimensional space (2D) the solution is found as the inverse Hankel transform of $\Phi_0(\mathbf{k})$, which is

$$\Phi_0(\mathbf{r}) = \frac{A}{2\pi c D} K_0(\mu_{\text{eff}} r) \quad (3.A5)$$

where K_0 is the modified Bessel function of the second kind of order zero. The 2D solution will prove useful for proof-of-principle numerical studies. The corresponding Green's functions solution to for $\mu_{\text{eff}}^2 G_0(\mathbf{r}, \mathbf{r}') - \nabla^2 G_0(\mathbf{r}, \mathbf{r}') = \delta(\mathbf{r})$ for 3D and 2D are

$$G_0(\mathbf{r}, \mathbf{r}') = \frac{\exp(-\mu_{\text{eff}}|\mathbf{r} - \mathbf{r}'|)}{4\pi|\mathbf{r} - \mathbf{r}'|} \quad (3.A6)$$

and

$$G_0(\mathbf{r}, \mathbf{r}') = \frac{K_0(-\mu_{\text{eff}}|\mathbf{r} - \mathbf{r}'|)}{2\pi}, \quad (3.A7)$$

respectively.

Our modeling requires computation of the gradients of both $G_0(\mathbf{r}, \mathbf{r}')$ and Φ . Because of radial symmetry about the source

$$\nabla G_0(\mathbf{r}_j, \mathbf{r}') = \hat{\mathbf{r}} \frac{\partial G_0(\mathbf{r}_j, \mathbf{r}')}{\partial r} \quad (3.A8)$$

For the 2D models the Green's function is given by Eq. 3. A7, and using properties of Bessel functions,

$$\frac{\partial K_0(\mu_{\text{eff}}r)}{\partial r} = -\mu_{\text{eff}}K_1(\mu_{\text{eff}}r) \quad (3.A9)$$

Hence, for 2D, Eq. 3.9 becomes

$$\begin{aligned} W_{\{ij\}n}^s &= -\frac{A\mu_{\text{eff}}^2}{4\pi^2 cD_0} K_1(\mu_{\text{eff}}|\mathbf{r}_j - \mathbf{r}'_n|) \\ &\times K_1(\mu_{\text{eff}}|\mathbf{r}'_n - \mathbf{r}_{s_i}|) \frac{(\mathbf{r}_j - \mathbf{r}'_n) \cdot (\mathbf{r}'_n - \mathbf{r}_{s_i})\Delta V}{|\mathbf{r}_j - \mathbf{r}'_n||\mathbf{r}'_n - \mathbf{r}_{s_i}|D_0} \end{aligned} \quad (3.A7)$$

Bibliography

- [1] M. Xu and L. V. Wang, "Photoacoustic imaging in biomedicine," *Rev. Sci. Instrum.*, vol. 77, no. 4, p. 041101, 2006.
- [2] B. T. Cox, S. R. Arridge, K. P. Köstli, and P. C. Beard, "two-dimensional quantitative photoacoustic image reconstruction of absorption distribution in scattering media by use of a simple iterative method," pp. 4–6, 2006.
- [3] Z. Yuan and H. Jiang, "Quantitative photoacoustic tomography: Recovery of optical absorption coefficient maps of heterogeneous media," *Appl. Phys. Lett.*, vol. 88, no. 23, p. 231101, 2006.
- [4] J. Ripoll and V. Ntziachristos, "Quantitative point source photoacoustic inversion formulas for scattering and absorbing media," *Phys. Rev. E*, vol. 71, no. 3, p. 031912, Mar. 2005.
- [5] T. Jetzfellner, D. Razansky, A. Rosenthal, R. Schulz, K.-H. Englmeier, and V. Ntziachristos, "Performance of iterative optoacoustic tomography with experimental data," *Appl. Phys. Lett.*, vol. 95, no. 1, p. 013703, 2009.
- [6] B. Banerjee, S. Bagchi, R. M. Vasu, and D. Roy, "Quantitative photoacoustic tomography from boundary pressure measurements: noniterative recovery of optical absorption coefficient from the reconstructed absorbed energy map.," *J. Opt. Soc. Am. A. Opt. Image Sci. Vis.*, vol. 25, no. 9, pp. 2347–56, Sep. 2008.
- [7] L. Yin, Q. Wang, Q. Zhang, and H. Jiang, "Tomographic imaging of absolute optical absorption coefficient in turbid media using combined

- photoacoustic and diffusing light measurements,” *Opt. Lett.*, vol. 32, no. 17, p. 2556, 2007.
- [8] Z. Yuan, Q. Wang, and H. Jiang, “Reconstruction of optical absorption coefficient maps of heterogeneous media by photoacoustic tomography coupled with diffusion equation based regularized Newton method.,” *Opt. Express*, vol. 15, no. 26, pp. 18076–81, Dec. 2007.
- [9] B. T. Cox, S. R. Arridge, and P. C. Beard, “Estimating chromophore distributions from multiwavelength photoacoustic images.,” *J. Opt. Soc. Am. A. Opt. Image Sci. Vis.*, vol. 26, no. 2, pp. 443–55, Feb. 2009.
- [10] Z. Guo, S. Hu, and L. V Wang, “Calibration-free absolute quantification of optical absorption coefficients using acoustic spectra in 3D photoacoustic microscopy of biological tissue.,” *Opt. Lett.*, vol. 35, no. 12, pp. 2067–9, Jun. 2010.
- [11] B. T. Cox, J. G. Laufer, and P. C. Beard, “<title>The challenges for quantitative photoacoustic imaging</title>,” vol. 7177, pp. 717713–717713–9, Feb. 2009.
- [12] I. V Larina, K. V Larin, and R. O. Esenaliev, “Real-time optoacoustic monitoring of temperature in tissues,” *J. Phys. D. Appl. Phys.*, vol. 38, no. 15, pp. 2633–2639, Aug. 2005.
- [13] M. Pramanik, T. N. Erpelding, L. Jankovic, and L. V. Wang, “Tissue temperature monitoring using thermoacoustic and photoacoustic techniques,” in *proceedings of SPIE*, 2010, vol. 7564, p. 75641Y–75641Y–10.

- [14] S. Park, S. R. Aglyamov, W. G. Scott, S. Y. Emelianov, S. Sethuraman, J. M. Rubin, J. Shah, a. B. Karpiouk, S. Mallidi, and R. W. Smalling, “Synergy and Applications of Combined Ultrasound, Elasticity, and Photoacoustic Imaging (Invited),” in *2006 IEEE Ultrasonics Symposium*, 2006, pp. 405–415.
- [15] S. R. Aglyamov, S. Y. Emelianov, J. Shah, K. Sokolov, and T. E. Milner, “4J-2 Ultrasound-Based Thermal and Elasticity Imaging to Assist Photothermal Cancer Therapy - Preliminary Study,” in *Ultrasonics Symposium, 2006. IEEE*, 2006, pp. 1029–1032.
- [16] S. Sethuraman, S. R. Aglyamov, R. W. Smalling, and S. Y. Emelianov, “Remote temperature estimation in intravascular photoacoustic imaging,” *Ultrasound Med. Biol.*, vol. 34, no. 2, pp. 299–308, Mar. 2008.
- [17] S. Park, T. Larson, K. Sokolov, and K. Johnston, “Photoacoustic imaging and temperature measurement for photothermal cancer therapy,” *J. Biomed. Opt.*, vol. 13, no. 3, pp. 1–19, 2009.
- [18] S.-H. Wang, C.-W. Wei, S.-H. Jee, and P.-C. Li, “Photoacoustic temperature measurements for monitoring of thermal therapy,” in *proceedings of SPIE*, 2009, vol. 7177, p. 71771S–71771S–11.
- [19] M. Pramanik and L. V Wang, “Thermoacoustic and photoacoustic sensing of temperature,” *J. Biomed. Opt.*, vol. 14, no. 5, p. 054024, 2009.
- [20] R. Seip and E. S. Ebbini, “Noninvasive estimation of tissue temperature response to heating fields using diagnostic ultrasound,” *IEEE Trans. Biomed. Eng.*, vol. 42, no. 8, pp. 828–39, Aug. 1995.

- [21] R. Maass-Moreno and C. A. Damianou, "Noninvasive temperature estimation in tissue via ultrasound echo-shifts. Part I. Analytical model," *J. Acoust. Soc. Am.*, vol. 100, pp. 2514–2521, 1996.
- [22] R. Seip and P. VanBaren, "Noninvasive real-time multipoint temperature control for ultrasound phased array treatments," ... *Freq. Control. ...*, vol. 43, no. 6, pp. 1063–1073, 1996.
- [23] S. J. Graham, M. J. Bronskill, and R. M. Henkelman, "Time and temperature dependence of MR parameters during thermal coagulation of ex vivo rabbit muscle.," *Magn. Reson. Med.*, vol. 39, no. 2, pp. 198–203, Mar. 1998.
- [24] P. Steiner, R. Botnar, B. Dubno, G. G. Zimmermann, G. S. Gazelle, and D. J. F., "Radio-frequency-induced thermoablation: monitoring with T1-weighted and proton-frequency-shift MR imaging in an interventional 0.5-T environment," *Radiology*, vol. 206, no. 3, pp. 803–810, 1998.
- [25] R. J. Zemp, J. Ranasinghesagara, Y. Jiang, X. Chen, and M. Kory, "A photoacoustic method for optical scattering measurements in turbid media," in *proceedings of SPIE*, 2009, p. 71770Q.
- [26] J. C. Ranasinghesagara, Y. Jiang, X. Chen, M. Kory, and R. J. Zemp, "Photoacoustic technique for assessing optical scattering properties of turbid media," *J. Biomed. Opt.*, vol. 14, no. 4, p. 040504, 2009.
- [27] G. Bal and G. Uhlmann, "Inverse diffusion theory of photoacoustics," *Inverse Probl.*, vol. 26, no. 8, p. 085010, Aug. 2010.

- [28] R. J. Zemp, “Quantitative photoacoustic tomography with multiple optical sources,” *Appl. Opt.*, vol. 49, no. 18, pp. 3566–72, Jun. 2010.
- [29] S. R. Arridge, W. R. B. Lionheart, S. R. Arridge, and W. R. B. Lionheart, “Nonuniqueness in diffusion-based optical tomography,” *Opt. Lett.*, vol. 23, no. 11, pp. 882–884, 1998.
- [30] S. R. Arridge, M. Schweiger, M. Hiraoka, and D. D. T., “a finite element approach for modeling photon transport in tissue,” *Medical Phys.*, vol. 20, no. 2, pp. 299–309, 1993.
- [31] L. V. Wang and H. Wu, *Biomedical Optics, principles and imaging*. Willey-Interscience, 2007.
- [32] H. Gao, H. Zhao, and S. Osher, “Quantitative photoacoustic tomography,” 2011.
- [33] S. Moskow and S. J. C., “Numerical studies of the inverse Born series for diffuse waves,” *Inverse Probl.*, vol. 25, no. 9, p. 095007, 2009.
- [34] H. Gao, H. Zhao, and S. Osher, “Bregman methods in quantitative photoacoustic tomography,” 2010.

4. Iterative Algorithm for Multiple-illumination Photoacoustic Tomography (MI-PAT) Using Ultrasound Channel Data¹

4.1 Introduction

Photoacoustic tomography (PAT) holds significant promise for high-resolution optical tomographic imaging in optically-scattering tissues. Often, two steps are involved in PAT reconstruction problems. First, the absorbed energy (or initial pressure) distribution is estimated from the measured acoustic signals. Second, one seeks to reconstruct optical properties, the optical absorption coefficient and scattering coefficient map, as well as the Grüneisen parameter distribution based on the results of the first step. This is often called quantitative PAT, or quantitation of PAT. The first step is a well-known acoustic inverse problem and thoroughly studied [1] [2] [3]. The second step, an optical inverse problem is, however, non-trivial [4]. This is because of several reasons. The local initial pressures generated when absorbed light pulses are converted to acoustic signals are proportional to not only the local optical absorption coefficient, but also the local laser fluence, which is in turn a complex nonlinear function of the distributed optical properties of the medium. This nonlinear inverse problem of estimating optical properties from photoacoustic data is further complicated by potential ill-posedness: a given photoacoustic absorbed energy distribution may be due to non-unique absorption-

¹ A version of this chapter has been published. Reprint with permissions from: P. Shao, T. J. Harrison and R. J. Zemp, *Biomed. Opt. Express*, 3(12), p. 3240-3249, 2012. Copyright 2012 OSA.

scattering distribution pairs. Additionally, when the Grüneisen parameter is unknown as a function of space, Bal and Ren argue that based on diffusion theory, with a single wavelength, only two of the three coefficients in quantitative PAT can be reconstructed uniquely [5].

Quite a number of methods were proposed for quantitative PAT. Studies were conducted in recovering absorption coefficient distributions with scattering background as a priori information [6] [7] [8] [9]. Yin et al. [10] iteratively estimated absorbed energy density with PAT and fluence distribution with diffuse optical tomography. Jetzfellner et al. [11] studied the experimental performance of an iterative scheme and concluded that scattering coefficient errors may lead to failure of the method. Cox et al. [12] recovered both absorption and scattering distribution with multiple optical wavelengths when known wavelength dependence of the optical scattering exists. Efforts were also made later on to decouple Grüneisen coefficients in quantitative PAT. Bal and Ren [13] proposed a scheme for reconstructing absorption, diffusion and Grüneisen coefficients distributions simultaneously with measured data by different wavelengths and a priori information on the form of the coefficients stably.

Recently we demonstrated a linearized non-iterative algorithm, namely multiple-illumination photoacoustic tomography (MIPAT), for recovering absorption-scattering distributions using multiple illuminations [14] [15]. This approach showed that multiple sources can significantly mitigate absorption-scattering non-uniqueness as demonstrated by simulations. The algorithm we reported used a diffusion-regime ratiometric approach and assumed that initial pressures could be reconstructed in an ideal way. Unfortunately, artifacts in the reconstructed initial pressure distribution can lead to undesirable errors when solving for optical properties. Despite these limitations, the technique showed

promise for multiple illumination photoacoustic data for more complex problems.

In this paper, we propose an updated version of the MIPAT algorithm that does not require an ideal initial pressure reconstruction, and that instead uses channel data from an ultrasound transducer array as the measurements. The proposed algorithm employs an iterative scheme, therefore it is capable of recovering relatively stronger heterogeneities. While we presently restrict ourselves to the diffusion-regime in 2D, the approach can potentially be generalized to include radiative transport models in 2 or 3 dimensions.

4.2 Theory

4.2.1 Light Propagation Model

We use the diffusion equation of optical transport as the light propagation model, which can be written as [16]

$$\frac{\partial \Phi(\mathbf{r}, t)}{\partial t} + c\mu_a \Phi(\mathbf{r}, t) - c\nabla \cdot [D\nabla \Phi(\mathbf{r}, t)] = q(\mathbf{r}, t), \quad (4.1)$$

in which q is the photon density source strength, c is light speed in the medium. D is the diffusion coefficient, which is defined as a function optical properties as $1/3(\mu_a + \mu_s')$. Here μ_a and μ_s' are the optical absorption coefficient and reduced scattering coefficient, respectively. A time-independent form of this equation is often sufficient when laser-pulse widths are significantly longer than the average random-walk time of photons through the tissue, in which case the time-derivative is neglected. To ensure that the diffusion model is valid, we require $\mu_s' \gg \mu_a$. With this hypothesis, fluence Φ will be almost isotropic. To calculate the fluence perturbations due to background heterogeneity at location \mathbf{r} , we use the relations

[16],

$$\Phi(\mathbf{r}) = \Phi_0(\mathbf{r}) + \Phi_{sc}(\mathbf{r}) \quad (4.2)$$

$$\begin{aligned} \Phi_{sc}(\mathbf{r}) = & -\int \frac{\delta\mu_a(\mathbf{r}')}{D_0} G_0(\mathbf{r}, \mathbf{r}') \Phi(\mathbf{r}') \\ & + \int \frac{\delta D(\mathbf{r}')}{D_0} \nabla G_0(\mathbf{r}, \mathbf{r}') \cdot \nabla \Phi(\mathbf{r}') d\mathbf{r}' \end{aligned} \quad (4.3)$$

$G_0(\mathbf{r}, \mathbf{r}')$ is the Green's function representing propagation from $\mathbf{r} \rightarrow \mathbf{r}'$. D_0 is the diffusion coefficient of the background. Optical property distributions are written as $\mu_a(\mathbf{r}) = \mu_a + \delta\mu_a$ and $D(\mathbf{r}) = D_0 + \delta D(\mathbf{r})$. The Born approximation is used in this paper to estimate fluence perturbations due to optical property variations at location \mathbf{r} , when assuming that the fluence perturbations are small: $\Phi_{sc}(\mathbf{r}) \ll \Phi_0(\mathbf{r})$, where $\Phi_0(\mathbf{r})$ is the background optical fluence.

4.2.2 Reconstruction of the Optical Properties with Ultrasound Channel Data

Consider that we have a photoacoustic tomography system with M ultrasound transducers and S illumination patterns. Consider that each detector acquires T time points at a given sampling frequency. A column vector of observed pressure measurements may be constructed as

$$\mathbf{p}^0 = \begin{bmatrix} p_{\{111\}}^0 & \cdots & p_{\{T11\}}^0 & \cdots & p_{\{1M1\}}^0 & \cdots & p_{\{TM1\}}^0 & \cdots \\ p_{\{11S\}}^0 & \cdots & p_{\{T1S\}}^0 & \cdots & p_{\{1MS\}}^0 & \cdots & p_{\{TMS\}}^0 & \cdots \end{bmatrix}^t \quad (4.4)$$

where $p_{\{\tau ik\}}^0$ is the observed pressure at time-point τ , with detector i , due to source k . The composite index $\{\tau ik\}$ can also be assigned the index ρ to map uniquely to the ρ th element of this vector such that $\rho = \tau + (i-1)T + (k-1)MT$.

We want to compare these observed photoacoustic channel measurements with forward-model computed values \mathbf{p}^c which are a function of the optical parameters $\mathbf{u} = [\boldsymbol{\mu}_a \quad \mathbf{D}]^T$, where $\boldsymbol{\mu}_a$ and \mathbf{D} are rasterized column vectors of the optical absorption and diffusion coefficient maps. The objective is to find best estimate $\hat{\mathbf{u}}$ for \mathbf{u} such that

$$\hat{\mathbf{u}} = \arg \min_{\mathbf{u}} \varepsilon(\mathbf{u}), \quad (4.5)$$

where $\varepsilon(\mathbf{u}) = \|\mathbf{p}^o - \mathbf{p}^c\|^2 + \lambda\beta(\mathbf{u})$ is the regularized least-squares error functional with regularizing penalty function $\beta(\mathbf{u})$, which can be taken as a total variation functional or other related functional. λ is the so-called trade-off parameter that determines how much emphasis is placed on regularization while seeking the optimal solution. Forward model calculations of pressures received by transducer i due to source illumination k follow from the superposition of propagated initial pressure signals:

$$p_{\{i,k\}}^c = \int \frac{p_{o,k}(\mathbf{r}_i, t_\tau - R_i/c)}{4\pi R_i} d\mathbf{r} = f^k(\mathbf{r}_i, \mathbf{u}, t_\tau), \quad (4.6)$$

with $R_i = |\mathbf{r}_i - \mathbf{r}|$ where \mathbf{r}_i is the location of the detector and \mathbf{r} is a field point. This expression is valid for point-detectors with isotropic directivity and ideal electromechanical efficiency. Initial pressures are computed simply as $p_{o,k}(\mathbf{r}, t) = \Gamma\mu_a(\mathbf{r})\Phi_k(\mathbf{r}, \mathbf{u})\delta(t)$ where Γ is the Grüneisen parameter, assumed to be a constant in this paper, and Φ_k is the local laser fluence due to source k . To

model the electromechanical response of the transducer, $f^k(\mathbf{r}_i, \mathbf{u}, t_\tau)$ is convolved with impulse response $h_{r,x}(t)$. Thus in the expression for $p_{\{rik\}}^c$ we can use a filtered version of the initial pressure distribution written as $p_{o,k}(\mathbf{r}, t) = \Gamma \mu_a(\mathbf{r}) \Phi_k(\mathbf{r}, \mathbf{u}) h_{r,x}(t)$. In future work, the computed channel data may also be modified to include finite aperture effects and acoustic attenuation. By considering that $f^k(\mathbf{r}_i, \mathbf{u} + \delta\mathbf{u}, t_\tau) \cong f^k(\mathbf{r}_i, \mathbf{u}, t_\tau) + \mathbf{J}_i^k \delta\mathbf{u}$, and requiring that $\partial \varepsilon(\mathbf{u}) / \partial \delta\mathbf{u} = 0$ we arrive at the iterative algorithm $(\mathbf{J}^T \mathbf{J}) \delta\mathbf{u} = \mathbf{J}^T (\mathbf{p}^o - \mathbf{p}^c(\mathbf{u}))$, which can be written as

$$\mathbf{J}^T \mathbf{J} \delta\mathbf{u} = \mathbf{J}^T \Delta, \quad (4.7)$$

with $\Delta \equiv \mathbf{p}^o - \mathbf{p}^c(\mathbf{u})$. For each iteration of the algorithm, $\delta\mathbf{u}$ is computed as an update vector. Once the optical properties are updated, new \mathbf{p}^c vectors and Jacobian matrices \mathbf{J} are computed, then a new update vector $\delta\mathbf{u}$ is computed, and the iterations continue until successive iterations of the algorithm yield little change. With Hessian matrix approximated as $\mathbf{H} = \mathbf{J}^T \mathbf{J}$, a Gauss-Newton step may be added to improve convergence speed such that $\delta\mathbf{u} = \alpha \mathbf{H}^{-1} [\mathbf{J}^T \Delta]$ and where α is a scalar chosen via a line-search algorithm to further minimize the error functional for each step. The Jacobian matrix has elements

$$\mathbf{J}_{\rho j} = \mathbf{J}_{\{rik\}j} = \frac{\partial f^k(\mathbf{r}_i, \mathbf{u}, t_\tau)}{\partial \mathbf{u}_j} = \sum_{\ell} \left(\frac{\partial f^k(\mathbf{r}_i, \mathbf{u}, t_\tau)}{\partial E_{\ell}^k} \right) \left(\frac{\partial E_{\ell}^k}{\partial \mathbf{u}_j} \right), \quad (4.8)$$

where $E_\ell^k = \langle \epsilon_\ell \rangle_{\tau \sim \tau_\ell}$ is the time-independent absorbed energy at location \mathbf{r}_ℓ due to source k. It is straightforward to show that

$$\left[\mathbf{a}^{\{tik\}} \right]_\ell = \frac{\partial f^k(\mathbf{r}_i, \mathbf{u}, t_\tau)}{\partial E_\ell^k} = \Gamma \frac{h_{rx}(t_\tau - R_{i\ell} / c)}{1 - \mathbf{n}_\ell^T \mathbf{n}_\ell}, \quad (4.9)$$

which reduces to the Gruneisen parameter times the free-space acoustic Green's function when $h_{rx}(t) \rightarrow \delta(t)$ and represents acoustic propagation from field point ℓ to detector i. $\partial E_\ell^k / \partial \mu_j$ represents optical absorbed energy variation with respect to optical property perturbations and it can be written as:

$$\left[\mathbf{B}^k \right]_{j\ell} = \frac{\partial E_\ell^k}{\partial \mu_j} \begin{bmatrix} \gamma_{\ell}^k & \gamma_{\ell}^k \\ \partial \mu_{aj} & \partial D_j \end{bmatrix}^T. \quad (4.10)$$

Given that the diffusion coefficient may be written as $D = 1/3(\mu_a + \mu_s)$, we have

$$\frac{\partial E_\ell^k}{\partial \mu_{aj}} = \langle \epsilon_\ell \rangle_{\tau \sim \tau_\ell} \frac{\partial \Phi_k(\mathbf{r}_\ell)}{\partial \mu_{aj}} \quad (4.11-a)$$

$$\frac{\partial E_\ell^k}{\partial D_j} = \langle \epsilon_\ell \rangle_{\tau \sim \tau_\ell} \frac{\partial \Phi_k(\mathbf{r}_\ell)}{\partial D_j} \quad (4.11-b)$$

The partial derivatives can in turn be computed from the diffusion equation or in linearized form as

$$\frac{\partial \Phi_k(\mathbf{r}_\ell)}{\partial \mu_{aj}} = \frac{\Delta x \Delta y}{D_0} G_0(\mathbf{r}_\ell) \quad (4.12-a)$$

$$\frac{\partial \Phi_k(\mathbf{r}_\ell)}{\partial D_j} = x \Delta y G_0(\mathbf{r}_\ell) \quad (4.12-b)$$

Observed and computed pressure vectors have dimensions $TMS \times 1$. For an $N \times N$ 2D grid of optical properties, \mathbf{u} and $\delta \mathbf{u}$ have dimensions $2N^2 \times 1$. Jacobian matrices have dimensions $TMS \times 2N^2$. These matrices can be quite large. The Hessian H of size $2N^2 \times 2N^2$ has quadrant symmetry, reducing memory requirements. With the above notation, the ρ th row of \mathbf{J} is a $1 \times 2N^2$ vector given as $\mathbf{J}_\rho = \mathbf{J}_{\{\tau ik\}} = [\mathbf{B}^k \boldsymbol{\alpha}^{\{\tau ik\}}]^T$ where for a given k , \mathbf{B}^k is a $2N^2 \times 2N^2$ matrix and for a given $\{\tau ik\}$, $\boldsymbol{\alpha}^{\{\tau ik\}}$ is an $2N^2 \times 1$ column vector. The Jacobian need not to be stored, but calculated row by row to find $\mathbf{b} = \mathbf{J}^T \Delta = \sum_{\rho=1}^{TMS} \mathbf{J}_\rho^T \mathbf{J}_\rho$ and $\mathbf{H} = \sum_{\rho=1}^{TMS} \mathbf{J}_\rho^T \mathbf{J}_\rho$ in a loop over ρ (a loop over the indices $\{\tau ik\}$). Future Gradient-based optimization methods may circumvent the necessity of using such large matrices.

4.2.3 Inversion

Rewrite equation (4.7) as

$$\mathbf{H} \delta \mathbf{u} = \mathbf{b}, \quad (4.13)$$

where $\mathbf{b} = \mathbf{J}^T \Delta$. Now estimating the unknown parameters $\delta \mathbf{u}$ is an inverse problem. Different techniques can be employed to solve the problem. For the i^{th} iteration, we minimize the following cost function

$$\mathbf{J}_i(\delta \mathbf{u}_i) = \|\mathbf{H} \delta \mathbf{u}_{i-1} - \mathbf{b}_{i-1}\|_2^2 + \lambda \|\mathbf{W} \delta \mathbf{u}_{i-1}\|_2^2. \quad (4.14)$$

For any vector \mathbf{x} , $\|\mathbf{x}\|_2^2$ is the ℓ_2 -norm. The first term is the least squares norm which represents the misfit portion of the cost function. The second term is the Tikhonov regularization term and represents the constraints possessed on the parameter to be estimated. \mathbf{W} is a 2-dimensional regularization operator matrix or weighting matrix. Here we use the second order derivatives as a smoothing weighting factor. For each iteration, the least-squares minimum solution is found with $\nabla \mathbf{J}_i = 0$, which yields $\delta \hat{\mathbf{u}}_i = (\mathbf{H}_{i-1}^T \mathbf{H}_{i-1} + \lambda \mathbf{W}^T \mathbf{W})^{-1} \mathbf{H}_{i-1}^T \mathbf{b}$. Solution $\delta \hat{\mathbf{u}}_i$ is then used to update optical fluence estimation for next iteration. Initial guess of the parameters to be estimated is chosen to be the background absorption and scattering distribution.

4.3 Numerical Simulation

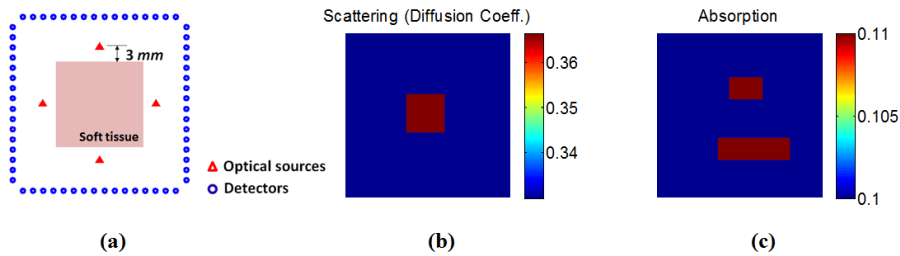


Fig. 4.1 Simulation model setup. The 2-dimensional simulation configuration is shown in (a) and true optical property model are presented in (b) and (c). Four light sources are distributed on each side of the imaging object, with a 3-mm gap backward from the soft tissue surface. 64 detectors are circumferentially located around the object.

With the framework above, we simulated multiple-illuminations of 2D absorption

and scattering distributions $2 \text{ cm} \times 2 \text{ cm}$ in a grid of 30×30 pixels of size $\Delta x = \Delta y = 667 \mu\text{m}$. Configuration of the simulation numerical model is shown in Fig. 4.1. The reduced scattering coefficient of the turbid background is taken as 10 cm^{-1} everywhere except a scattering perturbation of 1 cm^{-1} . The background scattering coefficient is taken as $\mu_s = 0.1 \text{ cm}^{-1}$, while one region is taken to have a 10% scattering perturbation. We use 4 illumination sources and an array of 64 ultrasound point detectors distributed circumferentially 1cm away from the object (16 on each side of the object). The optical sources are placed 3 mm away from the object to validate the light transport model in the diffusion regime. The gap permits isotropic source in an infinite medium to be a reasonable approximation to the pencil-beam illumination in experimental scenarios. We sample pressure signals generated by photoacoustic effects with a temporal sampling frequency of 15 MHz. The transducer electromechanical response $h_{rx}(t)$ is modeled as a low-pass Hanning filter of width 7 time samples. 1% normally distributed white noise (zero mean and 1% of the mean of data) is added to measurements. Fig. 4.2 shows some ‘measured data’ we generated with the simulation model. (a) is the normalized optical fluence generated with a point source on top of the grid system. (b) and (c) are the fluence perturbations due to only absorption and scattering with one point optical source on top of the grid system, respectively. (d) is the total fluence perturbation and (e) is the ultrasound transducer channel data.

The time vector has maximum length 283 samples, so with 4 sources the Jacobian is of size 72448×1800 , the pressure vectors are of length 1800, and the Hessian matrix is 1800×1800 .

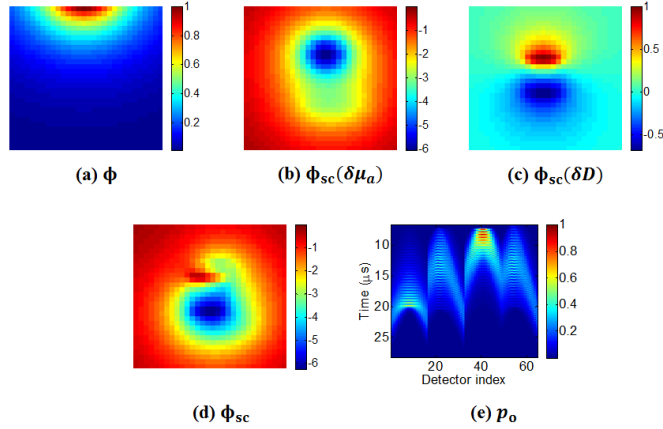


Fig. 4.2 Some quantities generated in the simulation study. (a) Normalized optical fluence distribution from source on top of the object. (b) Optical fluence perturbations due to only absorption heterogeneities. (c) Fluence perturbations due to only diffusion coefficient distribution. (d) Total fluence perturbations. (e) Ultrasound transducer channel data due to the same light source.

Reconstructed optical absorption and scattering distribution is shown in Fig. 4.3. Both μ_a and D distributions are faithfully recovered. μ_a is better recovered than scattering features. This supports conclusions by other researchers [17]. We believe this is due to stronger dependence of photoacoustic signals on optical absorption. This is also confirmed with faster convergence of optical absorption, as is shown in Fig. 4.5. A single iteration provides a reasonable first estimate of both μ_a and D . Additional iterations improve absorption distribution estimates in particular, however, diffusion coefficient begin diverging and this becomes appreciable especially after 10 iterations. By experimental work, the authors Jetzfellner et al. [11] found that a fixed point iteration scheme for recovering absorption heterogeneities could lead to divergence with over-iteration. Their work involved a single illumination pattern. They suggested that *a priori* information on the imaged object may be necessary. Our simulation showcased improved convergence in absorption distributions albeit with simulated data. As a comparison, we also show results with the ratiometric method described previously in [15] in the bottom row.

Only data with signal-to-noise ratio above 60 dB were used in this case. As is shown, the error in the reconstructed absorption map is unacceptably high for the radiometric approach. Reconstruction of absorption failed. This is because the diffusion coefficient D has higher values than that in the previous paper and cross-talk between absorption and scattering begin to appear. Where the proposed method can alleviate the cross-talk, the ratio-metric method cannot. Scattering features are recovered better than absorption. While this does not agree with real cases, it is due to the nature of the algorithm. Readers can refer to [15] for discussion.

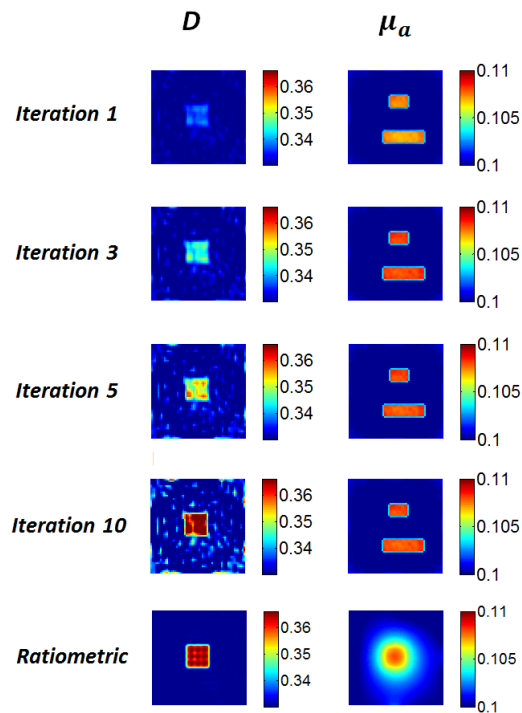


Fig. 4.3 Simulation results the proposed method and the ratio metric method with 4 illuminations surrounding the object. From top to bottom, absorption and diffusion on coefficient distribution obtained with the radiometric method described in [15], and the 1st, 3rd, 5th, and 10th iteration with the proposed method.

The singular values of the Hessian are analyzed as an indicator of inversion stability. The first-iteration Hessian with 1, 4 and 8 sources are shown in Fig. 4.5.

We found that conditioning improves with multiple illumination sources compared to one source alone (condition numbers are shown in Table 4.1). Detector count and positioning is also advantageous for inversion stability. 64 detectors yield better conditioning than circumferentially positioned 16 detectors. We also found that equally distributed sources perform better than densely positioned sources on one side of the object (data not shown). Conditioning of the inversion of each iteration is similar. Multi-source configuration is commonly used on diffuse optical tomography, therefore we also compared the conditioning of our proposed methods with continuous wave diffuse optical tomography (CW-DOT). With the same number of optical sources and detectors, the proposed method is orders of magnitude less ill-conditioned.

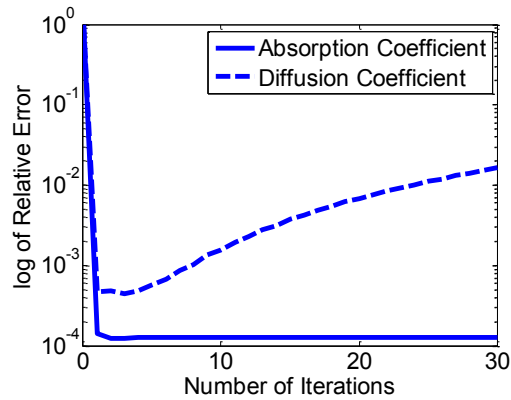


Fig. 4.4 Normalized reconstruction errors with 10 iterations.

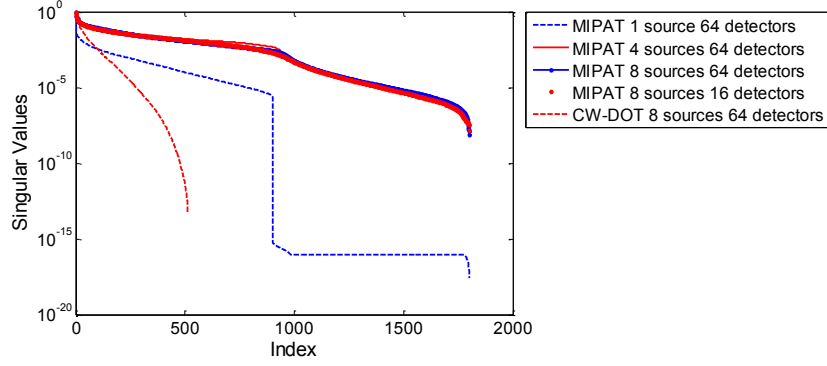


Fig. 4.5 Singular values of the Jacobian matrices for different configurations. MIPAT with different source and detector count (1, 4 and 8 sources with 64 detectors and 16 detectors) are compared. Conditioning of CW-DOT with the same number of sources and detectors is also included for comparison.

Table 4.1 Condition number for different configurations

Case	Condition number
MI-PAT, 1 source, 64 detectors	3.7764e+017
MI-PAT, 4 sources, 64 detectors	1.3061e+008
MI-PAT, 4 sources, 16 detectors	6.8934e+007
MI-PAT, 8 sources, 64 detectors	3.8724e+007
CW-DOT, 8 sources	1.7838e+013

4.4 Conclusions and Discussion

Our algorithm appears to be a promising way of reconstructing optical properties quantitatively using photoacoustic channel data. The use of multiple optical sources helps mitigate absorption-scattering non-uniqueness. The proposed algorithm performs image reconstruction and quantitative optical property estimation together in an iterative scheme.

Our approach is presently based on diffusion theory calculations. However, it may be generalized to incorporate the radiative transport equation (RTE). Though

RTE outperforms light diffusion models in reconstruction of optical properties in photoacoustic tomography [17], the diffusion approximation is a reasonable starting point. In our simulation setup, we also took into consideration the feasibility of the diffusion approximation and located light sources far from the object to be imaged. The Born approximation is utilized in our work. This limits our method to be validated with relatively small perturbations.

Additional nonlinear optimization methods should be explored to further improve reconstruction quality. Various constraints should be incorporated during inversion. One example is that Gao et al. [18] introduced the Bregman method combined with total variation regularization for reconstruction of optical properties in photoacoustic imaging. The ℓ_1 total variation regularization preserved sharp edges and therefore piece-wise continuous features in the recovered map. Simulation work demonstrated that their method outperformed the Jacobian matrix-based methods in terms of computational efficacy.

Our work has limitations. We simplified our work by assuming the Grüneisen parameter is constant throughout the object to be imaged. In practical scenarios, this may lead to inaccuracy in reconstruction of optical properties. We used the same theoretical model for both forward and inverse problems, but to avoid the ‘inverse crime’ we did add noise to our ‘measured’ data. It should also be straightforward to incorporate more realistic transducer aperture, directivity, and electromechanical response effects into future work involving experiments.

Bibliography

- [1] L. V. Wang, "Tutorial on photoacoustic microscopy and computed tomography," *IEEE J.Sel.Top.Quan.*, **14**, 171-179, 2008.

- [2] M. Xu and L. V. Wang, "Analytic explanation of spatial resolution related to bandwidth and detector aperture size in thermoacoustic or photoacoustic reconstruction," *Phys. Rev. E*, **67**, 056605, 2003.
- [3] Z. Guo, C. Li, L. Song and L. V. Wang, "Compressed sensing in photoacoustic tomography in vivo," *J. of Biomed. Opt.*, **15**, 121311, 2010.
- [4] B. Cox, J. G. Laufer, S. R. Arridge and P. C. Beard, "Quantitative spectroscopic photoacoustic imaging: a review," *J. of Biomed. Opt.*, **17**, 061202, 2012.
- [5] G. Bal and K. Ren, "Multi-source quantitative photoacoustic tomography in a diffusive regime," *Inv. Prob.*, **27**, 075003, 2011.
- [6] B. T. Cox, S. R. Arridge, K. P. Kostli and P. C. Beard, "Two-dimensional quantitative photoacoustic image reconstruction of absorption distribution in scattering media by," *App. Opt.*, **45**, 1866-1875, 2006.
- [7] Z. Yuan and H. B. Jiang, "Quantitative photoacoustic tomography: recovery of optical absorption coefficient maps of heterogeneous media," *Appl. Phys.*, **88**, 231101, 2006.
- [8] J. Ripoll and V. Ntziachristos, "Quantitative photo-acoustic tomography: recovery of optical absorption coefficient maps of heterogeneous media," *Phys. Rev. E*, **71**, 031912, 2005.
- [9] B. Banerjee, S. Bagchi, R. M. Vasu and D. Roy, "Quantitative photoacoustic tomography from boundary pressure measurements: noniterative recovery of optical absorption coefficient from the reconstructed absorbed energy map," *J. Opt. S. Am. A*, **25**, 2347-2356, 2008.

- [10] L. Yin , Q. Wang, Z. Zhang and H. B. Jiang, "Tomographic imaging of absolute optical absorption coefficient in turbid media using combined photoacoustic and diffusing light measurements," *Opt. Lett.*, **32**, 2556-2558, 2007.
- [11] T. Jetzfellner, D. Razansky, A. Rosenthal, R. Schulz, K. -H. Englmeier and V. Ntziachristos, "Performance of iterative photoacoustic tomography with experimental data," *Appl.Phys. Lett.*, **95**, 013703, 2009.
- [12] B. T. Cox, S. R. Arridge and P. C. Beard, "Estimating chromophore distributions from multiwavelength photoacoustic images," *J. Opt. S. Am.*, vol. **26**, 443-455, 2009.
- [13] G. Bal and K. Ren, "On multi-spectral quantitative photoacoustic tomography in diffusive regime," *Inv.Prob.*, **28**, 025010, 2012.
- [14] R. J. Zemp, "Quantitative photoacoustic tomography with multiple optical sources," *App.Opt.*, **49**, 3566-3572, 2010.
- [15] P. Shao, B. Cox and R. J. Zemp, "Estimating optical absorption, scattering, and Grueneisen distributions with multiple-illumination," *Appl. Opt.*, **50**, 1-11, 2011.
- [16] L. V. Wang and H.-I. Wu, *Biomedical Optics: principles and imaging*, Hoboken, New Jersey: Wiley, 2007.
- [17] B. Cox, T. Tarvainen and S. Arridge, in *Contemporary Mathematics* (Portland, Book News Inc., 2011), 1-12.

- [18] H. Gao, H. Zhang and S. Osher , "Bregman methos in quantitative photoacoustic tomoraphy," CAM report, **10-42**, 2010.

5. Consecutively Reconstructing Absorption and Scattering Distributions in Known Turbid Media with Multiple-Illumination Photoacoustic Microscopy (MI-PAT)¹

5.1 Introduction

Photoacoustic (PA) imaging has been intensively studied recently because of its promise for high resolution and intrinsic optical contrast [1]. Efforts have been directed to quantitative estimation of optical properties (absorption μ_a and scattering μ_s), and the Grüneisen parameter distributions based on photoacoustic tomography, which may significantly enhance clinical and biomedical applications of PA imaging. This is usually termed quantitative photoacoustic tomography (qPAT), which usually involves two steps. The first step is a well-studied acoustic inverse problem, which aims to reconstruct photoacoustic initial pressure distribution using recorded acoustic data generated by a wide field pulse laser [2][3][4]. The second step is to estimate optical properties μ_a and μ_s , in the target imaged. This is essentially a rather challenging optical inverse problem. Quite a number of approaches has been proposed for the second step of qPAT. Studies were first focused on μ_a estimation [5][6], later extended to include scattering [7][8][9][10]. Multiple-wavelength [11][12] or optical sources [13][14][15][16] were also proposed to mitigate the absorption-scattering non-uniqueness problem.

¹ A version of this chapter has been submitted to *J. Biomed. Opt.*, 2014.

Diffuse optical measurements were also used also to assist estimate μ_a in PAT [17] [18]. A thorough review on qPAT is provided by Cox et al. [19].

The fixed-point iterative scheme for estimating optical absorption distribution was first proposed by Cox et al. [6]. With this method, absorption map is estimated in each iteration and then used to update fluence distribution for the next iteration. With simulaitons based on a diffusion-based finite-element model, the authors demonstrated that the algorithm converges fast and the absorption distribution could be reconstructed accurately. Jetzfellner et al. [20] examined the performance of this scheme with experimental data. With a tissue-mimcking phantom, PA imaging was conducted with circular illumination with a high intensity near infrared pulsed laser. The authors argued the iterative method is sensitive to background optical properties and diverges over iterations.

Recently Harrison et al. [21] extended the aforementioned iterative method [6] to a least-squares fixed-point iterative method for reconstructing absorption maps in multiple-illumination photoacoustic tomography (MIPAT). With the proposed method, convergence of the inversion is significantly improved when multiple iterations is utilized. This approach is efficient and stable to accomplish as it does not require computation of Jacobian-matrix. However, the aforementioned methods are restricted to reconstructing only absorption distributions.

In the present paper, we intend to extend our previous work to recover both absorption and scattering perturbation distributions in a known turbid media, which holds a typical value of background scattering in soft tissue. We accomplish this task in an iterative manner. For each iteration, absorption maps is first estimated with the least-squares fixed-point iterative method by Harrison et al. [21]. Optical fluence distribution is then updated, whereupon scattering coefficient perturbation distribution is estimated. This procedure is then repeated for multiple times until an

acceptable error is reached.

5.2 Method

5.2.1 Light propagation model

qPAT is in essence inversion of a light transport model. We use the diffusion equation in this paper as the light propagation model. In photoacoustic imaging, pulsed laser must be used to excite transient acoustic generation, and the pulse duration is significantly longer than the average random-walk time of photons though the tissue. Therefore a time-independent form of the equation is usually utilized. For a time-independent point source with strength A in an infinite turbid homogeneous medium, the equation has the following form [22]:

$$\frac{\mu_a}{D} \Phi(\mathbf{r}) - \nabla^2 \Phi(\mathbf{r}) = \frac{A}{cD} \delta(\mathbf{r}), \quad (5.1)$$

where Φ is the optical fluence, A is the photon density source strength. μ_a is the absorption coefficient. D is the so-called diffusion coefficient, which is defined as $1/3(\mu_s + \mu_s')$. μ_s' in the above expression is the reduced scattering coefficient, which may be calculated by $\mu_s' = (1 - g)\mu_s$ with the anisotropy g . In diffuse theory, scattering is usually described with μ_s' , or D . In this study, we use D . To validate the diffusion theory, $\mu_s' \gg \mu_a$ is required, which is often satisfied in soft tissue at near-infrared wavelengths.

5.2.2 Reconstruction of absorption distribution

In MIPAT, the transient initial pressure distribution due to source i for a certain optical wavelength is [2]

$$p_i(\mathbf{r}) = \Gamma(\mathbf{r})\mu_a(\mathbf{r})\Phi_i(\mathbf{r}). \quad (5.2)$$

With the least-squares fixed-point iterative method [21], absorption at location \mathbf{r} is estimated by

$$\widehat{\mu}_a^{(i+1)}(\mathbf{r}) = \frac{1}{\Gamma} \frac{\sum_k \widehat{\Phi}_k^{(i)}(\mathbf{r}) \hat{p}_0^k(\mathbf{r})}{\sum_k \left[\widehat{\Phi}_k^{(i)}(\mathbf{r}) \right]^2 + \beta^2}, \quad (5.3)$$

where $\widehat{\mu}_a^{(i+1)}(\mathbf{r})$ is the estimated absorption with the $(i+1)^{\text{th}}$ iteration and $\widehat{\Phi}_k^{(i)}$ is the updated fluence due to source k with the previous absorption map in the i^{th} iteration. $\hat{p}_0^k(\mathbf{r})$ is the reconstructed initial pressure distribution due to source k . β is a regularization parameter to stabilize the computation.

5.2.3 Reconstruction of the diffusion coefficient perturbation distribution

The relation between the measured data $p_i(\mathbf{r})$ and $[\mu_a(\mathbf{r}), D(\mathbf{r})]$ is nonlinear, because optical fluence at location \mathbf{r} is also a function of local optical properties. However, if we have an estimation of the absorption distribution $\widehat{\mu}_a(\mathbf{r})$, the problem is simplified as the contribution of absorption to $\widehat{\Phi}_i(\mathbf{r})$ is known. Equation (5.2) is rewritten as,

$$p_i(\mathbf{r}) = \Gamma(\mathbf{r}) \widehat{\mu}_a(\mathbf{r}) \widehat{\Phi}_i(\widehat{\mu}_a(\mathbf{r}), D(\mathbf{r})). \quad (5.4)$$

To linearize the problem, we further decompose the local optical fluence at position \mathbf{r} as $\widehat{\Phi}_i(\mathbf{r}) = \widehat{\Phi}_{i,o}(\mathbf{r}) + \delta\widehat{\Phi}_{i,a}(\mathbf{r}) + \delta\widehat{\Phi}_{i,s}(\mathbf{r})$, which is a sum of known homogeneous background fluence ($\widehat{\Phi}_{i,o}(\mathbf{r})$) due to known background absorption and scattering properties, and fluence perturbations due to absorption and scattering:

$\delta\widehat{\Phi}_{i,a}(\mathbf{r})$ and $\delta\Phi_{i,s}(\mathbf{r})$.

Equation (5.4) now becomes

$$p_i(\mathbf{r}) = \Gamma(\mathbf{r}) \widehat{\mu}_a(\mathbf{r}) [\widehat{\Phi}_{i,o}(\mathbf{r}) + \delta\widehat{\Phi}_{i,a}(\mathbf{r}) + \delta\Phi_{i,s}(\mathbf{r})]. \quad (5.5)$$

In the above equation, the only unknown term is $\delta\Phi_{i,s}(\mathbf{r})$, the fluence perturbation due to scattering diffusion coefficient abnormalities. In this study, an extrapolated boundary condition is used (with zero inward flux) [22]. We assume that $\delta\Phi_{i,s}(\mathbf{r})$ is linearly related to $\delta D(\mathbf{r})$, which limits our study to the linear case such that $\delta\Phi_{i,s}(\mathbf{r}) \ll \Phi_{i,o}(\mathbf{r})$, and $\Phi_i \cong \Phi_{i,o}$, we have the following relation based on the first-order Born approximation [14],

$$\delta\Phi_{i,s}(\mathbf{r}) = \int \frac{\delta D(\mathbf{r}')}{D_o} \nabla G_0(\mathbf{r}, \mathbf{r}') \cdot \nabla \Phi_{i,o}(\mathbf{r}') d\mathbf{r}'. \quad (5.6)$$

Here $G_0(\mathbf{r}, \mathbf{r}')$ is Green's function representing propagation from \mathbf{r} to \mathbf{r}' . $\delta\Phi_{i,s}(\mathbf{r})$ can be estimated from equation (5.5):

$$\delta\Phi_{i,s}(\mathbf{r}) = \frac{p_k(\mathbf{r})}{\Gamma \widehat{\mu}_a(\mathbf{r})} - \widehat{\Phi}_{i,o}(\mathbf{r}) - \delta\widehat{\Phi}_{i,a}(\mathbf{r}). \quad (5.7)$$

If we discretize equation (5.7) and write it in a matrix form as

$$\Phi_{sc} = \mathbf{W}\mathbf{u}, \quad (5.8)$$

where \mathbf{W} is the Jacobian matrix, or sensitivity matrix and \mathbf{u} is the vector which contains the unknown diffusion coefficient perturbation map $\delta D(\mathbf{r})$ to estimate.

This is a well-formatted linearized inverse problem and can be solved with a number of techniques. We use the least-squares minimization with total variation regularization:

$$\mathbf{u} = \operatorname{argmin}_{\mathbf{u}} \|\Phi_{sc} - \mathbf{W}\hat{\mathbf{u}}\|_2^2 + \lambda|\hat{\mathbf{u}}|_{TV}. \quad (5.9)$$

λ in the above equation serves as the trade-off parameter for inversion. To determine the value of λ , we use the classic L -curve technique to balance the resulting errors in the first and second term [23].

We propose to repeat this procedure with multiple iterations to accomplish the imaging task until a preset tolerance is reached following the flowchart in Fig. 5.1. Before entering the iteration loop, we set the initial guess of the absorption as zero. In each iteration, we first update the fluence distribution with estimated $[\mu_a, D]$ from last the iteration. Then we reconstruct D with the updated fluence distribution, whereupon a new version of optical fluence is generated, based on which absorption is again modified if a tolerance is not yet reached. The iterative reconstruction is repeated till a satisfactory result is reached.

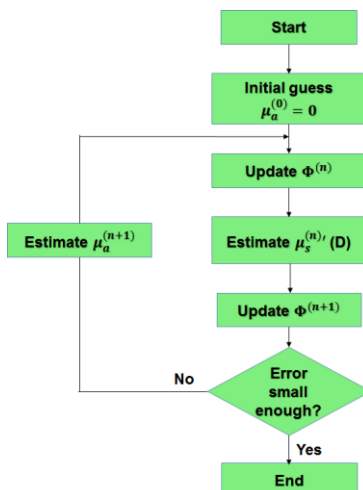


Fig. 5.1 Flow chart of the iterative method.

5.3 Simulation

Simulation studies were conducted to examine the performance of the proposed scheme. All simulation were conducted on a region of interest composed of 2-dimensional 40×40 mesh grid system, whose dimension is set to be $20 \text{ mm} \times 20 \text{ mm}$, except for otherwise stated. To mitigate inversion crime, the synthetic data were generated on a larger grid system (43×43) and down-sampled to 40×40 with the cubic interpolation for inversion. 16 optical sources positioned 3 mm backward from the object to validate the diffusion light propagation model. Background optical properties of the object were taken as the physiologically realistic values in biological soft tissue. Absorption and the reduced scattering coefficient are 0.1 cm^{-1} and 100 cm^{-1} , respectively.

We first tested our algorithm with regular overlapping features, as is shown in Fig. 5.2. Two rectangular features with absorption perturbations (10% on the left and 5% on the right) and diffusion coefficient anomalies (5% on the left and 10% on the right) were positioned in the center of the field of view. While noise with

normal distribution corresponding to an average SNR of ~ 30 dB were added to ‘reconstructed’ PAT image. For inversion, we use zero as initial guess for both absorption map and diffusion coefficient distribution. In each iteration, μ_a was estimated for 20 times before optical fluence was updated. Reconstructed results with iteration 1, 2 10 and 50 are employed to show improvement of estimation as more iterations are involved.

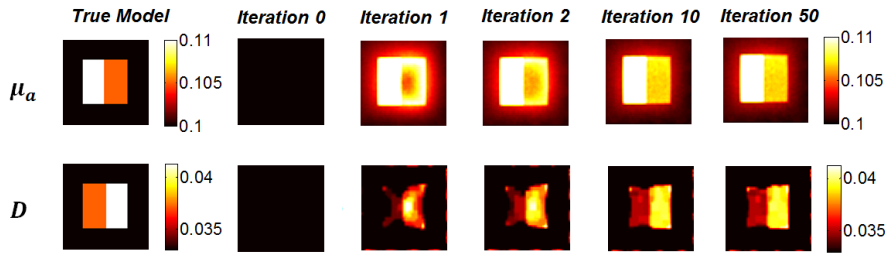


Fig. 5.2 Reconstruction of optical property distributions with the proposed method. Initial values were chosen to be zero for both absorption and diffusion coefficient distributions. Results with iteration #1, #2, #10 and #50 are shown to demonstrate that results are improved with more iterations.

To examine the capability of the method to recover arbitrary features rather than regular shapes, features with both discrete strips with sharp edges and smoothed features were tested, as is shown in Fig. 5.3. In (a), sharp strip features, which share similarities with biological structures such as blood vessels, with 10% absorption and scattering perturbations were reconstructed. We also tested four smoothed absorption perturbations (0.1 cm^{-1} , 0.09 cm^{-1} , 0.07 cm^{-1} and 0.05 cm^{-1} , respectively) and two diffusion coefficient anomalies (0.0083 cm^{-1} and 0.0042 cm^{-1}) with different spatial locations in the background. Synthetic data were generated with a SNR of ~ 30 and 20 iterations were used for inversion.

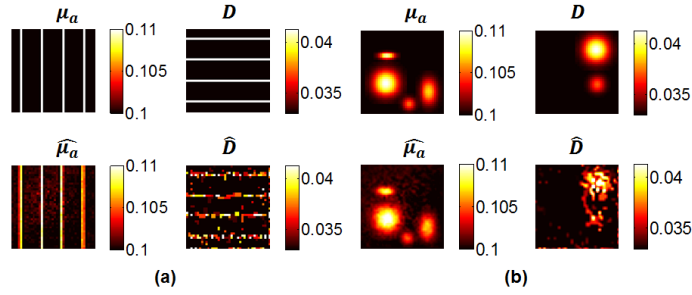


Fig. 5.3. Reconstruction of sharp (a) and smoothed features (b) with the proposed method with 20 iterations. In (a), Anomalies of both absorption and diffusion coefficient was set at 10% of the background value. Perturbations of 10%, 9%, 7% and 5% of the background absorption, 20% and 10% of the background diffusion coefficient at various locations was used in (b). SNR of synthetic data was ~ 30 dB.

Cross-talk between reconstructed maps of the two parameters is a concern, because diffusion coefficient depend on both absorption and scattering: $D(\mathbf{r}) = 1/3(\mu_a(\mathbf{r}) + \mu_s'(\mathbf{r}))$. Artefacts due to absorption might occur in reconstructed diffusion coefficient distribution. We tried estimating two non-overlapping features to examine cross-talk between the two properties in recovered results (Fig. 5.4). Interestingly, whereas no artefacts due to absorption appeared in the reconstructed D , we did observe artefacts in reconstructed absorption map where diffusion perturbations lie. However, the pseudo-feature is alleviated within several iterations and was finally removed from the results. This might be because that in each iteration, we update the absorption distribution, thus dependence of D on μ_a is significantly mitigated and it is negligible already before reconstructing the scattering feature. On the other hand, while we estimate absorption map, the contribution of scattering features is still functioning and brings about artefacts in the recovered μ_a . But with more iterations involved, optical fluence is updated repeatedly and getting closer to its real status, therefore artefacts are removed. It is not surprise that with a single source, a unique solution for $[\mu_a, D]$ estimation is

not achieved. This is due to the non-uniqueness problem.

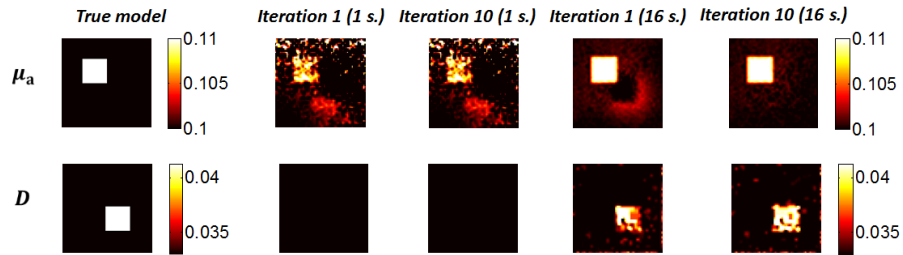


Fig. 5.4. Reconstruction with non-overlapping features to demonstrate capabilities of the algorithm to alleviate cross-talk between absorption and diffusion coefficient. Reconstruction results when using 1 and 16 illuminations are shown. Artefacts appeared in the reconstructed absorption map where diffusion coefficient anomalies locates. But with more iterations involved, the artefacts was removed when multiple-sources were used.

Figure 5.5 shows reconstruction of a realistic synthetic blood vessel structure of $10 \text{ mm} \times 10 \text{ mm}$. From left to right are true model, reconstruction results with SNR of infinity (0 noise), $\sim 30 \text{ dB}$ and $\sim 20 \text{ dB}$, respectively. We also show the cross-sectional profiles of corresponding results in the center of the distributions in Fig. 5.6. With data that has a SNR of $\sim 30 \text{ dB}$, absorption features are faithfully estimated. More artefacts appeared in the results computed with 20 dB data.

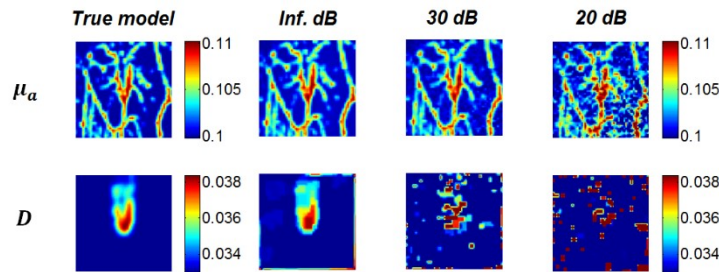


Fig. 5.5. Reconstruction of a synthetic blood vessel vasculature. Left column is the true $[\mu_a, D]$ model. Second to the last column are reconstruction results with average SNR of infinity (no noise), $\sim 30 \text{ dB}$ and $\sim 20 \text{ dB}$.

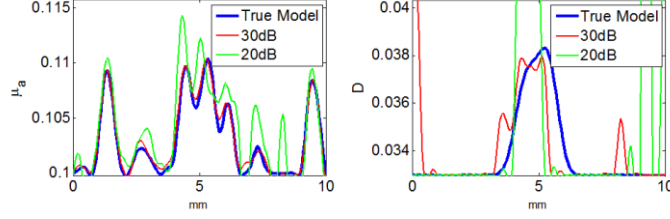


Fig. 5.6. Cross-sectional profiles of the reconstruction results along horizontal direction in the center of the true model in Figure 5.5. All features of μ_a was faithfully reconstructed with the ~ 30 dB data. Artefacts appeared in the reconstruction with data that has a SNR of ~ 20 dB. Despite some artefacts, D features were recovered with a ~ 30 dB SNR. Amplitude errors were unacceptable for data with ~ 20 dB SNR.

Figure 5.7 depicts the relation between reconstruction errors from the last example and number of optical sources involved. Errors were calculated with the following formula [20],

$$\varepsilon = \frac{\sqrt{\int \int |U - U_n|^2 dx dy}}{\sqrt{\int \int |U|^2 dx dy}} \quad (10)$$

where U and U_n are the intensity of true model and the reconstructed maps with the n^{th} iteration. The algorithm converges in the first few iterations and remains stable even with a large number of iterations. The number of optical sources matters for reconstruction quality. With more illuminations utilized reconstruction errors for both $[\mu_a, D]$ decreased immediately. But D benefits more and reconstruction errors drops more significantly. Considering that usually μ_a is better resolved than scattering features in qPAT [24], this suggests that multiple-illumination pattern does yield higher reconstruction quality by providing more information. We used 16 optical sources for studies in previous examples as it yields faithful results.

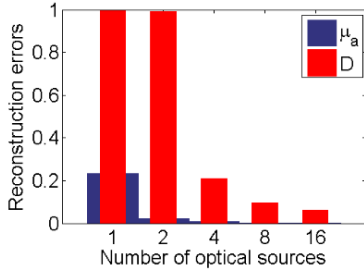


Fig. 5.7. Reconstruction errors with different number of optical sources.

Fast convergence was seen as a remarkable advantage of the least-squares fixed-point MIPAT approach [21]. We plot the relative errors of reconstruction in Fig. 5.8 as an illustration of overall convergence ability of the proposed scheme. Reconstruction errors decreases quickly and stabilizes within the first 10 iterations.

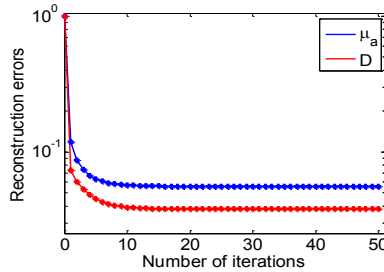


Fig. 5.8. Normalized reconstruction errors with 50 iterations. Both μ_a and D converge in a few iterations and stay stable after a large number of iterations.

5.4 Conclusion and discussion

We have proposed a consecutive reconstruction scheme to estimate optical absorption and diffusion coefficient perturbation distributions in known turbid medium for multiple-illumination photoacoustic microscopy (MIPAT). With this approach, absorption map is first estimated, whereupon optical fluence is updated and then diffusion coefficient distribution is reconstructed. The absorption distribution is recovered with a least-squares fixed-point iterative method. Numerical simulations demonstrated that both the optical properties can be

faithfully reconstructed with the presence of noise at a SNR level of ~ 30 dB. This method converges fast and is robust to cross-talk of overlapping and non-overlapping features.

Conventional iterative methods for qPAT suffers from computational complexity, instability and poor convergence performance. The least-squares fixed-point iterative methods [21] to recover absorption in our previous report does not require inversion of large scale Hessian- or Jacobian- matrix, therefore it is computationally efficient and stable. The reconstruction can be done on a resolution scale equivalent to the fine resolution obtainable by backprojection or other model-based inversion approaches. Convergence is substantially improved. These advantages enable the faithfully estimated absorption serve as a compulsory guide for each iteration in the current method. Updated fluence estimate based on the reconstructed absorption map assisted accurate estimation of the scattering features. We did not study convergence of the algorithm with a much more scattering background as described in [20] as we restrict our study in the scope of realistic biological soft tissue. While various approaches have been proposed for quantitative reconstructions of optical distributions, most previous approaches were not sufficiently tolerant to realistic noise levels. Prior to experimental work we argue it is essential to develop imaging strategies and algorithms for sufficiently noise-robust. In this manuscript we demonstrate the ability to reconstruct both absorption and scattering distributions with realistic noise levels.

Our study has limitations. The result in this paper is based on the approximate light propagation model in the diffuse regime. Whereas many studies used the diffuse approximation for qPAT, it is verified that the radiative transfer equation model [24] provides better estimation. It is worth trying to extend our current study to more accurate theoretical models. Similar to most of the literature on this topic,

we also assume that ideal reconstruction of the photoacoustic images from measured acoustic data. While one option to avoid this is to use the ultrasonic channel data as proposed by our previous report [16], one can also follow the framework by Saratoon et al. [25] to include acoustic reconstruction to study its influence on the final reconstruction results. Reconstruction of scattering distributions still requires matrix inversion, as do all other Diffuse Optical Tomographic (DOT) methods thus far. The matrix condition number is comparable with previous DOT/PAT approaches and the reconstruction can be done on a coarser scale to accommodate regularization (data not shown). We utilized this method as a preliminary example. We partially committed the ‘inverse crime’ in this paper, which refers to the act to generate, as well as to invert synthetic data with the same theoretical model or discretization. Since we use the same theoretical model for both forward and inverse problem, We 1) generated synthetic data on a larger grid system (with an odd-number of grid) and then down-sampled the dataset with a smaller system (even number of grid points) for inversion; 2) added white noise with normal distribution to all experimental data to mitigate this issue. To extend our simulation work to experiments is enlisted as our future work. As a preliminary work, recently we have reported a reflection-mode photoacoustic technique that can be used for optical properties sensing [26].

In summary, we provided an alternative, but stable and practical framework for quantitative estimation of overall absorption distribution and scattering perturbations in known biological media, despite that our current approach still need a somewhat more complex experimental setup.

Bibliography

- [1] M. Xu and L. V. Wang, “Photoacoustic imaging in biomedicine,” *Rev. Sci. Instrum.*, vol. 77, no. 4, p. 041101, 2006.
- [2] X. Wang, Y. Xu, M. Xu, S. Yokoo, E. S. Fry, and L. V. Wang, “Photoacoustic tomography of biological tissues with high cross-section resolution: Reconstruction and experiment,” *Med. Phys.*, vol. 29, no. 12, pp. 2799–2805, 2002.
- [3] M. Xu and L. Wang, “Universal back-projection algorithm for photoacoustic computed tomography,” *Phys. Rev. E*, vol. 71, no. 1, p. 016706, Jan. 2005.
- [4] K. Wang, R. Su, A. a Oraevsky, and M. a Anastasio, “Investigation of iterative image reconstruction in three-dimensional optoacoustic tomography,” *Phys. Med. Biol.*, vol. 57, no. 17, pp. 5399–5423, Sep. 2012.
- [5] Z. Guo, S. Hu, and L. V Wang, “Calibration-free absolute quantification of optical absorption coefficients using acoustic spectra in 3D photoacoustic microscopy of biological tissue,” *Opt. Lett.*, vol. 35, no. 12, pp. 2067–9, Jun. 2010.
- [6] B. T. Cox, S. R. Arridge, K. P. Köstli, and P. C. Beard, “two-dimensional quantitative photoacoustic image reconstruction of absorption distribution in scattering media by use of a simple iterative method,” pp. 4–6, 2006.

- [7] Z. Yuan and H. Jiang, “Quantitative photoacoustic tomography,” *Philos. Trans. A. Math. Phys. Eng. Sci.*, vol. 367, no. 1900, pp. 3043–3054, Aug. 2009.
- [8] J. Ripoll and V. Ntziachristos, “Quantitative point source photoacoustic inversion formulas for scattering and absorbing media,” *Phys. Rev. E*, vol. 71, no. 3, p. 031912, Mar. 2005.
- [9] G. Bal and G. Uhlmann, “Inverse diffusion theory of photoacoustics,” *Inverse Probl.*, vol. 26, no. 8, p. 085010, Aug. 2010.
- [10] H. Gao, H. Zhao, and S. Osher, “Quantitative Photoacoustic Tomography,” pp. 1–27.
- [11] B. T. Cox, S. R. Arridge, and P. C. Beard, “Estimating chromophore distributions from multiwavelength photoacoustic images,” *J. Opt. Soc. Am. A. Opt. Image Sci. Vis.*, vol. 26, no. 2, pp. 443–55, Feb. 2009.
- [12] G. Bal and K. Ren, “On multi-spectral quantitative photoacoustic tomography in diffusive regime,” *Inverse Probl.*, vol. 28, no. 2, p. 025010, Feb. 2012.
- [13] R. J. Zemp, “Quantitative photoacoustic tomography with multiple optical sources,” *Appl. Opt.*, vol. 49, no. 18, pp. 3566–3572, Jun. 2010.
- [14] P. Shao, B. Cox, and R. J. Zemp, “Estimating optical absorption, scattering, and Grueneisen distributions with multiple-illumination photoacoustic tomography,” *Appl. Opt.*, vol. 50, no. 19, pp. 3145–54, Jul. 2011.

- [15] G. Bal and K. Ren, "Multi-source quantitative photoacoustic tomography in a diffusive regime," *Inverse Probl.*, vol. 27, no. 7, p. 075003, Jul. 2011.
- [16] P. Shao, T. Harrison, and R. J. Zemp, "Iterative algorithm for multiple illumination photoacoustic tomography (MIPAT) using ultrasound channel data," *Biomed. Opt. Express*, vol. 3, no. 12, pp. 3240–3249, Dec. 2012.
- [17] C. Xu, P. D. Kumavor, A. Aguirre, and Q. Zhu, "Investigation of a diffuse optical measurements-assisted quantitative photoacoustic tomographic method in reflection geometry," *J. Biomed. Opt.*, vol. 17, no. 6, p. 061213, Jun. 2012.
- [18] L. Yin, Q. Wang, Q. Zhang, and H. Jiang, "Tomographic imaging of absolute optical absorption coefficient in turbid media using combined photoacoustic and diffusing light measurements," *Opt. Lett.*, vol. 32, no. 17, pp. 2556–2558, 2007.
- [19] B. Cox, J. G. Laufer, S. R. Arridge, and P. C. Beard, "Quantitative spectroscopic photoacoustic imaging: a review," *J. Biomed. Opt.*, vol. 17, no. 6, p. 061202, Jun. 2012.
- [20] T. Jetzfellner, D. Razansky, A. Rosenthal, R. Schulz, K.-H. Englmeier, and V. Ntziachristos, "Performance of iterative optoacoustic tomography with experimental data," *Appl. Phys. Lett.*, vol. 95, no. 1, p. 013703, 2009.
- [21] T. Harrison, P. Shao, and R. J. Zemp, "A least-squares fixed-point iterative algorithm for multiple illumination photoacoustic tomography," *Biomed. Opt. Express*, vol. 4, no. 10, pp. 2224–2230, Jan. 2013.

- [22] L. V. Wang and H. Wu, *Biomedical Optics, principles and imaging*. Willey-Interscience, 2007.
- [23] P. C. Hansen, “The L-curve and its use in the numerical treatment of inverse problems,” *Adv. Comput. Bioeng.*, vol. 4, pp. 119–142.
- [24] B. T. Cox, T. Tarvainen, and S. Arridge, “Multiple illumination quantitative photoacoustic tomography using transport and diffusion models,” in *Tomography and Inverse Transport Theory*, 2011.
- [25] T. Saratoon, T. Tarvainen, B. T. Cox, and S. R. Arridge, “A gradient-based method for quantitative photoacoustic tomography using the radiative transfer equation,” *Inverse Probl.*, vol. 29, no. 7, p. 075006, Jul. 2013.
- [26] J. C. Ranasinghesagara, Y. Jiang, and R. J. Zemp, “Reflection-mode multiple-illumination photoacoustic sensing to estimate optical properties,” *Photoacoustics*, vol. 2, no. 1, pp. 33–38, Mar. 2014.

6. Integrated Micro-endoscopy System for Simultaneous Fluorescence and Optical-Resolution Photoacoustic Imaging (OR-PAM)¹

6.1 Introduction

Optical-resolution photoacoustic microscopy (OR-PAM) is capable of sensing endogenous optical absorption in biological bodies with fine lateral resolution provided by optical focusing. Pioneered by Maslov et al. [1], OR-PAM imaging has been successfully applied to both structural and functional imaging [2]-[9]. Since both oxy- and deoxyhemoglobin are the dominant absorbing components in blood, the distribution of optical absorption, detected by the OR-PAM system can be used to recover oxygen saturation (SO_2). For example, Hu et al. [10] used OR-PAM to image SO_2 with capillary-level resolution in mouse brain with dual-wavelength measurements. Hu et al. [11] also imaged the healing process of laser-induced microvascular lesions in a small animal model in vivo in terms of morphological and SO_2 mapping. These studies demonstrated the capability of OR-PAM as a potential powerful tool in microcirculatory physiology and pathophysiology.

Recently our group reported the first label-free fiber-based OR-PAM (F-OR-PAM) imaging systems [12, 13]. The system retains many of the powerful properties of our previously proposed table-top system [14]. It takes advantage of

¹ A version of this chapter has been published. Reprint with permissions from: P. Shao, W. Shi, P. Hajireza and R. J. Zemp, *J. Biomed. Opt.* 17(7), 070624, 2012. Copyright 2012 SPIE.

a flexible image guide and has significant potential to serve as a new micro-endoscopic imaging technique for clinical use. Visualization of microvasculature in living mouse ears was demonstrated with the system.

Fluorescence contrast high-resolution fiber-optic micro-endoscopy (HRME) was introduced by Muldoon et al. [15]. This technique, which is inspired by the goal of virtual histopathology, utilizes a microscopic setup to image fluorescently-labelled cellular structures with lateral resolution on the order of microns. Fluorescent signals excited by a wide-field light source are magnified and sensed by a CCD camera. Rosbach et al. [16] justified the feasibility of the imaging modality in evaluating lymph nodes from breast cancer patients with morphological variation. Muldoon et al. [16] verified the validity of the technique in assisting diagnosis of oral lesions by observing and analyzing morphology of epithelia in human oral cavities.

In the present paper, we propose a combined system based on the HRME technique and our previous F-OR-PAM system, with the purpose of engineering a hybrid imaging platform to visualize capillary vasculatures along with cellular context.

6.2 Method

The dual modality imaging platform consists of two modules (Fig. 6.1). The F-OR-PAM system employs a 532-nm diode-pumped Ytterbium-doped fiber laser system as the optical source (GLP-10, IPG Photonics Corporation). Pulse repetition rate (PRR) of the laser system is tunable within the range from 20 kHz to 600 kHz. Pulse duration is ~ 1 ns and the pulse energy can reach up to 20 μ J. A pair of 2D galvanometer scanning mirrors (6230H, Cambridge Technology Inc.) is utilized to accomplish optical scanning. The scanners are driven by two analog sinusoidal waves (x - and y - direction) from a function generator. The scanned beam is then

focused by an objective lens ($f=18$ mm, K16033703, Mitutoyo Co.) and directed into an image-guide fiber (FIGH-30-850, Myriad Fiber Imaging Tech. Inc.). Photoacoustic signals are sensed by a 3.5 MHz transducer (19-mm focus, 6-mm active element, $f\# = 3.17$, CD International Technology, Inc.), amplified and pre-filtered by a pulser-receiver (5900 PR, Olympus NDT Inc.) and then digitized by a 12-bit 8-channel high-speed digitizer (CS8289, Gage Applied Technologies Inc.) along with the higher frequency (x -axis) scanning feedback signals. For the fluorescent sub-system, a 447.5-nm-centered diode laser is utilized as the excitation light source. A standard fluorescent filter unit is employed in the system. An exciter band-pass filter with a center wavelength (Thorlabs Inc.) of 445 nm is utilized. A 475-nm cut-off dichroic mirror (Chroma Technology Corp.) is used to reflect excitation light while transmitting excited fluorescence signals directed back. Excited fluorescence signals travel back through the image guide, reflected by the beam splitter positioned above the objective lens and then follow the light path to the scientific grade high-resolution Electron-Multiplied CCD (EM-CCD, Andor iXon 885, Andor Technology). To rule out noise in the fluorescence signals, we use a 500-nm long-pass barrier filter (Thorlabs Inc.) between dichroic mirror and tube lens. Pixel size of the CCD is $8 \mu\text{m} \times 8 \mu\text{m}$ and there are 1002×1004 pixels in total. The objective lens and the tube lens function together as a microscopic system. We use a plano-convex lens with a focal length of 150 mm (Thorlabs Inc.) as the tube lens and therefore the magnification factor of the system is ~ 8.3 . Proflavine, a FDA-approved drug for human medical use is utilized as the contrast agent. In soft tissue, proflavine stains nuclei. This is important since nuclei are often enlarged in cancer cells. Since the 532-nm laser is away from the absorption spectrum of Proflavine, no fluorescence signals will be generated by our OR-PAM optical source.

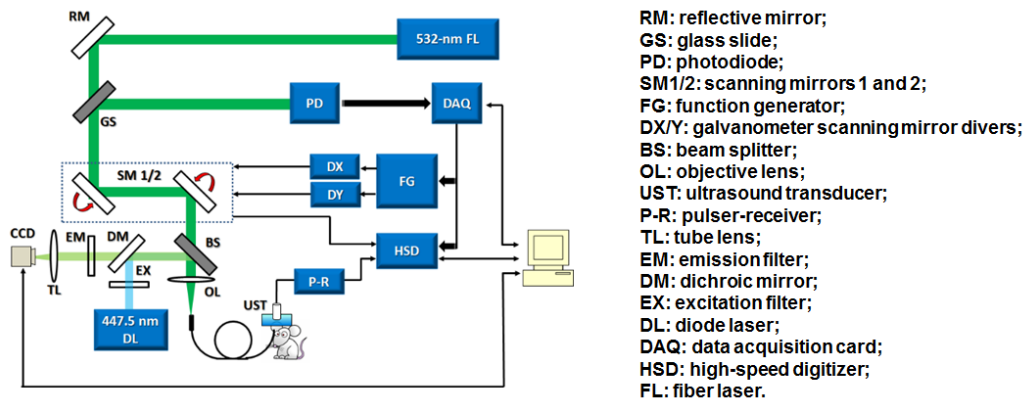


Figure 6.1 Experimental setup for the combined photoacoustic and fluorescence micro-endoscopy imaging system. The system is composed of an OR-PAM subsystem and a fluorescence microscopy system. A 2D galvanometer scanning mirror pair is used for raster optical scanning of the focused laser pulse. In the fluorescence imaging subsystem, excitation light is selected with an excitation filter and a dichroic mirror and directed by a beam splitter to share the same light path as the laser beam through the objective lens and the image guide to the target. Fluorescence energy is then reflected back through the dichroic mirror and then focused by a tube lens to the high resolution CCD camera.

The image guide we used, which consists of 30,000 single mode fibers in a bundle, has a diameter of $\sim 800 \mu\text{m}$. Considering the magnification factor of the microscope system, each single fiber covers 4.7 pixels of the EM-CCD on average, which is above the Nyquist limit.

The software package for data acquisition and data transfer is written in C/C++ and data processing and analysis is conducted with Matlab (Mathworks Inc.).

6.3 Results

6.3.1 System characterization

Figure 6.2 illustrates the system characterization of the imaging system. Fig. 6.2 (a) shows the entire footprint of the image guide we use, which has a diameter of ~ 800

μm . When the fluorescent imaging module is well-focused, single elements of the image guide can be visualized, as is shown in (b). This demonstrates that the module is capable of imaging features at a cellular level. To examine the lateral resolution of the fluorescent module, we imaged a 1951 United States Air Force resolution target (USAF 1951). Features with a dimension of $4.38 \mu\text{m}$ can be resolved, which suggests that the imaging module has a lateral resolution that is on the order as the F-OR-PAM sub-system. For properties of our F-OR-PAM module, readers can refer to [12] for details. (d) and (e) are images of a carbon fiber network obtained with both the two modules with fluorescent dye applied to the background. Contents in the two images are consistent. While carbon fibers appear as dark features in the fluorescent images, the F-OR-PAM image relies on photoacoustic signals from the fiber structures. The dual-modality imaging platform is capable of simultaneously providing two kinds of information that are supplementary to each other.

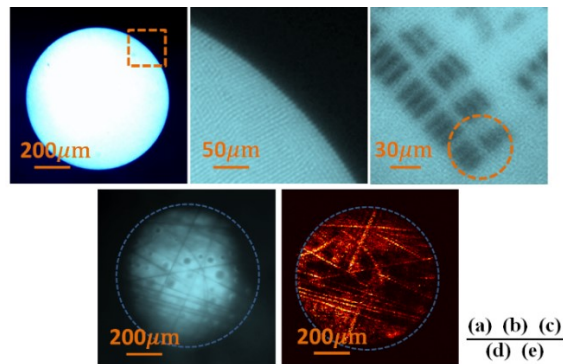


Figure 6.2 System characterization. (a) is the whole footprint of the image guide, with a diameter of $\sim 800 \mu\text{m}$. (b) is a zoomed-in version of the region in the dashed rectangle in (a). When the imaging system is well-focused, single elements of the image guide can be visualized. (c) is the image of the USAF 1951 resolution target taken with the fluorescent imaging system. Bars with a width of around $4.38 \mu\text{m}$ are resolved. (d) and (e) are the same carbon fiber network imaged with the fluorescent imaging module and the F-OR-PAM module sequentially. Consistent contents are visualized in the two images.

6.3.2 *In vivo* Imaging

In vivo studies were conducted to demonstrate imaging capability of our system. An ear of a 7-week old SCID hairless outbred mouse was imaged for *in vivo* studies. Experimental procedures follow the laboratory animal protocol approved by the University of Alberta Animal Use and Care Committee. An animal anesthesia system was utilized while image data were collected. Before the imaging experiment, we topically applied proflavine-saline solution with a concentration of 0.01% (w/v) to the ear skin surface. To avoid contamination of fluorescence image by our fiber laser, the fluorescent and F-OR-PAM images were taken sequentially in a few minutes after the dye was applied. But acquisition of the two images can be interlaced. The measured power of the excitation 455-nm light at distal end of the image guide is around 0.45 mW. The 532-nm laser works with PRR of 160 kHz. The average power measured at the distal end when conducting F-OR-PAM imaging is around 35mW. Results of the experiment are shown in Fig. 6.3. The scanning frequency of the galvanometer mirror system is 400 Hz and 1 Hz for the *x*- and *y*-axis, respectively. With the laser repetition rate of 160 kHz, the frame rate of the F-OR-PAM imaging sub-system is 2 frame per second, resulting in images with 160,000 points. (a) and (b) are the F-OR-PAM maximum amplitude projection (MAP) and fluorescent images of the mouse ear obtained at the same location, respectively. A 2D Hessian-based Frangi vesselness filter was used for data processing [18]. (c) is the co-registered image.

Figure 6.3 (d) is a fluorescence image of normal human oral mucosa taken with our system. After topical application of the fluorescent dye, distal end of the image guide was placed in contact with normal human oral mucosa to acquire fluorescent images. Staining of nuclei and cell membrane can be visualized clearly in the image.

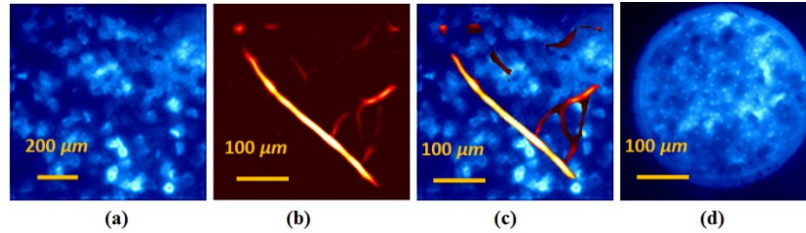


Figure 6.3. Results of in vivo experiments. (a) is the fluorescence image of the mouse ear taken at the same location where the F-OR-PAM image was obtained; (b) is the F-OR-PAM image; (c) co-registered image of (a) and (b). (d) Fluorescence image of normal human oral mucosa with topical application of Proflavine.

6.4 Conclusion and discussion

We demonstrated a hybrid imaging system for both F-OR-PAM-based vasculature and fluorescently labeled cellular structure imaging. We further provide cellular information on the micron-scale based on the OR-PAM system reported by our group [12] [13]. We believe that the concept shown in the present paper may lead to a more powerful tool for biomedical imaging.

A potential application of our system is the study and diagnosis of early-stage cancer. Whereas F-OR-PAM can provide images of vasculature (and potentially hemoglobin oxygenation) in tissue, cellular information may provide morphological context which is crucial for researchers and clinicians. For example, morphological anomalies in tumor tissue and variations in the micro-vasculatures due to cancer angiogenesis can confirm each other. This enables the technique to serve as a form of non-invasive virtual biopsy for identification of superficial tumor tissues in human cavities in diagnosis by clinicians. Estimate of SO_2 at capillary level, which is not possible with pure fluorescence imaging, can also be accomplished with dual-wavelength OR-PAM imaging [10]. This could help reveal metabolic status of the cancer tissue, which is proven to be of importance for both fundamental studies and clinical practices. Another example is vasa vasorum

imaging. Angiogenesis in this vascular layer of the lumen of atherosclerotic vessels has been correlated with plaque vulnerability. Visualizing the vessels could help provide one determinant of plaque vulnerability while fluorescent labelling could target immune cell invasion as an additional surrogate measure of rupture vulnerability.

We would like to note that though the fluorescent dye we use for the present project is not cell-specific, various dye materials can be utilized to label different cells, cell markers, or sub-cellular features in the soft tissue to generate contrast between tissue components. For example, the amine-reactive derivatives of fluorescein isothiocyanate (FITC), which is widely used for various applications such as anti-body labeling in immunofluorescence. The FDA-approved dye Indocyanine Green (ICG) [19] [20] has the advantage of near infrared excitation and could also be considered as a myriad of existing and emerging fluorescent reporters. Investigation of these dyes is warranted in our future work for novel potential applications.

Bibliography

- [1] K. Maslov, H. F. Zhang, S. Hu and L. V. Wang, "Optical-resolution photoacoustic microscopy for in vivo imaging of single capillaries," *Opt. Lett.* 33(9), 929-931, 2008.
- [2] S. Hu, K. Maslov and L. V. Wang, "Noninvasive label-free imaging of microhemodynamics by optical-resolution photoacoustic microscopy," *Opt. Express* 17(9), 7688-7963, 2009.
- [3] H. F. Zhang, K. Maslov, G. Stoica and L. V. Wang, "Functional photoacoustic microscopy for high-resolution and noninvasive in vivo imaging," *Nat. Biotech.* 24(7) 848-851 (2006). Hu S., Maslov K. and Wang L. V., "In vivo functional chronic imaging of a small animal model using optical-resolution photoacoustic microscopy," *Med. Phys.* 36(6), 2320-2323, 2009.
- [4] S. Hu, K. Maslov and L. V. Wang, "In vivo functional chronic imaging of a small animal model using optical-resolution photoacoustic microscopy," *Med. Phys.* 36(6), 2320-2323, 2009.
- [5] L. Song, K. Maslov and L. V. Wang, "Multifocal optical-resolution photoacoustic microscopy in vivo," *Opt. Lett.* 36(7), 1236-1238, 2011.
- [6] J. Yao, K. Maslov, Y. Shi, L. A. Taber and L. V. Wang, "In vivo photoacoustic imaging of transverse blood flow by using Doppler broadening of bandwidth," *Opt. Lett.* 35(9), 1419-1421, 2010.
- [7] V. Tsytsarev, S. Hu, J. Yan, K. Maslov, D. L. Barbour and L. V. Wang, "Photoacoustic microscopy of microvascular responses to cortical electrical stimulation," *J. Biomed. Opt.* 16(7), 076002, 2011.

- [8] A. Krumholz, S. J. Van Vickle-Chavez, J. Yao, W. E. Gillanders and L. V. Wang, "Photoacoustic microscopy of tyrosinase reporter gene in vivo," *J. Biomed. Opt.*, 16(8), 080503, 2011.
- [9] B. Rao, K. Maslov, A. Danielli, R. Chen, K. K. Shung, Q. Zhou and L. V. Wang, "Real-time four-dimensional optical-resolution photoacoustic microscopy with Au nanoparticle-assisted subdiffraction-limit resolution," *Opt. Lett.* 36(7) 1137-1139, 2011.
- [10] S. Hu, K. Maslov, V. Tsytsarev and L. V. Wang, "Functional transcranial brain imaging by optical-resolution photoacoustic microscopy," *J. Biomed. Opt.*, 14(4), 040503, 2009.
- [11] S. Hu, K. Maslov and L. V. Wang, "In vivo functional chronic imaging of a small animal model using optical-resolution photoacoustic microscopy," *Med. Phys.* 36(6) 2320-2323, 2009.
- [12] P. Haji reza, W. Shi and R. J. Zemp, "Label-free in vivo fiber-based optical-resolution photoacoustic microscopy," *Opt. Lett.* 36(20), 4107-4109, 2011.
- [13] Hajireza P., Shi W. and Zemp R. J., "Real-time handheld optical-resolution photoacoustic microscopy," *Opt. Express* 19(21), 20097-20102, 2011.
- [14] Shi W., Hajireza P., Shao P., Forbrich A. and Zemp R. J., "In vivo near-realtime volumetric optical-resolution photoacoustic microscopy using a high-repetition-rate nanosecond fiber-laser," *Opt. Express*, 19(18), 17143-17150, 2011.
- [15] T. J. Muldoon, M. C. Pierce, D. L. Nida, M. D. Williams, A. Gillenwaater and R. Richards-Kortum, "Subcellular-resolution molecular imaging

- within living tissue by fiber microendoscopy," *Opt. Express*, 15(25), 16413-16423, 2007.
- [16] K. J. Rosbach, D. Shin, T. J. Muldoon, M. A. Quraishi, L. P. Middleton, K. K. Hunt, F. Meric-Bernstam, T. Yue, R. R. Richards-Kortum and W. Yang, "High-resolution fiber optic microscopy with fluorescent contrast enhancement for the identification of axillary lymph node metastases in breast cancer: a pilot study," *Biomed. Opt. Express*, 1(3) 911-922, 2010.
- [17] T. J. Muldoon, D. Roblyer, M. D. Williams, V. M. T. Stepanek, R. Richards-Kortum and A. M. Gillenwater, "Noninvasive imaging of oral neoplasia with a high-resolution fiber-optic microscope," *Head & Neck*, 34(3), 305-312, 2012.
- [18] R. Manniesing and W. Niessen, "Multiscale vessel enhancing diffusion in CT angiography noise filtering," *Lect. Notes Comput. Sci.*, 3565, pp. 138-149, Springer, Berlin Heidelberg New York, 2005.
- [19] M. Miwa, "The principle of ICG fluorescence methods," *Open Surg. Oncol. J.*, 2, 26-28 2010.
- [20] M. Ogawa, N. Kosaka, P. L. Choyke and H. Kobayashi, "In vivo molecular imaging of cancer with a quenching near-infrared fluorescence probe using conjugates of monoclonal antibodies and Indocyanine Green," *Cancer Res.* 69(4), 1268-1272, 2009.

7. Mosaic Acquisition and Processing for Optical-Resolution Photoacoustic Microscopy (OR-PAM)¹

7.1 Introduction

Optical-resolution photoacoustic microscopy (OR-PAM) is a novel imaging modality for visualizing optically absorbing structures with high lateral resolution provided by fine optical focusing. Since proposed by Maslov et al. [1], it has been applied to both morphological and functional imaging in biological subjects. The technique was used to image microcirculation at the capillary level [2], brain microvascular morphology and oxygenation [3], amyloid plaques in Alzheimer's disease mouse models [4], ocular microvasculature [5], and healing processes of laser-induced lesions in small animal models [6]. Recently, Tsytarev et al. [7], used OR-PAM to monitor microvascular response to electrical stimulations of living mouse somatosensory cortex with exposed cranium.

Data acquisition time is limited by scanning speed, laser pulse repetition rate (PRR), and data transfer. Different raster scanning schemes were introduced, among which the most commonly used is to mechanically translate the bulky imaging head within the horizontal x-y plane [1]-[7] while firing laser pulses and receiving photoacoustic signals periodically. Considerable data acquisition time is unavoidable in this case. Hu et al. [8] reported that with their second generation

¹ A version of this chapter has been published. Reprint with permissions from: P. Shao, W. Shi, R. K. W. Chee and R. J. Zemp, *J. Biomed. Opt.*, 17(8), 080503, 2012. Copyright 2012 SPIE.

(G2) OR-PAM system developed recently, 70 minutes is needed to scan a mouse ear with an area of 7.8×10 mm. While stunning image quality was demonstrated, acceptance of the imaging modality in practical applications is hampered by the long data acquisition time.

Optical scanning was introduced by Xie et al. [9] to prevent mechanical scanning and to speed up the imaging process. While the laser beam raster scan was achieved by an x - y galvanometer scanner, an unfocused transducer was used to sense the generated photoacoustic signals. Utilizing a laser system with PRR of 1024 Hz, data acquisition time for a 256×256 -pixel image was reported as less than 2 min. Although a large circular field of view (FOV) of 6-mm diameter was demonstrated, a trade-off between signal to noise ratio (SNR) and FOV always exists. A hybrid-scanning OR-PAM (HSOR-PAM) scheme was used by Rao et al. [1]. With this setup, whereas fast scanning along one axis was achieved with a galvanometer mirror, mechanical scanning along the other axis was accomplished using a 1D mechanical translation stage. A cylindrically-focused transducer was used to receive ultrasonic signals. Using a laser system with a PRR of 5 kHz, the system required 256 s to obtain an $800 \times 1600 \times 200$ volumetric data set of live mouse ear vasculature. SNR of the imaging system was somewhat compromising middle ground between the optical scanning scheme of Xie [9] and mechanical scanning methods [1] [8]. Scanning range along the fast scan direction is limited. Furthermore, motion artifacts might be a potential problem when imaging a large area with this setup. Wang et al. [11] developed a voice-coil scanning system that is able to accomplish B-scan in a range of 1 mm at 40 Hz and 20 Hz at a range of 9 mm. Scanning in the other axis is achieved with a mechanical motor stage. Some of these system architectures could perform faster with a higher repetition rate laser. However, for the hybrid and optical scanning systems, the FOV will be limited in

at least one direction. Mechanical scanning will limit the image speed of G1 and G2 OR-PAM systems.

In this paper, we describe a fast OR-PAM system engineered for providing large FOV using mosaic acquisition and data processing. In this system, a 3-axis stepper-motor sub-system is used to mechanically move the target to be imaged from patch-to-patch in less than 0.5s. Patch images are aligned and stitched to generate a large scene composite. Our proposed system, which is a hybrid approach between laser-scanning and mechanical scanning, retains the SNR-advantages of focused-transducer OR-PAM systems we recently introduced [12].

7.2 Method

Configuration of our system is illustrated in Fig. 7.1. We use a diode-pumped pulsed Ytterbium-doped fiber laser system as the optical source (GLP-10, IPG Photonics Corporation), which generates 532-nm output pulses with durations of ~ 1 ns and the pulse energy can reach as high as $20 \mu\text{J}$. The PRR of the laser pulses is tunable within the range of 20 kHz to 600 kHz. A glass slide is used to reflect a small amount of light to a photodiode and used as a trigger for data acquisition. Optical scanning is achieved by a pair of galvanometer mirrors (6230H, Cambridge Technology Inc.) driven by two sinusoidal waves (x-y) from a function generator (Tektronix ATG 3022B). Scanning range (or FOV) of one individual image is determined by the amplitude of the sinusoidal signals. The scanned beam is focused by an objective lens (NA = 0.15, Thorlabs Inc.) with a focal length of 18 mm and then travels through our custom designed low-loss light-delivery probe [12] before reaching the imaging object. A 3.5 MHz ultrasound transducer (SLIG 3-02, CD International Technology, Inc.) with a 19-mm focal length and 6-mm active element is employed to sense photoacoustic signals.

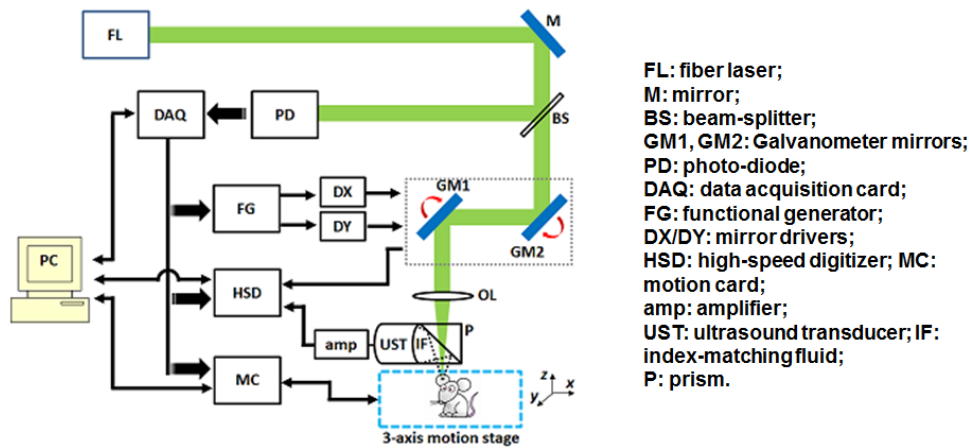


Figure 7.1 System configuration.

An 8-channel 12-bit PCI high speed digitizer (CS8289, Gage Applied Technologies Inc.) is used for data collection. Two channels of the HSD card are used to digitize and store photoacoustic signals and the scanning sinusoidal feedback signal with the higher frequency (x -axis). A pulser-receiver (5900 PR, Olympus NDT Inc.) is used for photoacoustic signal amplification and pre-filtering.

The object to be imaged is mounted on a motorized high precision 3-axis motion stage to realize mosaic movement. A PCI motion card (NI 7350) is utilized to communicate with the motion system that consists of three integrated high torque stepper motors (23Y002D-LW8, Anaheim Automation).

Mosaic acquisition is accomplished by acquiring small FOV fast-optical scans successively in a sequence of mosaic patches at mechanically-scanned 2D grid locations. The object is moved to each mosaic location until the entire region is covered. At each imaging spot, the location of the stage is sensed by encoders and recorded for patch alignment. Stage movement, data collection and optical scanning are coordinated with a square wave generated by a DAQ card (NI PCI 6221,

National Instruments) sharing the same frequency as the slow-axis (y -axis) scanning signal. Photoacoustic data acquisition is active only for the backward portion of the y -axis signal. During data acquisition, the low-phase of the coordinating square wave is used to inhibit the motors to avoid electronic noise from the motion sub-system. After each mosaic data acquisition is complete, and during stepper motor activation for subsequent patch positioning, data from the previous patch are transferred from the HSD-card on-board memory to a number of pre-allocated data buffers in the random-access memory (RAM) of the PC. The buffers are created when commencing the imaging task and utilized in a circular pattern to minimize system resource requirements. A separate thread manages saving data from PC RAM to the hard drive when buffers are not empty. Software for realizing data collection and motion control is written in C/C++. A flowchart of the control software is illustrated in Fig. 7.2. Multiple threading is used to coordinate tasks such as data acquisition, stage movement and data saving.

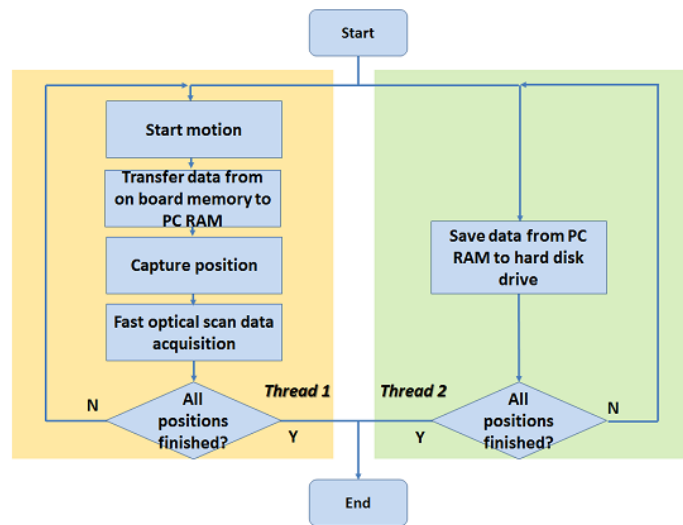


Figure 7.2 Flow chart of the control software. One thread is used to coordinate photoacoustic data acquisition, while the other thread is generated to save data into the PC hard-drive.

Scanning areas for each sub-image is intentionally kept larger than desired mosaic patch sizes. Image redundancy permits position shifts for image alignments to account for motion artifacts and also helps improve SNR in the marginal area of each small FOV scene. In data processing, mosaic patches are first positioned at corresponding locations on the 2D grid system then shifted according to the position feedback information obtained during the imaging process to compensate mechanical movement errors. Raster scanning directions are aligned to be parallel with the movement directions, therefore no complex image registration methods are required by this system. Image blending is essential for generating the large composite. We use the feathering [13] method to merge adjacent image mosaic patches. The pixel value at location (x, y) in the new image composite in the overlapping area is determined with the contribution of the two adjacent mosaic patches with the following method:

$$N(x, y) = \alpha I_A(x, y) + (1 - \alpha) I_B(x, y)$$

in which $N(x, y)$ is the pixel value in the new image composite at (x, y) , $I_A(x, y)$ and $I_B(x, y)$ are the pixel values of adjacent image A and B, respectively. α is the weighting function, which is simply calculated as the distance from image A. This helps eliminate the edge artifacts in the composite image.

7.3 Results

Figure 7.3 shows results of our phantom study. 36 images with a small FOV of $\sim 930 \mu\text{m} \times 930 \mu\text{m}$ were generated in total, as is shown in (a). The mosaic patches were then shifted according to the position feedback information and then stitched to generate the panoramic scene (b).

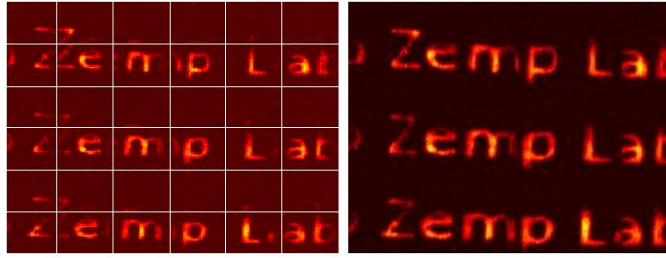


Figure 7.3 Phantom studies. (a) 36 Sub-images acquired at a 2D grid locations; (b) image composite generated with the mosaic images with image alignment and stitching.

We imaged the blood vessel structures of a 7-week old SCID Hairless Outbred (SHO™, Charles River, MA, USA) mouse ear for in vivo studies. All experimental procedures are in conformity with the laboratory animal protocol approved by the Animal Use and Care Committee of the University of Alberta. The mouse was under anesthesia during the imaging process.

The panoramic scene with an overall area of $6.45 \text{ mm} \times 5.8 \text{ mm}$ is shown in Fig. 7.4 (a). 90 (9×10) image mosaics were generated to composite the large FOV image. Distance between imaging spots is $645 \mu\text{m}$ and the original dimension of image mosaic is around $930 \mu\text{m} \times 930 \mu\text{m}$. (b) is an image composite with 4×4 image blocks, which is an image of the framed area A in image (a) but acquired separately after the animal was re-positioned. The vascular structures in (b) are consistent with those in the region A shown in image (a). To examine the image capability of our system, we take an individual image patch, which is shown in (c) from the large scene. With a fine resolution of around $6 \mu\text{m}$ of the system [12], detailed capillary structures can be resolved.

PRR of the laser system is 320 kHz for the imaging experiment. The measured pulse energy after the scanning mirror is $\sim 0.15 \mu\text{J}$. No damage was observed on the animal skin surface after imaging. Assuming that the laser focal spot is around $120 \mu\text{m}$ beneath the skin surface, the calculated laser fluence on the skin is 18

mJ/cm². This is less than the 20 mJ/cm² standard by American National Standards Institute (ANSI). We used 400 Hz (*x*-axis) and 1 Hz (*y*-axis) sinusoidal waves to drive the scanning mirrors, respectively. Therefore the B-scan frame rate across 930 μm is 400 Hz. Only 0.5 seconds is needed to collect data for one mosaic patch with 160,000 pixels (400 × 400). In total, only 1 second is required for one image mosaic including data acquisition, transfer and the stage movement.

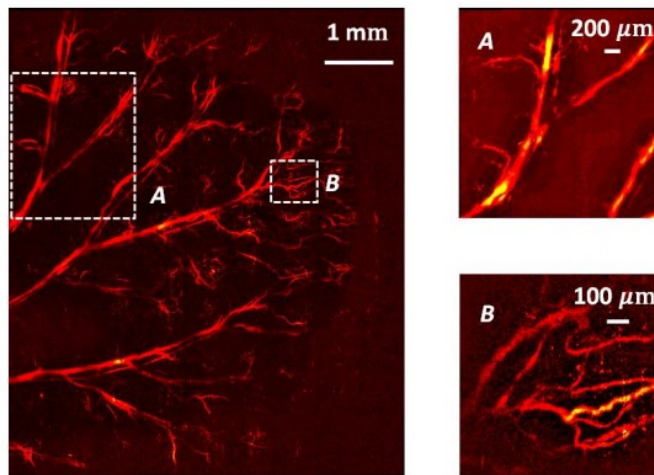


Figure 7.4 Micro-vasculature of a living mouse ear. Left: large image composite of the living mouse ear with FOV of 6.45×5.81 mm²; Upper right: a separate image of the same area framed with dashed box A in the image composite; Bottom right: a magnified individual patch taken from the image composite enclosed by the dash box B.

7.4 Conclusion and discussion

Several advantages of our mosaicing scheme should be noted. First, as a hybrid scanning approach between optical scanning and mechanical scanning, mosaicing significantly speeds up the data acquisition time of the imaging modality. With 320 kHz fiber laser, our system outperforms the G2 OR-PAM, which is introduced by Hu et al. [8] in terms of data acquisition speed. To scan a region of 7.8 mm × 10 mm, 70 min is required for G2 OR-PAM, whereas with the proposed system, only

90 s is needed for a region of $6.45 \text{ mm} \times 5.8 \text{ mm}$. Our system is at least 20 times faster than G2 in terms of data acquisition time per unit area. Since our system has similar pixel size with G2 OR-PAM, it still surpasses G2 OR-PAM by the same factor if compared with size of dataset per unit time range. Our system is also faster than existing systems with different scanning schemes in terms of dataset size as discussed above. This speed advantage will prove important for ease of use for end-users. Second, the mosaicing scheme significantly enlarged the FOV possible with optical-scanning OR-PAM, which is limited by the transducer focal waist. Third, since each mosaic patch is acquired in less than 0.5 seconds, motion artifacts per patch should be minimal, and motion artifacts between different mosaic patches can be compensated for by simple image processing. This scheme may be less prone to motion artifacts over large FOVs compared to other mechanical or hybrid-scanning methods [10]. Future work should validate robustness to motion in clinical scenarios. Finally, the mosaicing scheme enables multi-scale imaging with OR-PAM. As shown in Fig. 7.4 (a) and (b), one can conduct a rough scan in a larger area for preliminary study, and then direct the imaging system to a specific region of interest for further studies after re-adjusting the system in terms of focusing, etc. We believe the aforementioned merits will accelerate the acceptance of the imaging technique among biologists and clinicians.

Bibliography

- [1] K. Maslov, H. F. Zhang, S. Hu and L. V. Wang, "Optical-resolution photoacoustic microscopy for in vivo imaging of single capillaries," *Opt. Lett.* 33(9), 929-931, 2008.
- [2] S. Hu, K. Maslov and L. V. Wang, "Noninvasive label-free imaging of microhemodynamics by optical-resolution photoacoustic microscopy," *Opt. Express*, 17(9), 7688-7963, 2009.
- [3] S. Hu, K. Maslov, V. Tsytsarev and L. V. Wang, "Functional transcranial brain imaging by optical-resolution photoacoustic microscopy," *J. Biomed. Opt.* 14(4), 040503, 2009.
- [4] S. Hu, P. Yan, K. Maslov, J-M Lee and L. V. Wang, "Second-generation optical-resolution photoacoustic microscopy," *Opt. Lett.* 36(6), 1134-1136, 2011.
- [5] S. Hu, B. Rao, K. Maslov and L. V. Wang, "Label-free photoacoustic ophthalmic angiography," *Opt. Lett.* 35(1), 1-3, 2010.
- [6] S. Hu, K. Maslov and L. V. Wang, "In vivo functional chronic imaging of a small animal model using optical-resolution photoacoustic microscopy," *Med. Phys.* 36(6), 2320-2323, 2009.
- [7] V. Tsytsarev, S. Hu, J. Yan, K. Maslov, D. L. Barbour and L. V. Wang, "Photoacoustic microscopy of microvascular responses to cortical electrical stimulation," *J. Biomed. Opt.* 16(7), 076002, 2011.

- [8] S. Hu, P. Yan, K. Maslov, J-M. Lee and L. V. Wang, "Second-generation optical-resolution photoacoustic microscopy," *Opt. Lett.* 36(6), 1134-1136 2011.
- [9] Z. X. Xie, S. L. Jiao, H. F. Zhang and C. A. Puliafito, "Laser-scanning optical-resolution photoacoustic microscopy," *Opt. Lett.* 34(12), 1771-1773 2009.
- [10] B. Rao, L. Li, K. Maslov and L. V. Wang, "Hybrid-scanning optical-resolution photoacoustic microscopy system for in vivo vasculature imaging," *Opt. Lett.* 35(10) 1521, 2010.

8. Monitoring Photodynamic Therapy (PDT) with Photoacoustic Microscopy (PAM)¹

8.1 Introduction

Photodynamic therapy (PDT), or photochemotherapy, is a modality that takes advantage of toxicity of activated photosensitizer by light at selective wavelength to kill targeted diseased cells/ tissue [1]. PDT has been successfully applied to a wide range of medical conditions, for example, skin conditions and cancer treatment. During a PDT treatment, photosensitizer is activated from ground state to excited state by photons when exposed to treatment light source, then it releases energy to return to its ground state. In this process, energy is transferred from light to molecular oxygen, generating reactive oxygen species (ROS), for instance, singlet oxygen ($^1\text{O}_2$), which is highly toxic to cellular structures [2]. Therefore, the three interacting components: photosensitizer, light administration and oxygen play important roles in PDT. Evaluation of PDT treatment is of significant importance and urgently needed. However, it is recognized that to evaluate the efficacy of PDT with only the presence of these three components is not sufficient [3]. Despite the fact that dosimetry measurement is important, such as photosensitizer distribution, $^1\text{O}_2$ concentration and treatment light fluence (rate), biological responses monitoring is an effective means to evaluate the efficacy of PDT as it is a direct reflection of the treatment outcomes [4]. PDT-induced vasculature variation is the most important hallmark of these parameters.

¹ A version of this chapter is in preparation to be submitted to *J. Biomed. Opt.*

A number of techniques can be used to image vasculature. Magnetic resonance angiography (MRA) is a group techniques to image blood vessels based on MRI [5]. However, it requires imaging contrast agent, comparatively high cost and can provide only limited spatial and temporal resolution. Positron emission tomography (PET) also requires contrast agents to visualize vasculature [6]. Recently optical techniques, such as Laser Doppler imaging [7][8] and laser speckle imaging [9], have been proposed to study vasculature. However, these techniques suffers from either limited penetration depth due to highly scattered photons in soft tissue, limited resolution or difficulty to target specific region of interests in practices.

Photoacoustic (PA) imaging is a new imaging modality intensively studied recently because of its promise for combined high resolution and intrinsic optical contrast, which can reveal important physiological information without assistance of contrast agents [10]. As hemoglobin in blood is the dominant absorber in soft tissue to provide optical contrast, both computed photoacoustic tomography (PAT) and scanning photoacoustic tomographic techniques have been applied to a wide spectrum of topics for both morphological and functional studies [11]. Blood flow imaging based on the Photoacoustic Doppler Effect was accomplished [12]. In [13], Shi et al. realized real time monitoring of hemodynamics with an optical-scanning optical-resolution photoacoustic microscopy (OR-PAM) system.

Photoacoustic imaging techniques has also been proposed to evaluate efficacy of, or to monitor PDT by assessing vasculature changes. Xiang et al. [14] reported a PAT imaging system to monitor vascular damage in PDT on a check chorioallantoic membrane (CAM) tumor model. In their setup, a single pulsed laser with a wavelength of 532 nm served as the light source for both photoacoustic imaging and photodynamic therapy. The protoporphyrin IX (PpIX) was used as the photosensitizer. With this system, they visualized neovascularization in tumor

angiogenesis and then verified the capability of their system for imaging vascular structure damage by PDT. However, only target blood vessel size change was studied in their report. This study was also limited to topical application of photosensitizer on the CAM model.

In this study, we intend to monitor both morphological and functional information variations due to PDT with acoustic-resolution photoacoustic microscopy (AR-PAM, or PAM). With the wavelength tenability of our laser system, we are able to acquire not only vasculatures, but also oxygen saturation change of interested areas. In the present project, we are not restricted to topically application of photosensitizer to the CAM model, we also studied effects of PDT in a rat ear model with IV injection from a tail vein.

8.2 Method

The experiment setup is shown in Fig. 8.1. For the imaging task, we use a tunable nanosecond pulsed dye laser (ND6000, Continuum, Santa Clara, CA, U.S.) as the light source. The laser has a tunable wavelength range between 420nm – 900 nm with proper selected dyes. For the present study, we used Rhodamine 590 (Exciton, OH, U.S.). The laser pulse is coupled into a 600- μm multimode optical fiber. Laser pulse coming out of the fiber is first collimated. After being focused by a microscope objective lens, it is directed to the target by a custom-made imaging probe. An ultrasound transducer (V214-BB-RM, Olympus) with a 50-MHz center frequency was coupled with the probe acoustically. An acoustic lens was positioned under the probe to receive ultrasound energy. Signal detected by the transducer is digitized by a high-speed digitizer and then transferred to a PC for further processing. To realize raster scanning during the imaging task, the object is positioned on a 3-Axis motion stage, which is controlled by the PC through a motion control card [15]. An example of PAM images generated with this system

is shown in Fig. 8.2.

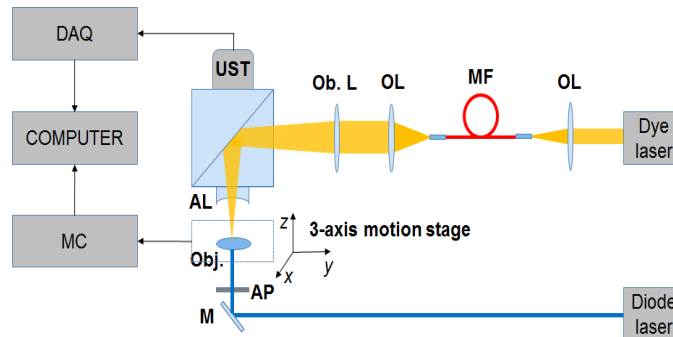


Figure 8.1 Experiment setup. OL: optical lens; MF: multi-mode fiber; Ob. L: objective lens; UST: ultrasonic transducer; AL: acoustic lens; AP: aperture; M: mirror; DAQ: data acquisition card; MC: motion controller.

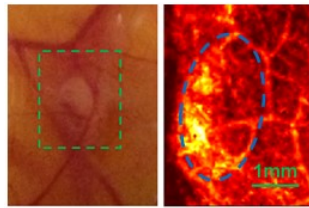


Figure 8.2 Setup PAM image of a HT1080 tumor-induced neo-vasculature on a CAM model. (a) is the white light picture of the HT1080 tumor in the CAM; (b) is the PAM image showing neovascularity around the tumor. Tumor region is labeled by a dashed circle.

A diode-laser with a 455 ± 5 -nm wavelength (Ultralasers, Newmarket, ON., CAN) was utilized for PDT. The laser beam is directed to an aperture to adjust the beam size for treatment.

Verteporfin (129497-78-5, Sigma-Aldrich) was utilized as the photosensitizer. 3.6 mg Verteporfin was first dissolved in 500 μ L Dimethyl Sulfoxide (DMSO), and then diluted with Phosphate buffered saline (PBS) to various concentration for experiments. Storage and preparation of the solution is protected from light.

8.3 Results

To validate the capability of our system to image vasculature change due to PDT, a preliminary study was conducted with the CAM model. Verteporfin of $50 \mu\text{M}$ was topically applied to a region of treatment on the membrane 15 min before treatment. Then the embryo was positioned under the pulsed laser for a 20-min treatment. Power of the treatment beam was $20 \text{ mW}/\text{cm}^2$. As a comparison, we also illuminated another region on the same embryo without photosensitizer applied as a control. PAM images were taken before and after the treatment for both regions of interests. Results were shown in Fig. 8.3. Whereas vasculature remained the same in the image of the control area (upper row in Fig. 8.3), dramatic change was visualized in the treatment region (bottom row). Major blood vessel (with diameters $< 100 \mu\text{m}$) structures, for example, blood vessels marked as 1 and 2, in this area were destroyed. Capillary clouds were also partially damaged, leaving bleeding spots (bright spots).

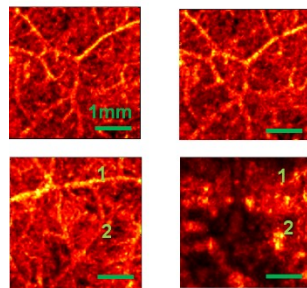


Fig. 8.3 PDT-induced vasculature change in a CAM model.

A longitudinal monitoring study was performed to examine vasculature variations due to the treatment. PAM images of the treatment area are shown in Fig. 8.3. One images was (#1) taken before the treatment, and then followed by images

taken after every 5-min treatment period. 50 μM Verteporfin was topically applied on the membrane surface 15 min before treatment. Optical fluence used for treatment was 10 mJ/cm^2 . 15 min was needed for taken each image with the size of 3.6 mm \times 3.6 mm. All parameters settings were kept the same for the imaging equipment during the experiment and the 7 images were displayed with the same colormap for comparison.

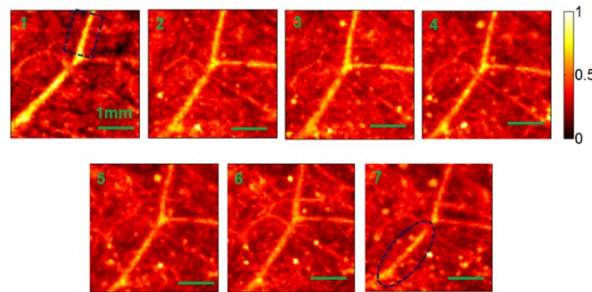


Figure 8.4 PDT-induced vasculature change in a CAM model. 50 μM Verteporfin was topically applied to the CAM surface 15 min before treatment with a fluence of 10 mJ/cm^2 . Images were taken sequentially during the treatment at every 5 minutes.

A steady decrease of pixel intensities corresponding to the major blood vessel structure is observed, which may imply the decrease of blood volume as the photoacoustic signal is proportional to the total concentration of hemoglobin. In Fig. 8.4, discontinuities appeared in the circled vessel, which may be thrombi after the treatment.

In some areas, capillary structures also experienced a decreased intensity values, leaving bright spots. We believe this is bleeding area due to damage of small blood vessels.

Decrease of blood vessel size is believed to be a result a PDT [4]. We compared the diameter change of a target vessel with a $242 \pm 20\text{-}\mu\text{m}$ width in image before

treatment (labeled by the dashed box in image #1). Measured size of the vessel experienced a steady decrease along with the treatment procedure (Fig. 8.5). Width of the vessel was defined by the region that has at least 50 % of the maximal pixel intensity of the vessel before treatment. An immediate size change occurred in the first a few minutes right after the treatment was started. A steady decrease continued till the end of measurements. An overall decrease of 70 % of the original size was observed by the end of the treatment.

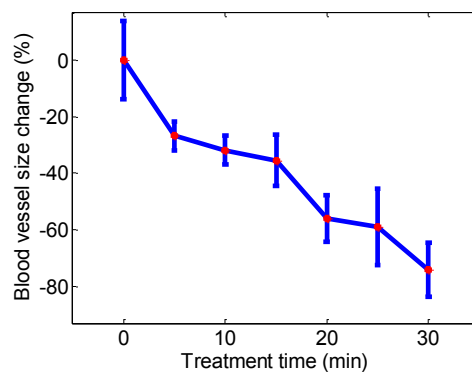


Figure 8.5 Change of a target blood vessel size in a CAM model due to PDT.

We also examined feasibility of our technique with a rat ear model. Before experiment, the whole rat ear was processed with hair removal cream for 10 min and then cleaned with warm water. Verteporfin was injected via a tail vein of a 60-g weight Sprague Dawley rat with a dose of 2 mg/kg (300 μ L) as suggested by literature. PDT was started 15 min after the injection. Laser pulse fluence was set to right blow 20 mJ/cm^2 , which is the upper value of the ANSI limit [10] for laser safety on skin surface for wavelength rage 400 nm – 700 nm to avoid laser-induced skin burn.

PAM images were acquired before the treatment, and at 30 min and 90 min after the treatment was started, respectively. Treatments was temporally stopped for

20 min when imaging the region of interest. Result images with the same colormap were shown in Fig. 8.6. Image (a) is the whole field of view before treatment with the region of treatment for quantitative study circled. (b) - (d) are zoomed-in versions of the treatment region. The size change of the target vessel (boxed in (b)-(d)) in the region of treatment is shown in Fig. 8.7. Size of the target blood vessel significantly shrank to ~55 % of its original after the treatment.

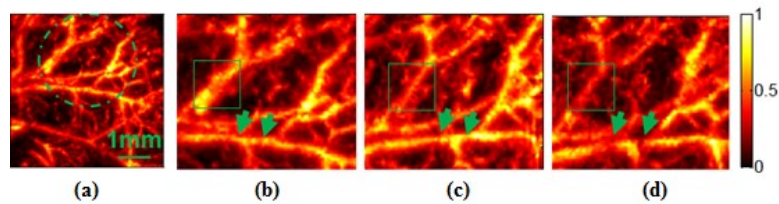


Figure 8.6 PDT-induced vasculature change in the treated area in a rat ear. (a) PAM image of the ear with treatment region circled. (b) – (d) vasculature change of the treatment area. A target blood vessel for quantitative analysis is labeled with a box.. Thrombi occurred at the locations labeled with arrows along with the treatment.

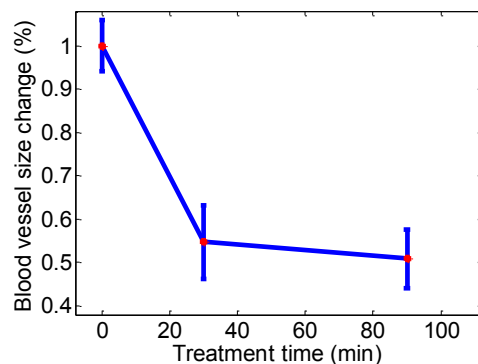


Figure 8.7 Change of a target blood vessel size in a rat ear model due to PDT.

Oxygen level is one of the most factors for PDT. With the tunable laser source, we longitudinally monitored the oxygen saturation level of a target vessel during the treatment. In Fig. 8.8 (a) is the region of treatment before and after the treatment.

SO₂ of labeled spots in the two images was measured multiple times with a 10-min interval during the experiment. An immediate drop of SO₂ was observed. During the treatment, the SO₂ level gradually recover to a slightly lower level compared with the original value.

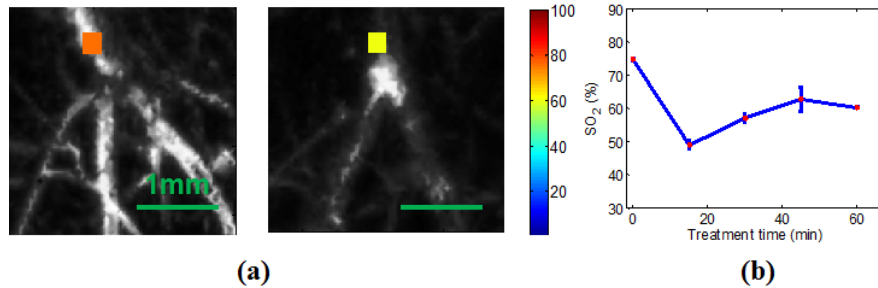


Figure 8.8 Oxygen saturation change during PDT. (a) Example of PAM image of the treated region, with measured SO₂ at the target vessel before and after treatment. (b) Variations of SO₂ at the target vessel along during the treatment.

8.4 Conclusion and discussion

We report our feasibility study of parametric imaging of vasculature response to PDT with photoacoustic microscopy. Functional information change induced by PDT is also measured with PA technique. To our knowledge, this is the first report of using scanning photoacoustic tomography to monitor PDT-induced biological response. As a label-free imaging modality combines high resolution and optical contrast, PA imaging is ideal for studying vasculature variations due to PDT. Our future work include to quantitatively image hemodynamics-related biological responses such as blood flow, blood volume change during PDT.

Bibliography

- [1] T. J. Dougherty, C. J. Gomer, B. W. Henderson, G. Jori, D. Kessel, M. Korbelik, J. Moan, and Q. Peng, “Photodynamic therapy,” *J. Natl. Cancer Inst.*, vol. 90, no. 12, pp. 889–905, Jun. 1998.
- [2] D. E. J. G. J. Dolmans, D. Fukumura, and R. K. Jain, “Photodynamic therapy for cancer,” *Nat. Rev. Cancer*, vol. 3, no. 5, pp. 375–80, May 2003.
- [3] B. Li, Z. Qiu, and Z. Huang, “Advanced optical techniques for monitoring dosimetric parameters in photodynamic therapy,” vol. 8553, p. 85530F, Dec. 2012.
- [4] J. P. Celli, B. Q. Spring, I. Rizvi, C. L. Evans, K. S. Samkoe, S. Verma, B. W. Pogue, and T. Hasan, “Imaging and photodynamic therapy: mechanisms, monitoring, and optimization,” *Chem. Rev.*, vol. 110, no. 5, pp. 2795–838, May 2010.
- [5] M. P. Hartung, T. M. Grist, and C. J. François, “Magnetic resonance angiography: current status and future directions,” *J. Cardiovasc. Magn. Reson.*, vol. 13, no. 19, pp. 1–11, 2011.
- [6] S. Valable, E. Petit, S. Roussel, L. Marteau, J. Toutain, D. Divoux, F. Sobrio, J. Delamare, L. Barré, and M. Bernaudin, “Complementary information from magnetic resonance imaging and (18)F-fluoromisonidazole positron emission tomography in the assessment of the response to an antiangiogenic treatment in a rat brain tumor model,” *Nucl. Med. Biol.*, vol. 38, no. 6, pp. 781–93, Aug. 2011.

- [7] A. Major, S. Kimel, S. Mee, T. E. Milner, D. J. Smithies, S. M. Srinivas, and J. S. Nelson, "Microvascular photodynamic effects determined in vivo using optical Doppler tomography," *IEEE J. Sel. Top. Quantum Electron.*, vol. 5, no. 4, pp. 1168–1175, 1999.
- [8] J. Tyrrell, C. Thorn, A. Shore, S. Campbell, and A. Curnow, "Oxygen saturation and perfusion changes during dermatological methylaminolaevulinate photodynamic therapy," *Br. J. Dermatol.*, vol. 165, no. 6, pp. 1323–1331, Dec. 2011.
- [9] H. Qiu, Y. Zhou, Y. Gu, Q. Ang, S. Zhao, Y. Wang, J. Zeng, and N. Huang, "Monitoring Microcirculation Changes in Port Wine Stains During Vascular Targeted Photodynamic Therapy by Laser Speckle Imaging," *Photochem. Photobiol.*, vol. 88, no. 4, pp. 978–984, Jul. 2012.
- [10] M. Xu and L. V. Wang, "Photoacoustic imaging in biomedicine," *Rev. Sci. Instrum.*, vol. 77, no. 4, p. 041101, 2006.
- [11] L. V Wang and S. Hu, "Photoacoustic tomography: in vivo imaging from organelles to organs," *Science*, vol. 335, no. 6075, pp. 1458–1462, Mar. 2012.
- [12] H. Fang, K. Maslov, and L. Wang, "Photoacoustic Doppler Effect from Flowing Small Light-Absorbing Particles," *Phys. Rev. Lett.*, vol. 99, no. 18, p. 184501, Oct. 2007.
- [13] W. Shi, P. Shao, P. Hajireza, A. Forbrich, and R. J. Zemp, "In vivo dynamic process imaging using real-time optical-resolution photoacoustic microscopy," *J. Biomed. Opt.*, vol. 18, no. 2, p. 26001, Feb. 2013.

- [14] L. Xiang, D. Xing, H. Gu, D. Yang, S. Yang, L. Zeng, and W. R. Chen, "Real-time optoacoustic monitoring of vascular damage during photodynamic therapy treatment of tumor," *J. Biomed. Opt.*, vol. 12, no. 1, p. 014001, 2007.
- [15] P. Shao, W. Shi, R. K. W. Chee, and R. J. Zemp, "Mosaic acquisition and processing for optical-resolution photoacoustic microscopy," *J. Biomed. Opt.*, vol. 17, no. 8, p. 080503, Aug. 2012.

9. Conclusions and Future Prospects

9.1 Summary of work done in this dissertation

The work presented in this dissertation can be divided into three parts. The first part focused on quantitative photoacoustic tomography (qPAT). The second part focused on developing new imaging platforms for quantitative photoacoustic microscopy (PAM) imaging. In the third part, experimental work was described for quantitatively imaging of vasculature variations due to photodynamic therapy with PAM.

qPAT: We pioneered the use of the multiple-illumination schemes in reconstruction of optical properties. Before our work, most work in qPAT focused mainly on reconstructing only the absorption coefficient distributions. With the involvement of multiple optical sources, the absorption-scattering non-uniqueness was broken, therefore both the optical absorption and scattering distributions are able to be faithfully estimated. We also for the first time de-coupled the Grüneisen parameter in PA imaging. This might lead to a potential for various clinical applications such as temperature monitoring in treatments. The work in this part was for deep tissue imaging in a macro-scale in PA imaging, and was demonstrated with numerical simulations. We were not yet able to experimentally present these concepts. Specifically, the work can be summarized as follows:

1. We developed a framework for quantitative estimation of optical properties with multiple-source PAT. The reconstruction method is able to recover optical absorption, scattering and Grüneisen parameter distributions in a known turbid media background with high accuracy;

2. We furthered our work in i) by introducing an iterative reconstruction method to recover optical absorption and scattering distributions with only ultrasound channel data rather than ideally reconstructed PAT images;
3. We proposed an iterative method which recovers absorption and scattering features consecutively. In each iteration, we first estimate the absorption map with a least-squares fixed-point iterative method introduced by our group and then use this as a guide to update the background optical fluence, whereupon scattering distribution is estimated based on optical fluence.

Quantitative PAM imaging platforms: In this part, we developed new imaging platforms for superficial structure imaging on a micro-scale. We tried to further previous imaging techniques and proved new concepts with experimental demonstration:

1. We demonstrated a multi-modality imaging system that can simultaneously accomplish optical-resolution PAM vasculature imaging and fluorescently labeled cellular structure imaging;
2. ii) We presented a fast, wide-field-of-view (FOV) optical-resolution PAM system which significantly reduced data acquisition time to a clinically realistic scale with arbitrary FOV size.

Quantitative PAM imaging of vasculature variations: We presented a preliminary study which use acoustic-resolution PAM (AR-PAM) to monitor vasculature variations during photodynamic therapy (PDT). *In vivo* experiments were conducted with both chick chorioallantoic membrane vasculature model and a rat ear model to monitor blood vessel diameter change and oxygen saturation variations induced by the treatment was quantitatively monitored. This work

demonstrated the promise of PAM for imaging blood vessel ablation and oxygen depletion during PDT.

9.2 Directions of future work

Quantitatively imaging tumor-induced vasculature is highly desired in both biomedical fundamental and clinical studies. Both the theoretical and imaging platforms can be applied to a spectrum of applications in this field.

The series qPAT algorithms can be applied to quantitative imaging of cancer angiogenesis. The abilities of these algorithms to recover both optical absorption and scattering enables PAT to provide scientists and clinicians with multiple parameters that might be important for diagnosis. For example, cancerous tissue usually present enlarged cell nuclei. Our algorithms have the potential to identify scattering anomalies induced by the diseased cells. Another example is that the spatially varying Grüneisen parameter distribution is highly temperature-dependent. Grüneisen maps recovered by our algorithms can be used to monitor temperature change in applications such as thermal therapy of cancer.

The multi-modality system has the potential for studying tumor angiogenesis-related topics as it can simultaneously image fluorescently labelled cellular structure. For example, in diagnosis of cancer, the morphological change in vasculature due to angiogenesis and tissue anomalies can confirm each other. The fast, wide-FOV OR-PAM can be a powerful tool for imaging vasculature due to its quick imaging speed in contrast to conventional systems that requires tens of minutes data acquisition time.